Integrated CFD-Based Optimization of Rocket Nose cone and Nozzle Configurations for Enhanced Aerodynamic and Propulsive Efficiency

a project presented to

The Faculty of the Department of Aerospace Engineering

San José State University

in partial fulfillment of the requirements for the degree

Master of Science in Aerospace Engineering

by

Luis D Jurado Soto

May 2025

approved by

Dr. Yawo Ezunkpe

Faculty Advisor

Abstract

Integrated CFD-Based Optimization of Rocket Nose cone and Nozzle Configurations for Enhanced Aerodynamic and Propulsive Efficiency

Luis D Jurado Soto

This project presents a comprehensive aerodynamic and propulsion optimization study aimed at improving the overall efficiency of a rocket launch vehicle. The first phase of the study focused on evaluating and comparing various nose cone configurations to minimize aerodynamic drag during ascent. Using computational fluid dynamics (CFD) simulations, the aerodisk configuration was identified as the most effective design, demonstrating a significant reduction in bow shock intensity and stagnation pressure relative to traditional blunt geometries. The second phase of the project explored nozzle optimization through theoretical analysis and 3D CFD simulations. A baseline aerospike nozzle was analyzed by a parametric study that varied throat area, chamber geometry, ramp curvature, and ambient pressure. Among four configurations evaluated, the combined-optimization aerospike nozzle yielded the highest thrust output and most efficient expansion characteristics. Theoretical predictions were validated against CFD results to confirm performance accuracy. The project concludes by identifying the optimal nose cone and nozzle designs, and proposes future work involving full-scale modeling, thermal protection analysis, experimental validation, and advanced turbulence modeling. The findings provide a strong foundation for further development of high-performance space launch systems.

Acknowledgements

I would like to express my deepest gratitude to Dr. Yawo Ezunkpe for serving as my advisor throughout this project. His guidance, feedback, and encouragement were invaluable in helping me navigate the technical and academic challenges of this project. I am also immensely thankful to my beloved family and friends for their unwavering support, patience and motivation which carried me through the demanding phases of this journey. Their belief in me made this accomplishment possible.

Table of Contents

LIST OF FIGURES

LIST OF TABLES

Nomenclature

Symbol	Description	Units
ρ	Fluid density	kg/m^3
u	Velocity vector	m/s
p	Pressure	Pa
τ	Viscous stress tensor	Pa
g	Gravitational acceleration vector	m/s^2
E	Total specific energy	J/kg
e	Internal energy	J/kg
k	Thermal conductivity	W/(m·K)
T	Temperature	K
Φ	Viscous dissipation term	W/m^3
ω	Specific dissipation rate	1/s
k	Turbulent kinetic energy	m^2/s^2
G_k	Generation of turbulent kinetic energy	$kg/(m \cdot s^3)$

G_ω	Generation of specific dissipation rate	kg/(m·s³)
Y_k	Dissipation of turbulent kinetic energy	kg/(m·s³)
Y_ω	Dissipation of specific dissipation rate	kg/(m·s³)
Γ_k	Effective diffusivity of k	m²/s
Γ_ω	Effective diffusivity of ω	m²/s
D	Drag force	N
C_d	Drag coefficient	—
u	Freestream velocity	m/s
A	Reference area	m²
M	Mach number	—
M_e	Exit Mach number	—
v_e	Exit velocity	m/s
A_t	Throat area	m²
A_e	Nozzle exit area	m²

ω(M)	Prandtl-Meyer expansion angle	degrees
F	Thrust	N
ṁ	Mass flow rate	kg/s
P_o	Total pressure at inlet	Pa
P_a	Ambient pressure	Pa
P_e	Exit static pressure	Pa
T_0	Total temperature at inlet	K
R	Specific gas constant	J/(kg·K)
γ	Ratio of specific heats	—

Chapter 1. Introduction

1.1 Introduction

Space exploration and commercial space travel have experienced significant growth in recent decades, leading to increased demand for efficient rocket designs. U.S. commercial space operations have seen an exponential increase in just the past decade. Since 2017, there has been a 70% increase in U.S. commercial space operations, with 124 total operations conducted last year in 2023 (U.S. Government Accountability Office, 2023). NASA, SpaceX, Blue Origin, and Lockheed Martin are among the leading entities that build and design the launch vehicles to operate these commercial space missions. Despite being multi-billion dollar companies, they all end up facing the same challenge, global warming. There is an estimated 1,000 tons of black carbon emitted annually by space-related launch vehicles(rockets) and researchers predict that this trend would see an annual increase in temperatures in the stratosphere between 0.5 – 2° Celsius (National Oceanic and Atmospheric Administration, 2022). Researchers predict this change will affect global circulation patterns by slowing the subtropical jet streams by as much as 3.5% and thus weakening the stratosphere's overturning circulation (National Oceanic and Atmospheric Administration, 2022). A layer of ozone resides within the stratosphere, which is essential in protecting humans and our ecosystems from harmful radiation.

Heavy ongoing research and collaboration is being done to help combat this challenge, namely NASA by attempting to produce different fuel alternatives. Out of the currently available rocket fuels approved by the Federal Aviation Administration (FAA), solid chemical rocket fuel is relatively more cost-efficient and safer than the other alternatives, despite its environmental impact. Customers funding commercial space programs value cost at a high standard, therefore they will always choose the propellant that is the most cost-efficient. In 2023, the U.S. launched 96 Falcon-9s out to space, that statistic makes up about 44% of the total launch vehicles launched that same year by the whole world [1]. Falcon-9 rockets use solid rocket fuel and it is estimated that they emit between 200-300 tons of black carbon per the NOAA (National Oceanic and Atmospheric Administration, 2022).

To combat this carbon emission issue, I would like to optimize the fuel performance of these launch vehicles. One of the critical factors influencing rocket performance is the design of the nose cone and nozzle. The nose cone is responsible for minimizing aerodynamic drag, while the nozzle plays a crucial role in converting the energy from combustion into thrust. Optimizing these components can lead to improved mission success, increased weight capacity, and most of all fuel efficiency. Previous research has explored various nose cone geometries, such as conical, ogive, and parabolic shapes, as well as different nozzle designs, including convergent-divergent and aerospike nozzles. However, there is still room for improvement in terms of achieving a balance between aerodynamic efficiency, structural integrity, and manufacturability.

1.2 Literature Review

1.2.1 Background

The history of rockets has evolved drastically ever since their origin in China during the 13th century as explosive arrows to the advanced space launch vehicles we see today. Early rocket technology, like multi-stage rockets developed by Johann Schmidlap, laid the foundation for modern advancements in propulsion systems. Significant contributions to rocketry were made by pioneers such as Konstantin Tsiolkovsky and Robert Goddard, with Goddard achieving the first successful flight of a liquid-fueled rocket in 1926, marking a milestone in space travel [2]. In addition, research on rocket nozzles has seen growth over the past 75 years. The development of nozzles, from the simple convergent-divergent design introduced by Carl de Laval to modern bell and aerospike nozzles, has continuously focused on improving thrust efficiency and addressing aerodynamic losses. Rocket nozzle research has aimed to optimize parameters like expansion ratios and nozzle contours, leading to innovations such as the dual bell and multi-nozzle grid designs, which offer improvements in altitude compensation and overall performance [3].

1.2.2 Overview

A major factor that affects the rocket fuel performance comes from the rocket design, primarily the nose cone and nozzle. The nose cone is the first thing that comes into contact with the air, it is responsible for minimizing aerodynamic drag and tolerating high temperatures due to air friction. The geometry and material selection will determine the drag that will be experienced and the overall efficiency of the rocket. A scholarly journal posted on Science Direct talks about a two-stage rocket launched in New Zealand, and it goes into detail of the design process for the rocket. The material used for their nose cone was 3D-printed titanium to withstand high temperatures, however, one of the risks with this material selection is the weight that it is imposed on the rocket. Typically, for two-stage rockets you want the center of gravity and center of mass to ideally be near the rear of the rocket to avoid weather rocking during flight [4]. The nozzle is responsible for maximizing thrust efficiency by optimizing the expansion of exhaust gasses. Similar to the nose cone, the nozzle's geometry, structural integrity, and material selection are critical factors that affect the efficiency of the rocket. Xiang-Yang Liu and his colleagues have attempted to improve the overall efficiency by optimizing the design of the aerospike nozzle with a rotating detonation engine [5]. However, this attempt was faced with some challenges such as dealing with large pressure fluctuations.

1.2.3 Nose Cone Design and Material Considerations

The nose cone of a rocket is the first component to encounter atmospheric drag. Its geometry is critical in determining the aerodynamic forces experienced by the rocket, particularly at high speeds. There are several nose cone geometries that have been explored, including conical, ogive, and parabolic shapes as mentioned before. Each design offers distinct advantages depending on the flight conditions, and rocket dimensions along with its weight. Conical nose cones are easy to manufacture and perform well at subsonic speeds, but they generate more drag at higher speeds. [6]. In contrast, ogive shapes are more aerodynamically efficient at supersonic and hypersonic speeds, making them ideal for space travel [7]. Figure 1.2 displays the different nose cone shapes,

starting from the left and moving to the right we have; (a) Conical, (b) Ogive, (c) Ellipsoid, (d) Power series, (e) Parabolic series, and (f) Haack series. [6].

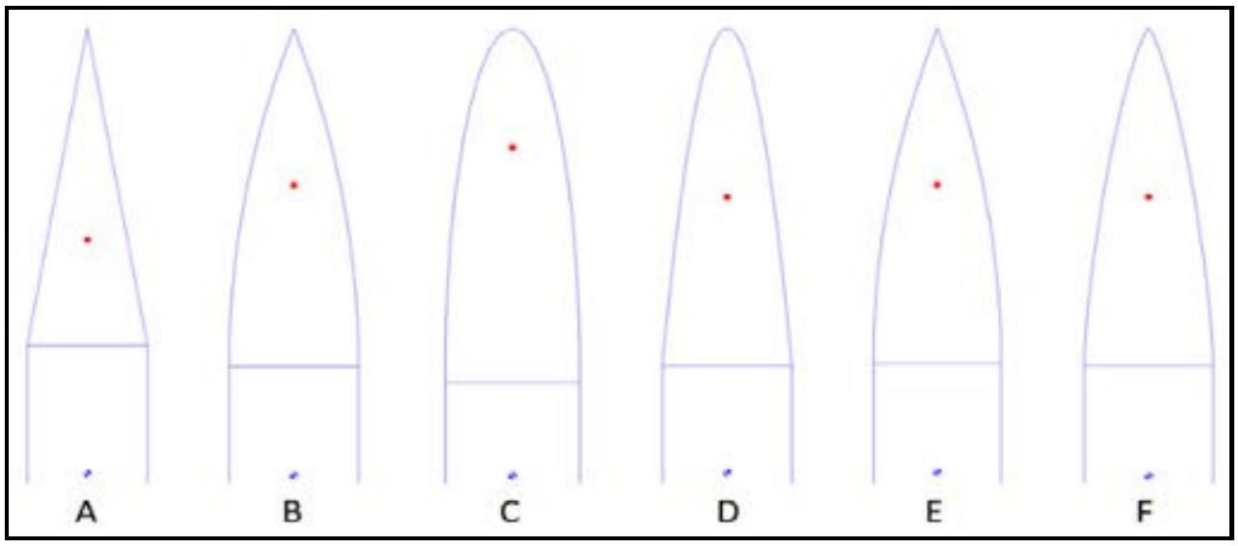

Figure 1.1 Nose cone shapes via OpenRocket simulator [6]

A study in 2021 explored the optimal nose cone geometrical shape for supersonic rockets, comparing conical and ogival nose shapes using CFD simulations. Figure 1.2 illustrates the comparison between the wedge and ogive nose gone geometries for drag and lift coefficients at Mach 2. The study found that the ogival shape produced significantly less aerodynamic drag than the conical design at Mach 2, making it more suitable for supersonic flight. These findings reinforce the importance of selecting the appropriate geometry for the specific flight conditions of the rocket [7].

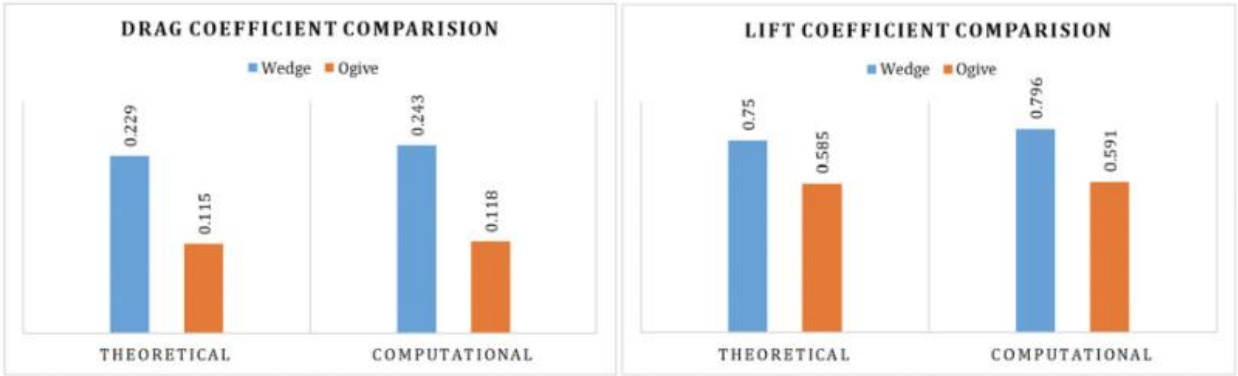

Figure 1.2 Bar graph comparison between wedge and ogive shaped nose cones [7]

In addition to geometry, material selection plays just as an important factor in the performance of nose cones. Nose cones must withstand extreme temperatures during flight due to atmospheric friction, especially during ascent and re-entry. One of the most innovative materials used in modern rocket design is 3D-printed titanium, which has been employed in two-stage rockets to handle high thermal loads. However, despite its strength and heat resistance, titanium poses a weight penalty that can shift the rocket's center of gravity forward, negatively impacting

flight stability [8]. Other materials such as fiberglass and carbon fiber offer lighter alternatives, though they may not perform as well under intense thermal conditions.

Innovative approaches to nose cone design have also been explored. For instance, researchers studied the application of fillets to reduce stress concentrations in rocket nose cones [9]. By using fillets in the design, the study demonstrated that both thermal and mechanical stresses were reduced, which significantly improved the overall structural integrity of the nose cone [9].

1.2.4 Aerodynamic Additions: Aerospikes and Aerodisks

In high-speed flight, reducing drag is critical for improving the rocket's performance and one method in particular that has been extensively researched is the use of aerospikes and aerodisks. Figure 1.3 depicts what these aerodynamic devices look like, (a) the aerospike and (b) the aerodisk. These aerodynamic devices, when added to a blunt body, alter the flow structure around the vehicle, reducing pressure drag and improving in turn fuel efficiency. A comprehensive study on the effects of aerospikes and aerodisks in supersonic flows was conducted in 2024 and the study used CFD simulations to evaluate the performance of various spike lengths and disk diameters in reducing drag on blunt bodies at Mach 2. The optimal configuration resulted in a substantial drag reduction of up to 40%, demonstrating the potential of these devices in rocket and missile applications [10].

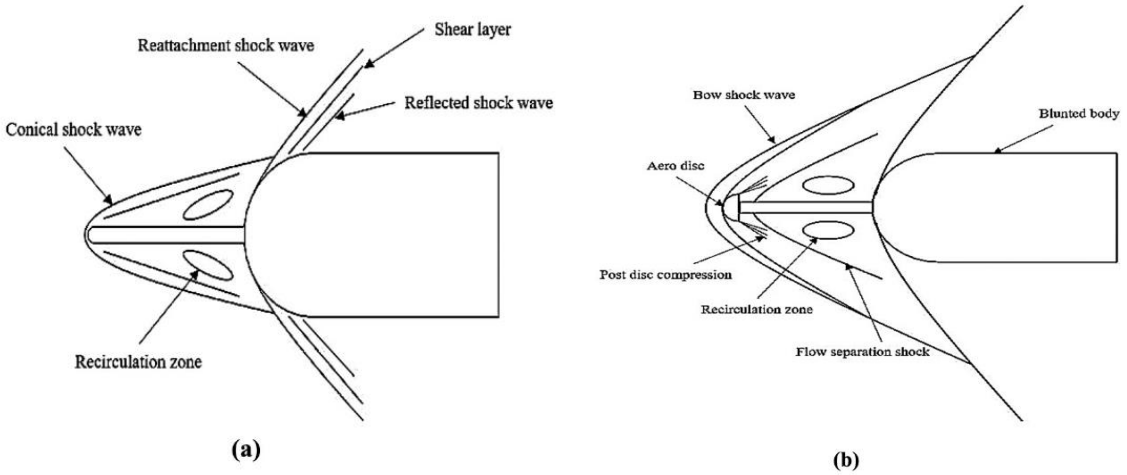

Figure 1.3 Flow field characteristics of (a) Aerospike cone (b) Aerodisk cone [10]

The combination of aerospikes and aerodisks creates a recirculation zone in front of the blunt body, reducing the strength of the detached shockwave and significantly lowering drag. This principle has been applied to rockets, re-entry vehicles, and space capsules, which benefit from the enhanced aerodynamic performance. Additional studies have shown that adjusting the aerospike length and disk diameter further optimizes drag reduction, though beyond a certain point, increasing the spike length offers diminishing returns [5].

1.2.5 Nozzle Design and Performance Optimization

Rocket nozzles play a crucial role in determining the efficiency of a propulsion system by converting the chemical energy from the combustion of propellants into kinetic energy, producing

thrust. The most commonly used nozzle is the convergent-divergent (De Laval) nozzle, which accelerates exhaust gases to supersonic speeds through a carefully shaped throat and expansion section [11]. However, recent research has explored advanced nozzle designs, such as aerospike nozzles, to maintain efficiency across a wide range of altitudes.

Researchers have conducted a study on the design and optimization of an aerospike nozzle for use with a rotating detonation engine (RDE). The aerospike nozzle showed promising results in improving thrust by maintaining optimal gas expansion across varying altitudes. However, the RDE introduced challenges related to pressure fluctuations, which required further optimization to fully harness the potential of the aerospike design [5].

A separate study presented a new shape design optimization methodology for rocket nozzles based on the method of characteristics (MoC). This method allows for the optimization of the nozzle shape while balancing the trade-offs between thrust efficiency and nozzle length. The study demonstrated that the optimized nozzle design achieved a higher coefficient of thrust compared to traditional methods, showing the effectiveness of the MoC in improving nozzle performance [12]

In addition to geometry, the materials used for nozzle construction are essential for ensuring performance and durability, especially when dealing with high-temperature combustion environments. Research conducted by NASA's Lewis Research Center evaluated several materials, including refractory metals, graphites, and ceramics, for use in solid-propellant rocket nozzles. Tungsten and molybdenum exhibited excellent resistance to erosion and thermal-stress cracking, making them ideal candidates for high-performance nozzles. However, even these materials were susceptible to oxidation, particularly in environments with high aluminum content in the propellant [13].

Moreover, the development of contour optimization methods has further improved nozzle performance. A study published in the *International Journal of Aerospace Engineering* introduced a new contour design for rocket nozzles with large exit area ratios, which led to significant gains in vacuum-specific impulse. By utilizing thermally perfect gas assumptions, the modified Rao method enabled a thinner expansion section and improved thrust performance for the tested rocket nozzle [14].

1.2.6 Innovation and Emerging Trends

Emerging trends in rocket design are not limited to traditional approaches. Advanced techniques such as additive manufacturing have been increasingly applied to the production of both nose cones and nozzles, allowing for more complex geometries and lighter components. The use of carbon-fiber composites and 3D-printed titanium in high-altitude rockets provided a well-balanced solution for the structural and thermal demands of space travel due to the lightweight properties of carbon fiber, combined with the thermal resistance of titanium [5].

Additionally, new computational techniques have made it possible to conduct more sophisticated simulations of flow characteristics around nose cones and nozzles. CFD and FEA (Finite Element Analysis) tools have become essential in the design process, allowing engineers to test multiple configurations and optimize for performance before physical prototyping. For

instance, ANSYS is being used to simulate the mechanical and thermal properties of different nozzle designs, demonstrating how advanced software tools can drive innovation in rocket propulsion systems [9].

1.2.7 Thermal Stress and Heat Flux in Rocket Nozzles

The thermal loads experienced by rocket nozzles during operation are crucial in determining the structural integrity and longevity of the nozzle. A study conducted in 2023 analyzed the thermal stress on solid rocket nozzles using fluid-structure interaction simulations. The research highlights the importance of accounting for thermal stress in the design of nozzles, particularly for rockets that utilize solid propellants. Two different MX-450 rocket nozzles were tested, one being the nozzle used in a 2021 static-firing test and the other being a newly modified nozzle design with an increased graphite thickness. The results demonstrated that increasing the graphite thickness in the nozzle led to a reduction in the minimum principal stress by 8.7 MPa, which was key to improving its thermal performance [15]. The use of materials like graphite in nozzles is essential for handling the extreme thermal conditions generated during rocket combustion. However, the design of these materials and the thickness of components such as graphite inserts must be carefully considered to prevent structural failure due to thermal stress. The fluid-structure interaction method used in the study allowed for more accurate predictions of how thermal loads interact with structural components, providing key insights into how future nozzle designs can be improved.

1.2.8 Aerodynamic Drag Reduction and Heat Flux in Nose Cones

In addition to thermal stress management, reducing aerodynamic drag and heat flux is a critical consideration in the design of hypersonic rockets. Research has investigated several spike geometries, including bi-conic, parabolic, ogive, elliptical, spherical, and flat-tapered spikes attached to parabolic nose cones, under hypersonic flow conditions. Flat-tapered spikes exhibit the most significant reduction in both aerodynamic drag and heat flux, making them an optimal choice for high-speed applications [16].

1.3 Motivation

Despite engineers trying their best to improve their designs, they end up facing a hurdle that winds up becoming much more challenging than the initial problem at hand. The increasing demand for cost-effective and environmentally sustainable rocket technologies drives the need for improved nose cone and nozzle designs. Enhancing the aerodynamic and propulsion efficiency of rockets can lead to reduced launch costs, increased weight capacity, and lower environmental impact. By focusing on optimizing these components, this project aims to build upon existing research by conducting a comprehensive study and developing optimized designs for rocket nose cones and nozzles.

1.4 Methodology

This project was conducted in multiple phases, beginning with an extensive literature review to establish a solid foundation in nose cone and nozzle aerodynamics. Research sources included peer-reviewed databases such as ScienceDirect and Google Scholar, as well as technical

publications relevant to launch vehicle design. This review guided the development of theoretical frameworks and informed early assumptions for geometry and flow behavior.

Following the research phase, preliminary comparisons were made between existing rocket designs, including Atlas V, Delta IV, and Falcon 9, to extract dimensional and performance benchmarks. CAD models of nose cone and nozzle geometries were created using Autodesk Inventor, and ANSYS Fluent was used to perform 3D CFD simulations across a range of configurations. These simulations evaluated Mach number, velocity, pressure, temperature, density, and enthalpy distributions. Where applicable, geometric parameters were modified to improve mesh quality and flow resolution.

For propulsion-related analysis, MATLAB was used to develop scripts that computed exit velocity, thrust, area ratios, and compared theoretical values to CFD results. Multiple nozzle designs—including conic, bell, double-bell, and aerospike—were studied in detail, and a parametric optimization of the aerospike nozzle was conducted by varying throat area, ramp curvature, chamber extension, and ambient pressure. Each configuration was evaluated against performance metrics to determine its relative efficiency.

Results from both nose cone and nozzle phases were compiled, compared, and validated using theoretical models. The final outcome was a complete assessment of aerodynamic drag reduction and thrust optimization, culminating in a recommendation for the most efficient design. This methodology not only supported the objectives of the current study, but also lays the groundwork for future development and research in launch vehicle optimization.

Chapter 2. Case Study - Launch Vehicle Design Comparisons

2.1 A Case Study Analysis of Atlas V, Delta IV, and Falcon 9

This chapter dives into the design choices made in three rockets—Atlas V, Delta IV, and Falcon—focusing on their nose cone geometries, nozzle configurations, and material selections. Through examining these components, this chapter aims to derive insights into how design decisions correlate with mission requirements and vehicle performance.

2.2 Atlas V

2.2.1 Atlas V Overview

The Atlas V, developed by United Launch Alliance (ULA), is a versatile launch vehicle used for both commercial and government missions, including interplanetary launches. It features a modular design with various configurations, such as the addition of solid rocket boosters (SRBs) for enhanced lift capacity. The vehicle is particularly known for its reliability in high-stakes launches [17].

2.2.2 Atlas V Nose Cone Design

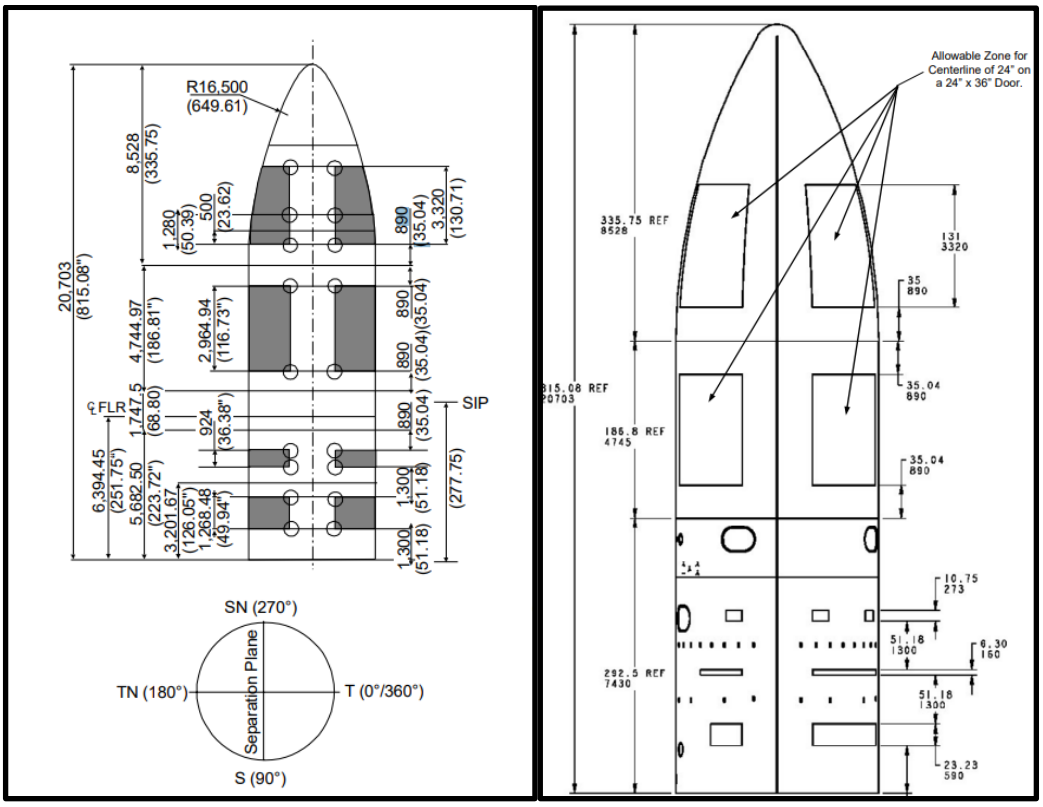

Figure 2.1 Atlas V 20.7m payload fairing dimensions [20,23]

The payload fairing of the Atlas V is available in two sizes for different mission needs: the 5-meter diameter fairing with short and medium configurations (20.7 and 23.4 meters in height, respectively). This design provides substantial payload protection during ascent and

accommodates various payload shapes and sizes [17]. The fairing is constructed using a composite shell design, combining graphite epoxy face sheets with an aluminum honeycomb core. The lightweight and sturdy structure helps withstand aerodynamic loads, minimizing weight while providing robust protection against atmospheric drag and heating [17].

Based on the drawings in Figure 2.1., this specific fairing of 20.7m x 5m seems to have an ellipsoid-shaped nose cone. In Chapter 1, figure 1.1 displays the general shapes of nose cones, and the ellipsoid-shaped nose cone closely matches the nose cone shape for the Atlas V. However, it is a combination of an ogive nose cone leading to a spherical cap [20]. This configuration is effective at minimizing drag while also maintaining thermal shielding for the fairing.

2.2.3 Atlas V Nozzle Design

The Atlas V booster stage utilizes the RD-180 engine, a dual-chamber liquid rocket engine, that provides primary thrust for the Atlas V booster. It operates using a combination of RP-1 (a refined form of kerosene) and liquid oxygen (LOX). This engine is designed with an optimized bell nozzle for high thrust at sea level and is capable of providing both gimbal control and stability during ascent [20].

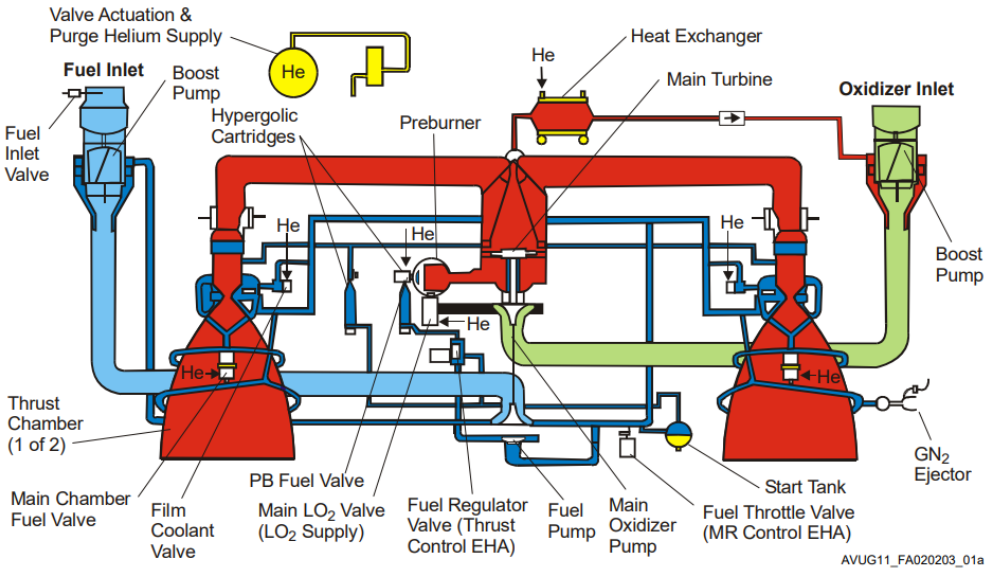

Figure 2.2 RD-180 engine schematic [20]

2.2.4 Atlas V Material Choices

Atlas V employs composite materials in its fairing, specifically graphite epoxy combined with an aluminum honeycomb core. This choice reduces the weight and improves the structural durability of the fairing while also providing thermal protection during ascent. The RD-180 engine nozzle in the first stage includes carbon phenolic materials, which are known for their high thermal resistance and durability in withstanding the intense heat and pressure during launch [20].

2.3 Delta IV

2.3.1 Delta IV Overview

Delta IV, also developed by ULA, is known for its heavy-lift capabilities, primarily supporting government and military missions that require high-energy orbits. This vehicle's design emphasizes payload capacity and reliability for high-stakes missions [18].

2.3.2 Delta IV Nose Cone Design

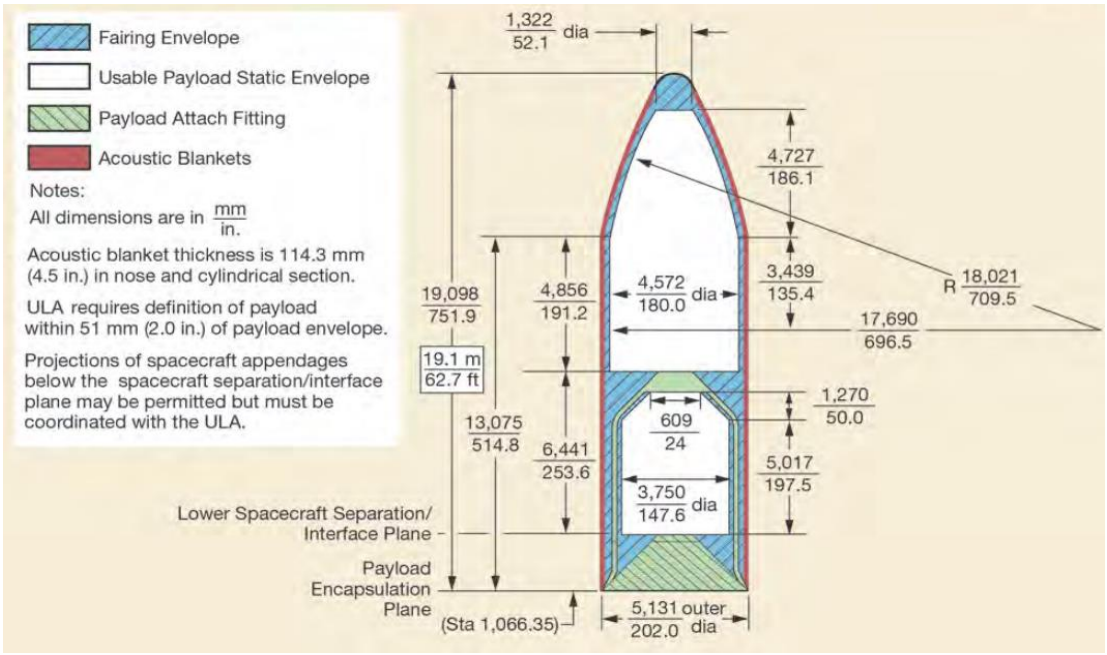

Figure 2.3 Five meter fairing dimensions for Delta IV

The Delta IV utilizes a 5-meter diameter payload fairing, similar to the Atlas V, made from a composite structure with graphite epoxy face sheets and an aluminum honeycomb core. This design provides aerodynamic stability and payload protection while minimizing additional weight [18]. Similar to the Atlas V, the nose cone shape starts ogive and then is capped with a spherical top. The design choice is practically the same, minimizing drag while also ensuring minimal thermal resistance.

2.3.3 Delta IV Nozzle Design

Delta IV's bell nozzle design is optimized for high thrust, accommodating the demands of heavy-lift missions. The RS-68A engine operates on liquid oxygen (LO2) and liquid hydrogen (LH2) cryogens, producing 3137 kN of thrust at sea level with a vacuum-specific impulse of 411.9 seconds. The nozzle design has an expansion ratio of 21.5 to 1 and uses a gas generator cycle, with regenerative cooling in the thrust chamber. This configuration is designed for high-thrust requirements in atmospheric and vacuum conditions. [18].

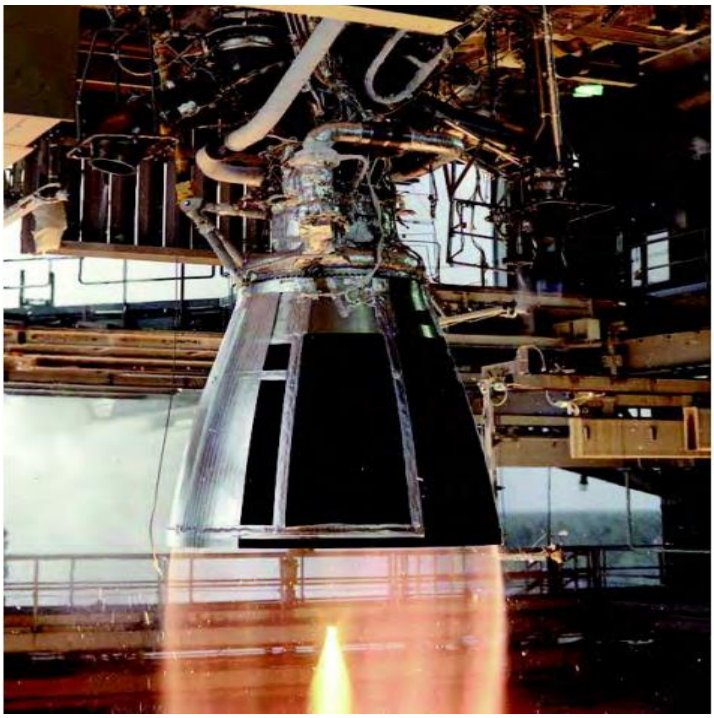

Figure 2.4 Delta IV's RS-68A engine [18]

2.3.4 Delta IV Material Choices

Delta IV employs the same graphite epoxy and aluminum honeycomb structure in its fairing as the Atlas V, prioritizing lightweight strength. For the nozzle, high-temperature-resistant materials, such as carbon-carbon composites, are used to manage the extreme conditions associated with heavy-lift missions, as outlined in the user guide [18].

2.4 Falcon 9

2.4.1 Falcon 9 Overview

The Falcon 9 rocket, developed by SpaceX, is a reusable launch vehicle designed for various missions, including satellite launches and cargo resupply missions to the International Space Station. Falcon 9's design emphasizes cost-effectiveness and reusability, with its first stage capable of multiple landings and relaunches [19].

2.4.2 Falcon 9 Nose Cone Design

Falcon 9's payload fairing is 5.2 meters in diameter and approximately 13.1 meters in height. This fairing is built to withstand the rigors of multiple launches, recoveries, and reusability. Constructed with composite materials similar to those used in Atlas V and Delta IV, the fairing is designed to protect the payload and minimize aerodynamic drag during ascent [19]. Although specific nose cone classifications are not disclosed, the fairing's shape is engineered to reduce aerodynamic drag and ensure efficient performance across multiple flights. The overall shape of the nose cone is more round and blunt when compared to the Atlas V and Delta IV nose cone shapes. The round and blunt design choice for their nose cone is likely due to their determination

to reuse their fairing for multiple flights, thus thermal protection is highly prioritized over drag performance in this case.

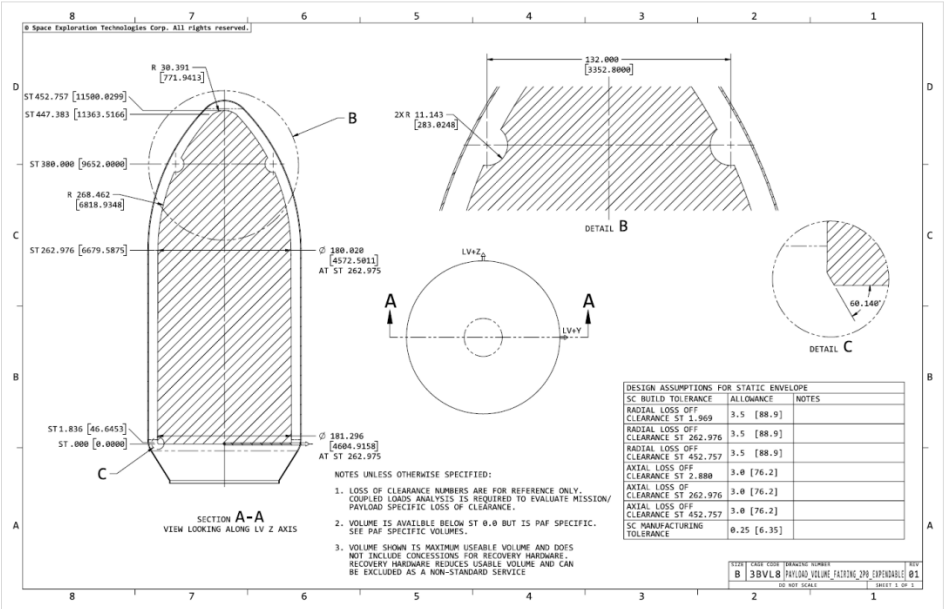

Figure 2.5 Falcon 9 fairing dimensions [19]

2.4.3 Falcon 9 Nozzle Design

The Falcon 9 uses a Merlin engine equipped with a nozzle designed for both sea-level and vacuum conditions. For the first stage, a sea-level optimized bell nozzle is used, while the second stage features a larger vacuum-optimized nozzle that maximizes efficiency in low-pressure environments. This configuration allows maximizing thrust efficiency across a range of altitudes while maintaining reusability [19].

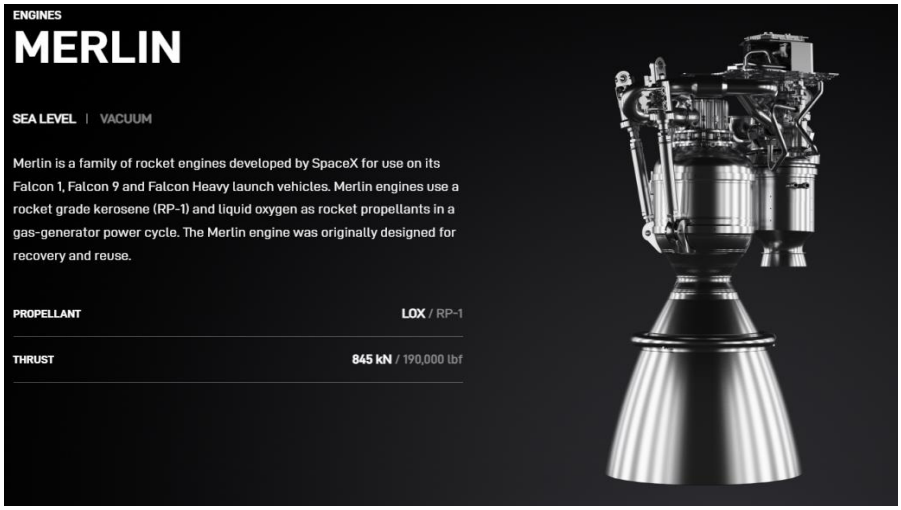

Figure 2.6 Merlin engine specifications [19]

2.4.4 Falcon 9 Material Choices

The fairing materials used in Falcon 9 include composite materials that are durable enough for multiple launches and recoveries, however, they are not directly specified by Space X. For the vacuum nozzle, SpaceX uses a niobium alloy to handle the extreme temperatures encountered in space. This material is selected for its durability and ability to withstand repeated thermal cycling, crucial for Falcon 9's reusable design [19].

2.5 A Comparative Analysis for Atlas V, Delta IV and Falcon 9

The Atlas V, Delta IV, and Falcon 9 rockets display several distinct design choices, each reflecting optimizations suited to specific mission profiles, reusability requirements, and performance goals. Both Atlas V and Delta IV utilize composite nose cones made from graphite epoxy with an aluminum honeycomb core. Their nose cone designs combine an ogive shape capped with a spherical tip, balancing aerodynamic drag reduction and thermal protection during ascent. This design choice considers payload protection and drag performance. In contrast, Falcon 9's fairing is slightly more blunt and rounded, optimized for reusability. This choice prioritizes thermal durability, enabling the fairing to withstand multiple launches and recoveries. This design aligns with SpaceX's commitment to cost-effective and reusable systems.

In terms of nozzle design and expansion ratios, Atlas V and Delta IV each use bell nozzles optimized for efficient thrust in both atmospheric and vacuum conditions. The Delta IV RS-68A engine features a bell nozzle with a 21.5:1 expansion ratio, which enhances efficiency across various altitudes [20,21]. Falcon 9, on the other hand, uses a unique two-stage approach: a sea-level optimized bell nozzle on its Merlin first-stage engine, and a vacuum-optimized nozzle for the second stage. This dual-stage configuration allows Falcon 9 to maintain high thrust efficiency in both atmospheric and low-pressure environments, which further aligns with their mission of reusability[19].

The materials chosen for nozzles and fairings illustrate each rocket's design priorities. Atlas V and Delta IV, both expendable rockets, utilize carbon phenolic and carbon-carbon composites in their nozzles, materials well-suited for single-use applications due to their durability and high thermal resistance [20,21]. Falcon 9, in contrast, uses niobium alloy in its vacuum-optimized nozzle to withstand multiple thermal cycles and maintain structural integrity across several missions. The fairing materials used in Falcon 9, though undisclosed, are likely engineered to endure repeated recoveries and launches, favoring reusability over minimal weight [19]. This analysis underlines how Delta IV and Atlas V prioritize structural integrity and thermal protection for heavy-lift missions, whereas Falcon 9 seeks a balance of efficiency and reusability, incorporating materials and designs that withstand the demands of multiple flights.

2.6 Set up for Chapter 3

For the next chapter, the goal will be to design a nose cone and nozzle using either Solid Works or 3D Inventor, with the data gathered from this chapter. One specific rocket will be picked and a nose cone along with a nozzle will be designed, keeping in mind its mission requirements. Based on the literature review from Chapter 1, the information there regarding aerospike and aero-disk designs for the nose cone and nozzle will be entertained in combination with the information learned in this chapter.

Chapter 3. CFD Analysis of Falcon 9 Nose Cone Configuration

3.1 A CFD analysis on the Falcon 9 nose cone

In this chapter, an intermediate Computational Fluid Dynamics (CFD) analysis was conducted for the Falcon 9's(F9) nose cone(NC), with three different configurations consisting of a blunt(original design for the F9 Nose cone), aerospike and aerodisk design. The purpose of this chapter is to compute this CFD analysis to assess which configuration results in a minimum drag given the same boundary conditions.

3.2 Geometry set up

The geometry was created using the software Autodesk Inventor, similar to other engineering software designer tools like Solidworks and Fusion360. Following the 2D drawings from the F9 user manual and SpaceX website [19], the geometry was simply created first by sketching half of the F9 NC on a plane. After finalizing the sketch, the 2D geometry was revolved around the mid axis of the NC, resulting in a 3D model of F9 NC displayed on figure 3.1.

Figure 3.1 F9 NC 3D model

Using the same model, an aerospike and aerodisk were implemented respectively by following similar strategies as mentioned previously. A sketch of the aerospike was made on the midplane of the 3D model for the F9 NC, then it was revolved around the center axis to create the

3D model for the aerospike. The same steps were taken to create the 3D model of the F9 NC with an aerodisk configuration, both configurations are displayed in figures 3.2 and 3.3 respectively.

Figure 3.2 Aerospike configuration

Figure 3.3 Aerodisk configuration

The three NC configurations were exported as a .step file and imported to ANSYS to finalize the geometry for this analysis. Using the ANSYS (fluid flow) design modeler, a rectangular prism was generated around the imported NC, with a fixed distance of ~25 m in all directions, except for the top and bottom faces, which were set to be ~30 meters. Then, a boolean operation was performed to subtract the imported NC geometry and the rectangular prism, with the result being the rectangular prism, and at the center of it a cutout of the NC geometry with the result illustrated on figure 3.4. This resultant geometry will essentially be the fluid domain where our CFD will be conducted.

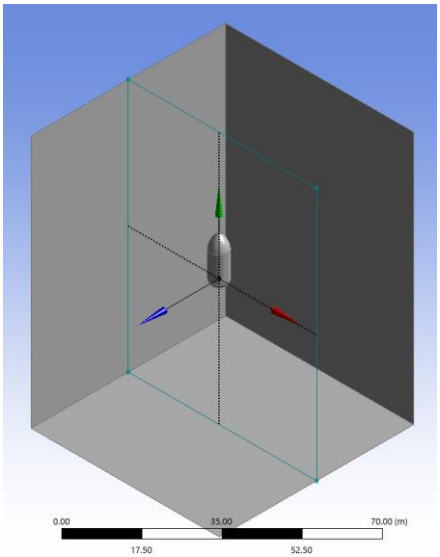

Figure 3.4 Resultant geometry of boolean subtract operation

3.3 Mesh set up

Before setting up the mesh, the resultant geometry from the previous section was split into different faces and were set a name/region. The cut out of the NC is pointing up in the positive-Y-direction, meaning that the inlet would be assigned on the top face of the domain(resultant geometry) and the bottom face would be the outlet. All other four faces would act as a wall, and the cut out surface will additionally act as a wall. Performing these steps before continuing with the mesh eases the process later on when we set up the boundary conditions.

The next step would be to conduct an automated mesh of the whole domain. After it is generated, some refinement will be necessary on certain locations of the domain, more specifically, near the NC cutout surface. Firstly, the element size of the whole domain will be increased to 1.5 m, rather than 0.5 m, due to it being computationally intense due to its large domain. The elements are triangular to increase simulation and mesh computational efficiency and also due to the restrictions of element quantities allowed using a student version of ANSYS. The growth rate will be increased from 1.05 to 1.2, to reduce the increase in the overall size of the elements near the wall regions of the domain that are acting as walls. And to now refine the NC cutout, essentially all the previously mentioned parameters will be decreased in order to create more elements at that location, and the result is shown on figures 3.5, 3.6 and 3.7.

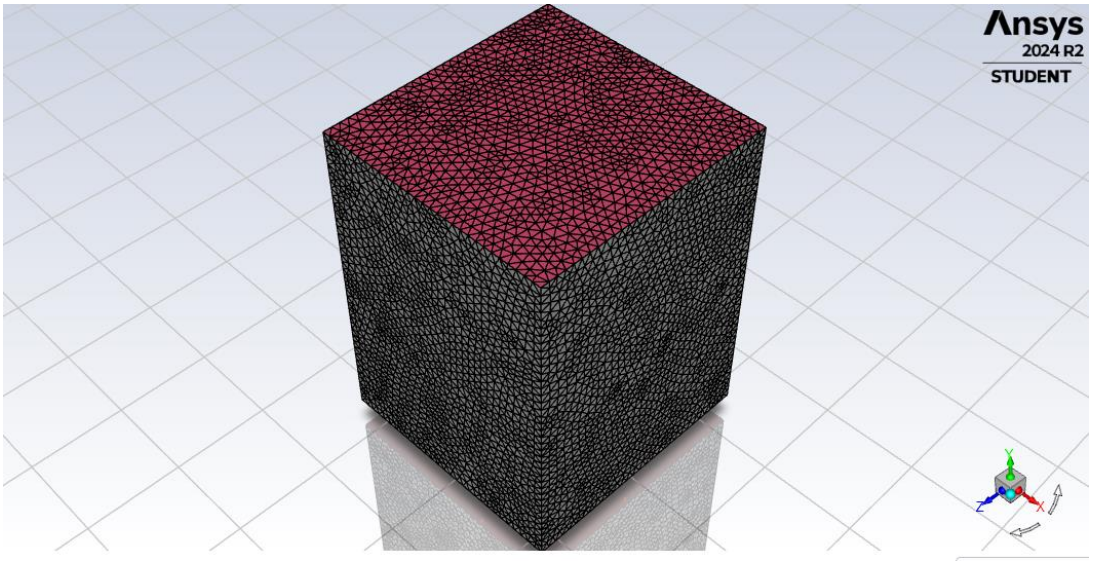

Figure 3.5 Finalized mesh of the domain

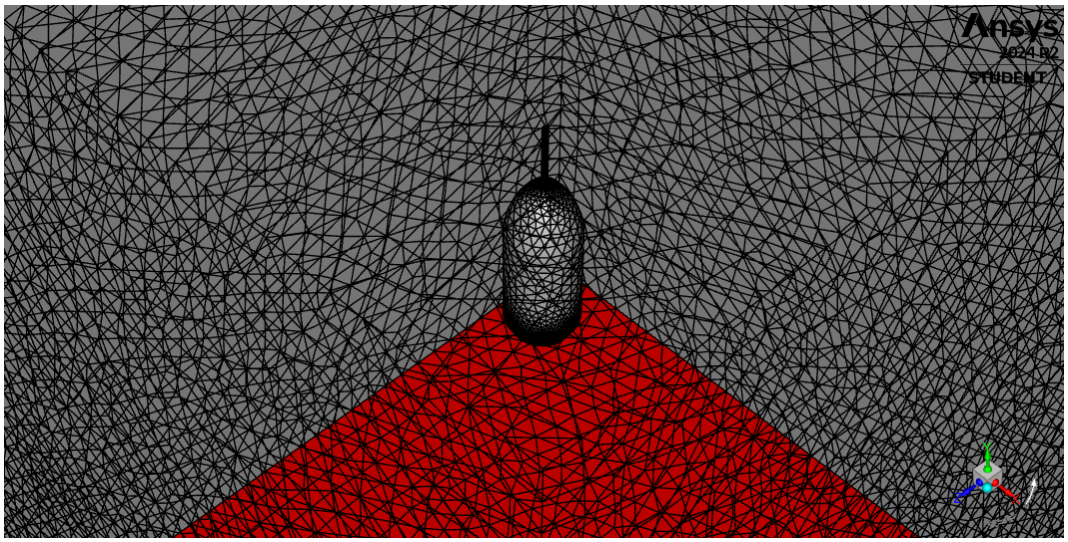

Figure 3.6 Zoomed in view inside the mesh domain

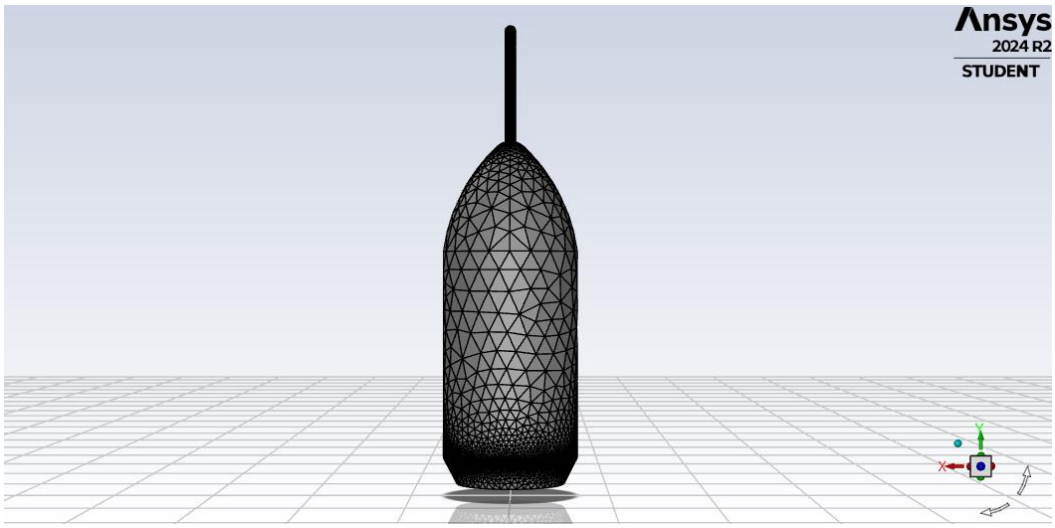

Figure 3.7 Isolated view of NC mesh

With respect to the aerospike and aerodisk geometries, their mesh is refined similarly as explained previously, and an example of how the mesh is generated is displayed on figure 3.8

Figure 3.8 Isolated view of NC aerospike mesh

3.4 Physics and Continua

This section will cover the physics behind the simulation and go over the set up to achieve reasonable results.

3.4.1 Governing Equations

The CFD simulations for the F9 NC are based on solving the compressible Navier-Stokes equations. These equations describe the conservation of mass, momentum, and energy in the flow field and are essential for accurately modeling high-speed aerodynamic behavior.

3.4.1.1 Continuity Equation (Mass Conservation)

$$\partial\rho/\partial t + \nabla \cdot (\rho\vec{u}) = \boldsymbol{0} \tag{3.1}$$

where ρ is the fluid density and u is the velocity vector.

3.4.1.2 Momentum Equation (Newton's Second Law)

$$\partial(\rho\vec{u})/\partial(t) + \nabla \cdot (\rho\vec{u}\vec{u}) = -\nabla p + \nabla \cdot \boldsymbol{\tau} + \rho g \tag{3.2}$$

where ρ is the pressure, τ is the viscous stress tensor, and g is the gravitational acceleration vector.

3.4.1.3 Energy Equation

$$\partial(\rho E)/\partial(t) + \nabla \cdot (\rho\vec{u}(E + p/\rho)) = \nabla \cdot (k\nabla T) + \Phi \tag{3.3}$$

where E is the total specific energy ($E = e + \boldsymbol{0.5} \cdot |u|^2$), k is the thermal conductivity, T is the temperature, and Φ is the viscous dissipation term.

These equations collectively account for the compressibility of the fluid, viscous effects, and thermal transport, which are critical for analyzing the aerodynamic performance of the nose cone at supersonic speeds.

3.4.2 Turbulence Modeling

For high-speed aerodynamic simulations, it is essential to accurately capture turbulent flow characteristics, particularly around the nose cone where shock waves and boundary layer separation occur.

In this study, the k-ω Shear Stress Transport (SST) turbulence model is used due to its ability to accurately predict boundary layer separation under adverse pressure gradients. It is also able to perform well in both the near-wall region (k-ω formulation) and the free-stream region (k-ε formulation). Lastly, it will provide reliable results for supersonic and hypersonic flows. The transport equations for the k-ω SST model are as follow:

Turbulent Kinetic Energy (k) Equation

$$\partial(\rho k)/\partial(t) + \nabla \cdot (\rho k\vec{u}) = \nabla \cdot (\Gamma_k \nabla k \ ) + G_k - Y_k + S_k \tag{3.4}$$

Specific Dissipation Rate (ω) Equation

$$\partial(\rho\omega)/\partial(t) + \nabla \cdot (\rho\omega\vec{u}) = \nabla \cdot (\Gamma \ _\omega \nabla\omega) + G_\omega - Y_\omega + S_\omega \tag{3.5}$$

where $G_k$and G_ω represent the generation of turbulent kinetic energy and specific dissipation rate, Y_k and Y_ω are the dissipation terms, andΓ_k and $\Gamma \ _\omega$ are the effective diffusivities. Figure 3.9 highlights the previously mentioned physics applied in the set up box of the simulation.

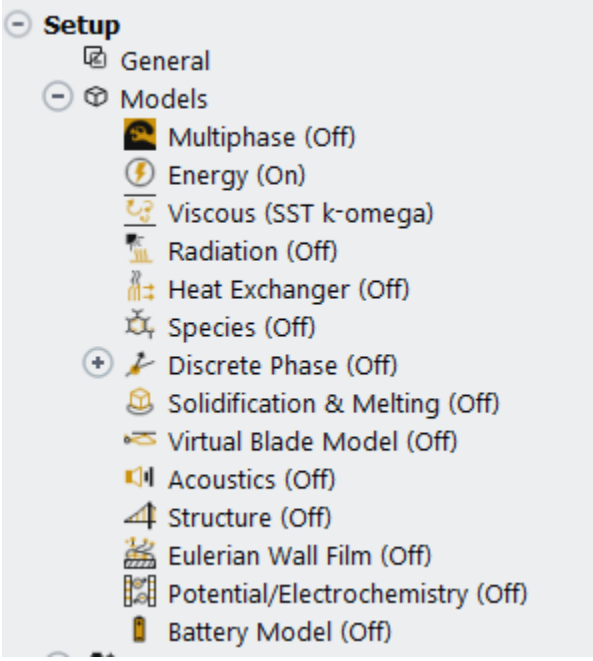

Figure 3.9 Set up box for F9 NC CFD simulation

3.4.3 Boundary Conditions

The following boundary conditions are applied in the CFD simulations to ensure accurate representation of the aerodynamic environment around the Falcon 9 nose cone. At the inlet, a velocity inlet condition is specified with a velocity magnitude of approximately 896 m/s, corresponding to a freestream Mach number of 2. The inlet temperature is set to 500 K to account for compressible heating effects typically encountered in supersonic flow conditions. The outlet is defined as a pressure outlet with a pressure of 50,000 Pa, which represents the atmospheric conditions at an altitude of approximately 5 km (16,400 feet), where ambient pressure is significantly lower than at sea level. The walls of the nose cone and the four faces (excludes inlet and outlet faces of domain) around the nose cone are modeled as no-slip walls with an adiabatic thermal condition. Finally, a pressure far-field boundary condition is applied to avoid reflections of shock waves and ensure that the computational domain adequately represents the open-air environment surrounding the nose cone during supersonic flight.

3.4.4 Assumptions

The following assumptions are made to simplify the simulations and ensure computational efficiency while maintaining accuracy. The fluid is treated as compressible due to the high-speed conditions encountered in supersonic flight. Air is modeled as an ideal gas with temperature-dependent properties to account for variations in density and pressure. The simulations are conducted as transient flow analyses to capture unsteady phenomena such as vortex shedding and shockwave oscillations that may occur around the nose cone. Additionally, the nose cone surface is assumed to be adiabatic, meaning no heat transfer occurs through the surface, unless otherwise specified in specific scenarios.

3.4.5 Equations for Drag Coefficient

The drag coefficient (C_D) quantifies the aerodynamic drag on the nose cone and is calculated as:

$$C_D = D/(0.5 \cdot \rho \cdot U^2 \cdot A) \tag{3.6}$$

where D is the drag force in Newtons, ρ is freestream air density in kg/m³, U represents freestream velocity m/s, and lastly A is the Reference area in m².

3.5 Simulation Results

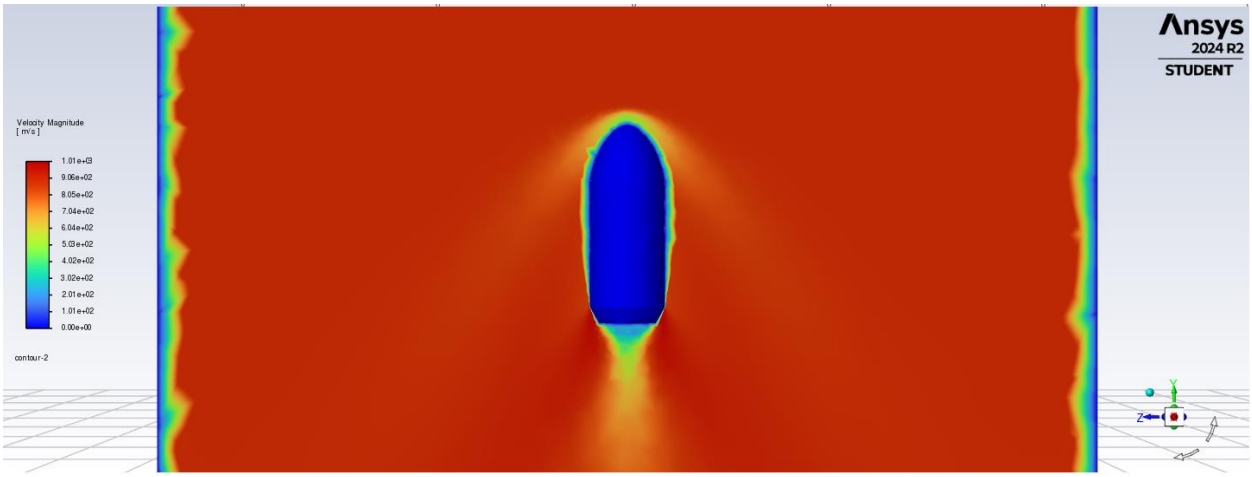

Figure 3.10 Blunt NC velocity magnitude contour plane

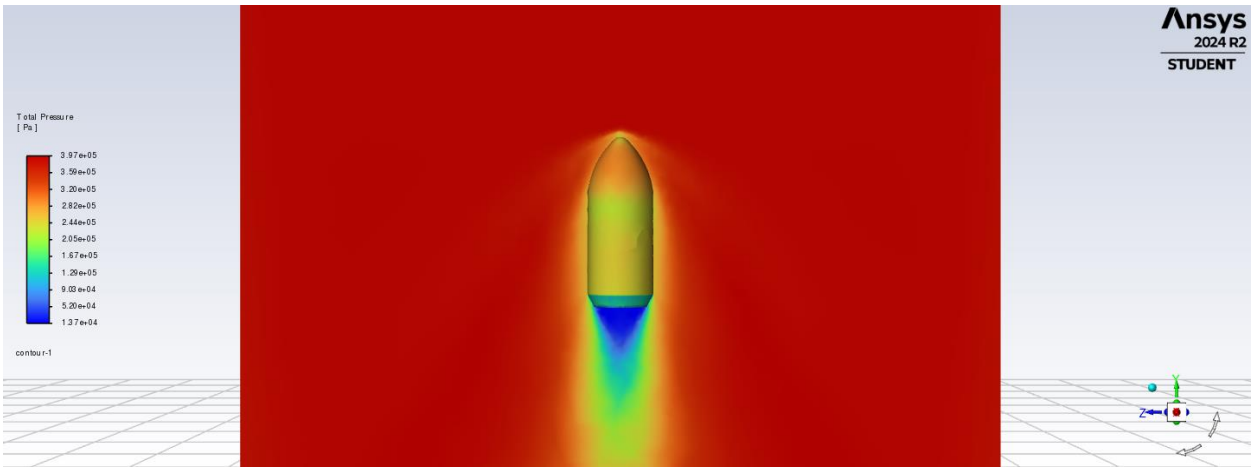

Figure 3.11 Blunt NC total pressure contour plane

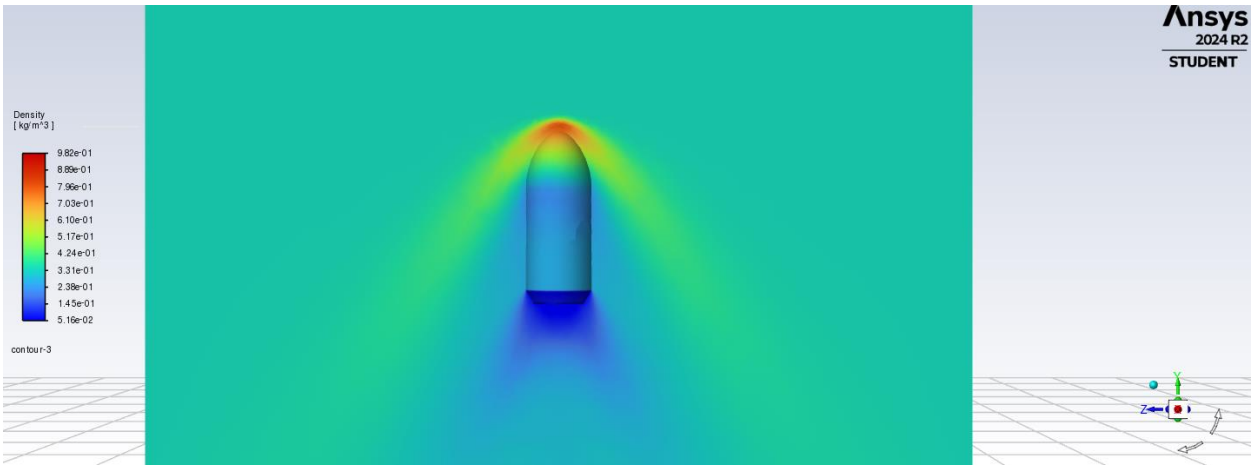

Figure 3.12 Blunt NC density contour plane

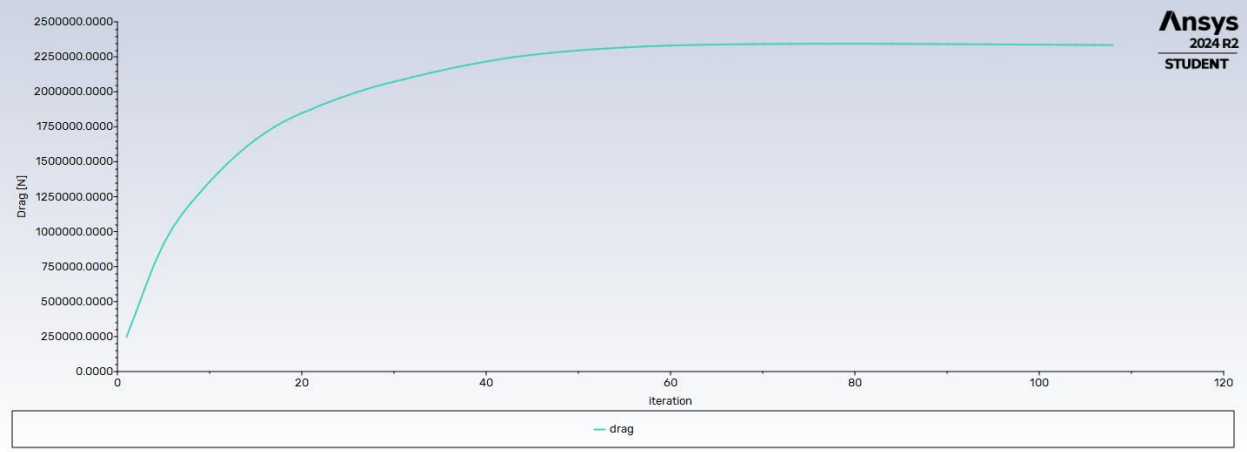

Figure 3.13 Blunt NC drag curve

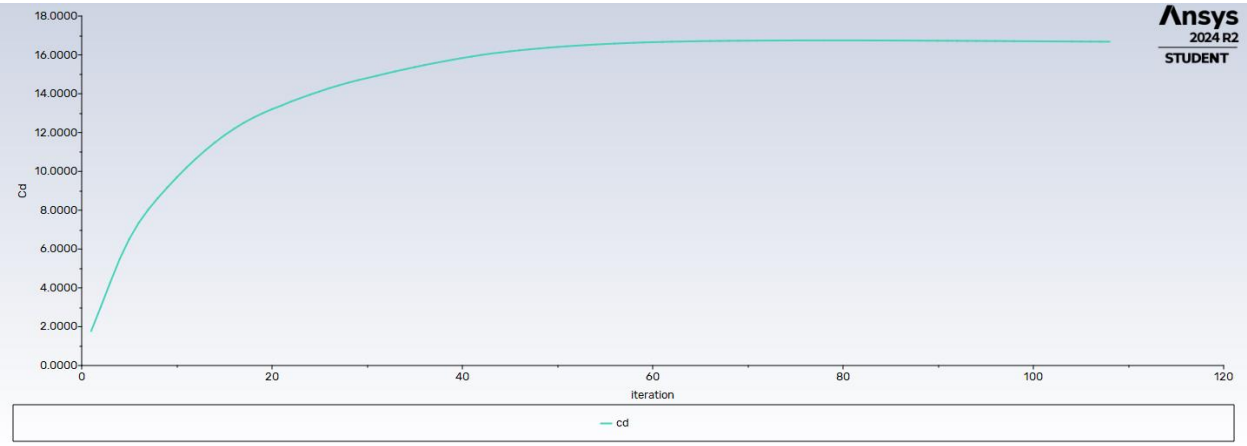

Figure 3.14 Blunt NC coefficient of drag curve

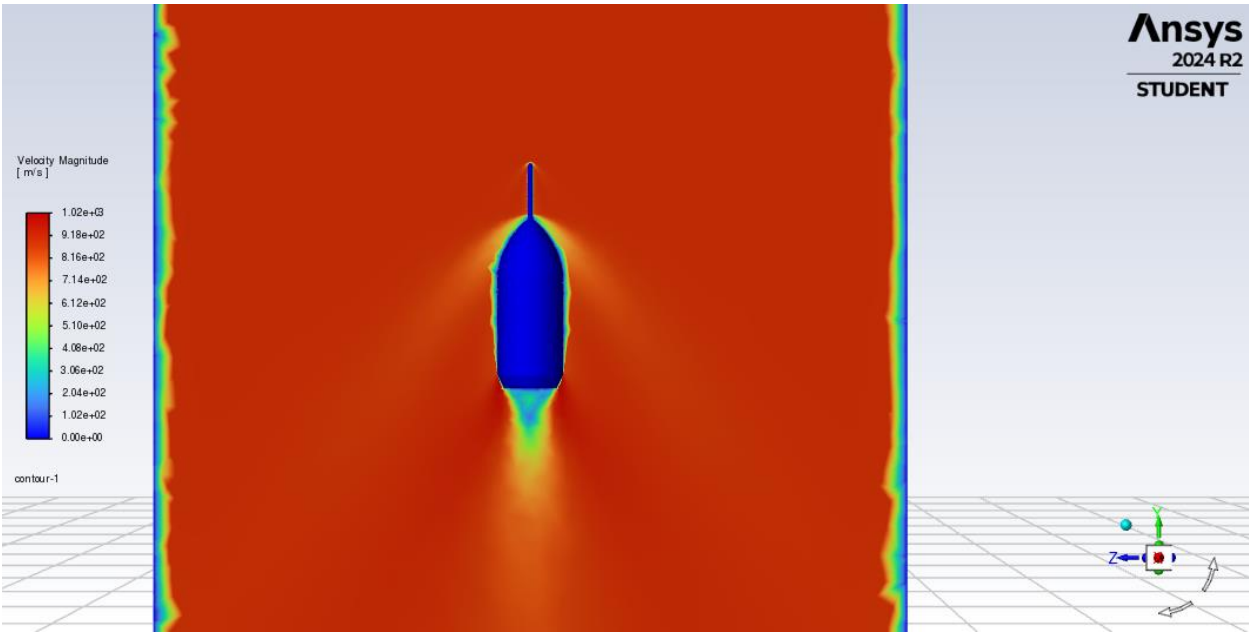

Figure 3.15 Aerospike NC velocity contour plane

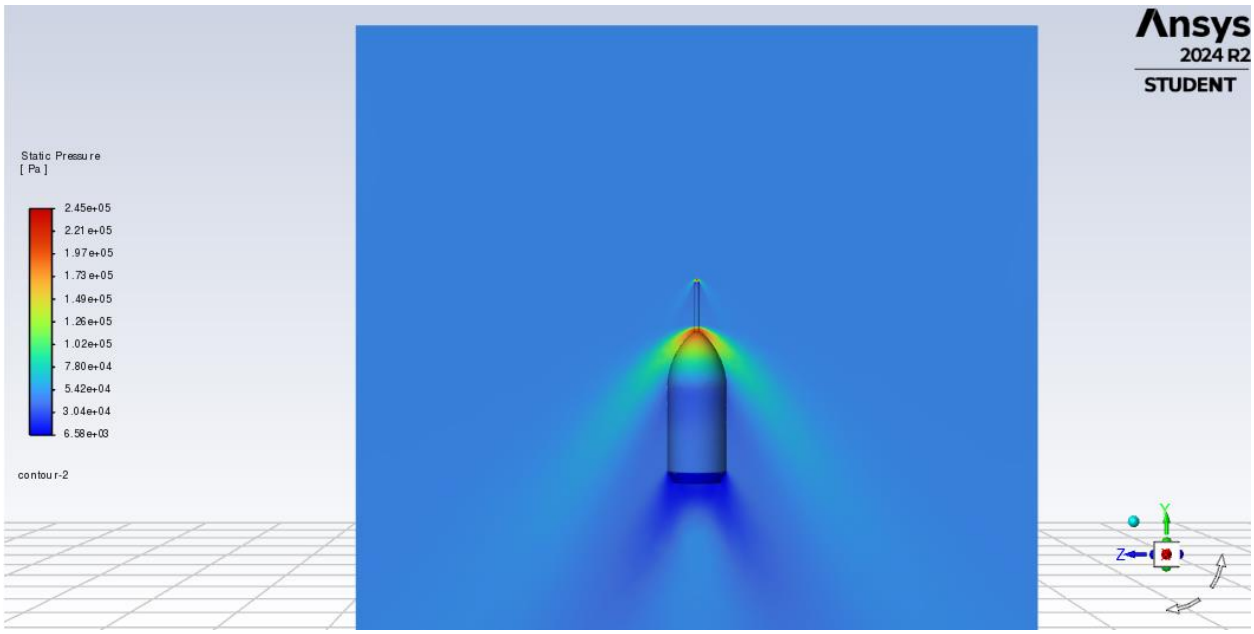

Figure 3.16 Aerospike NC total pressure contour plane

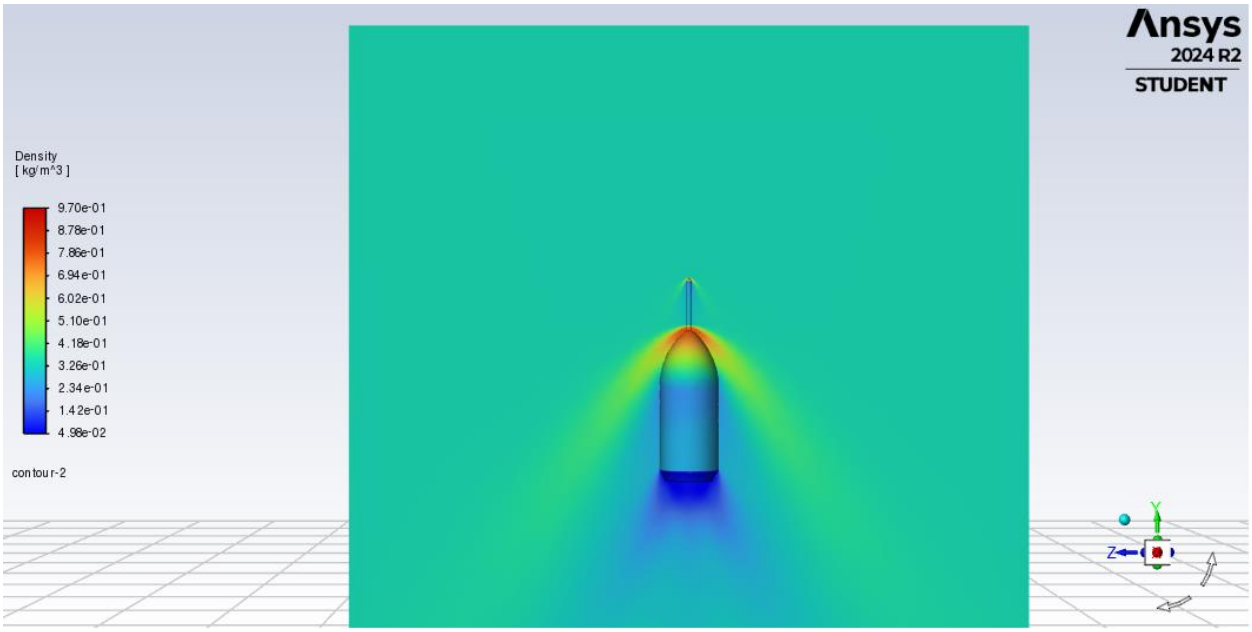

Figure 3.17 Aerospike NC density contour plane

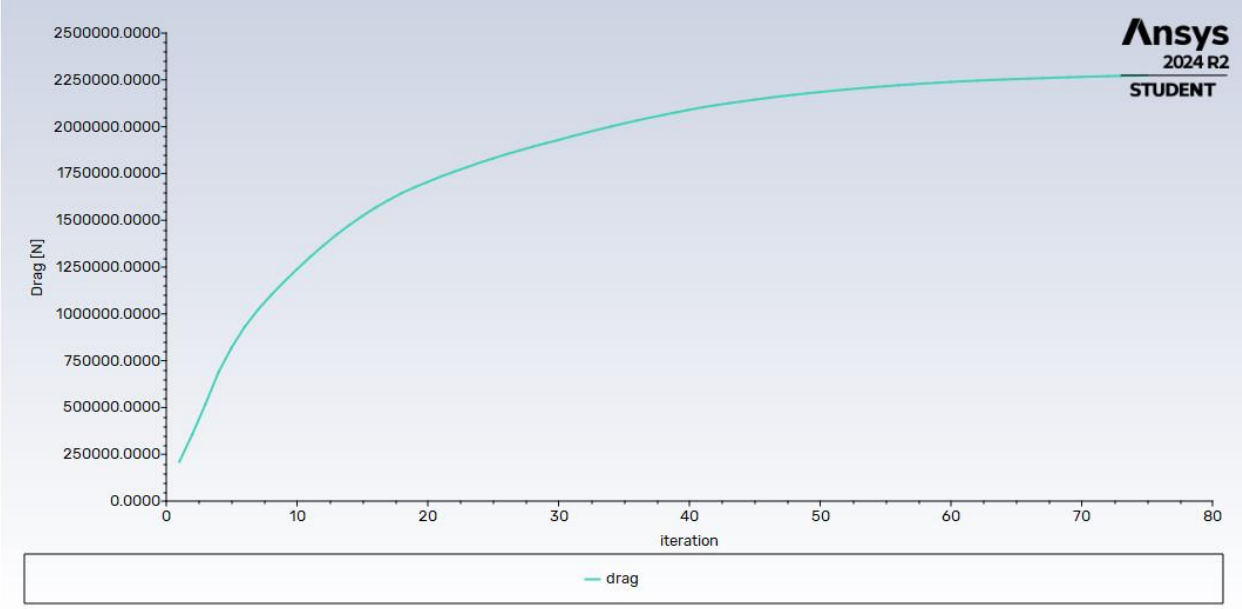

Figure 3.18 Aerospike NC drag curve

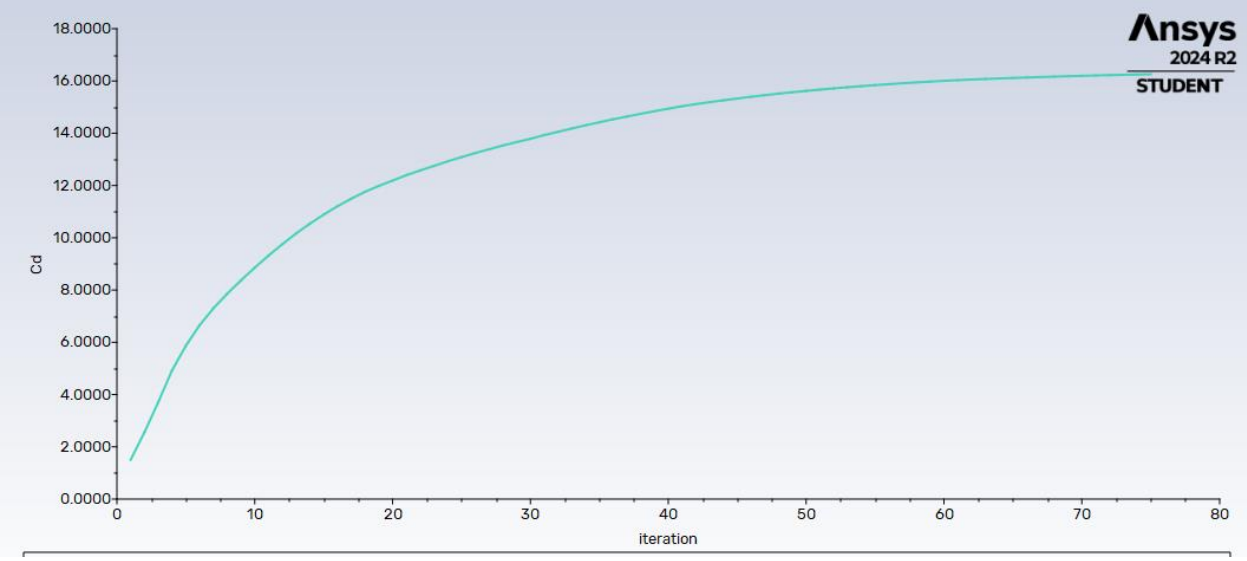

Figure 3.19 Aerospike NC coefficient of drag curve

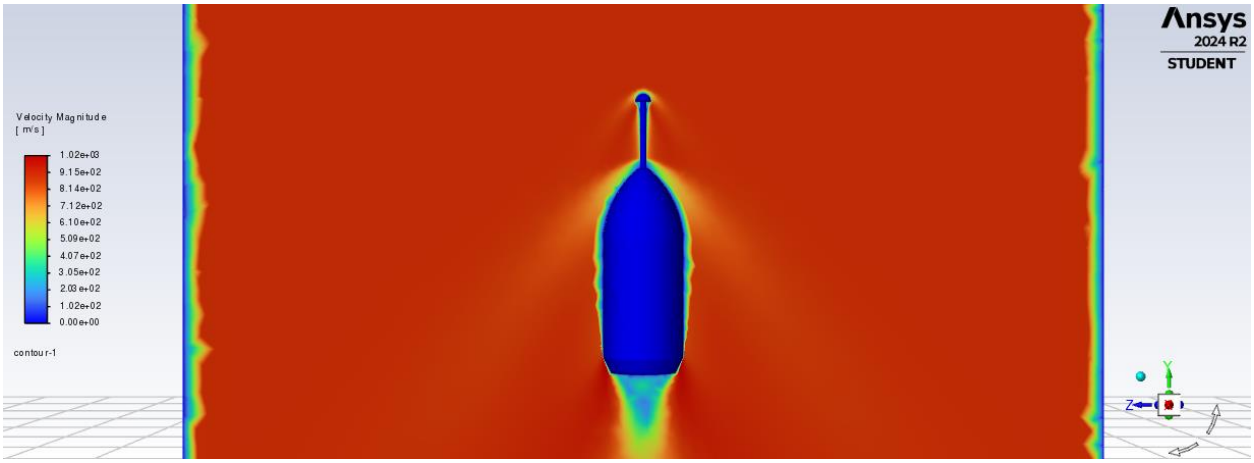

Figure 3.20 Aerodisk NC velocity contour plane

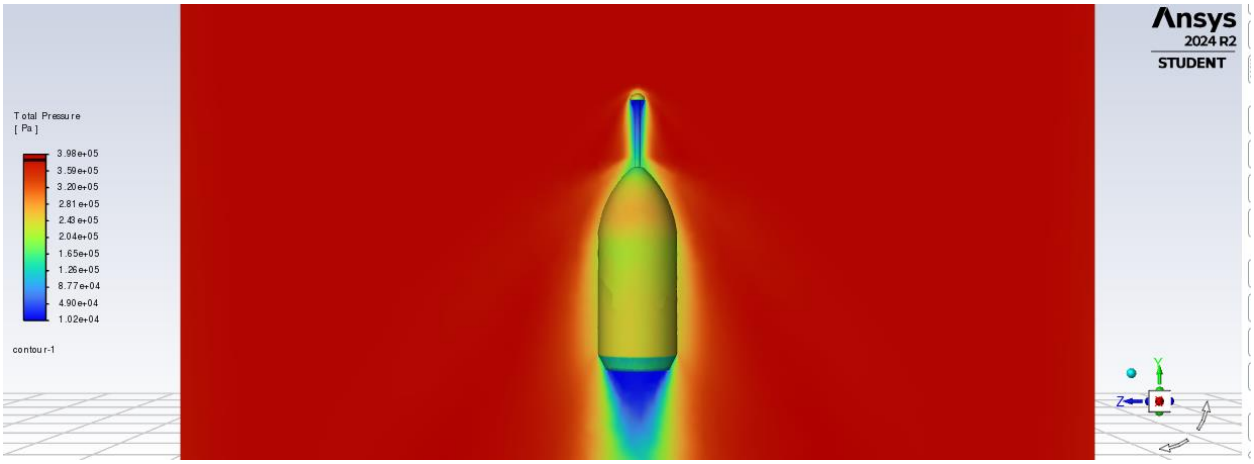

Figure 3.21 Aerodisk NC total pressure contour plane

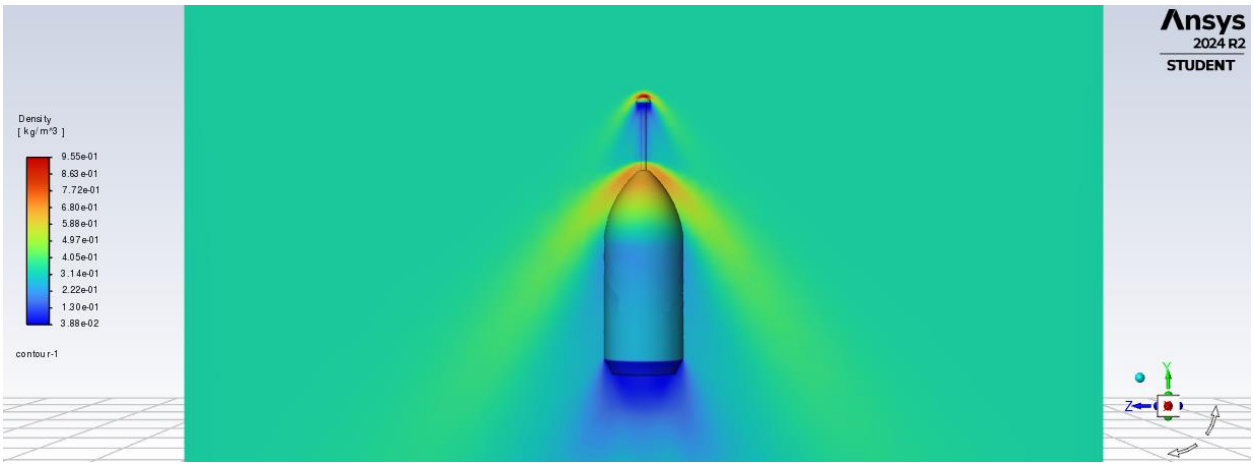

Figure 3.22 Aerodisk NC density contour plane

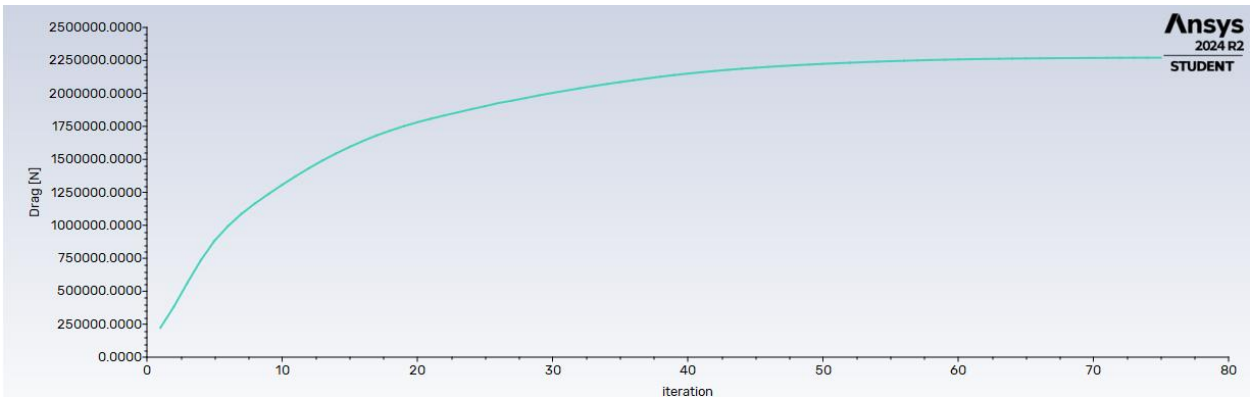

Figure 3.23 Aerodisk NC drag curve

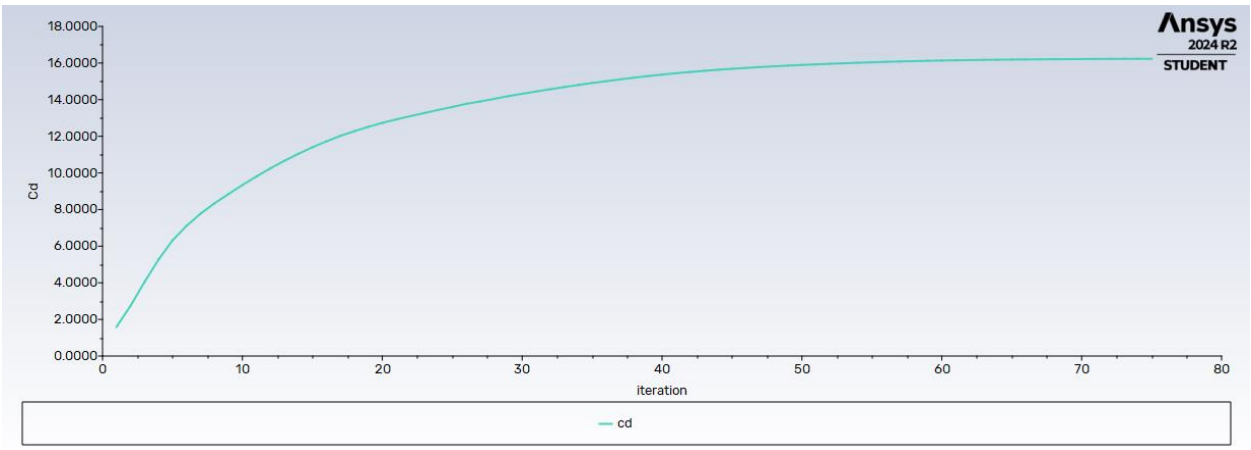

Figure 3.24 Aerodisk NC coefficient of drag curve

3.6 Discussion

The simulation results for the three nose cone configurations — the standard F9 blunt NC, the aerospike configuration, and the aerodisk configuration — reveal significant differences in velocity, total pressure, and density distributions. These results align closely with the findings from another study and validate the aerodynamic performance of the aerodisk as the best drag-reducing configuration [10].

For the blunt nose cone configuration, the velocity distribution illustrated on figure 3.10 reveals the formation of a strong detached bow shock ahead of the nose cone. This shock causes a significant decrease in velocity near the stagnation point, resulting in a region of elevated pressure that increases aerodynamic drag. Downstream of the nose cone, the total pressure illustrated on figure 3.11 decreases abruptly, very similarly to Balusamy, K. et al. [10] study, and they claim it can be attributed to the extensive recirculation zone and the wake region. The density plane contours on figure 3.12 illustrate a concentrated high-density area at the stagnation point, further contributing to the overall drag. These result simulations align with the baseline drag characteristics noted by Balusamy, K. et al. [10], where blunt bodies generate higher drag due to the strong bow shock and the resulting pressure differences.

In the aerospike configuration, the addition of the spike reduces the strength of the bow shock by transforming it into a weaker oblique shock. This alteration allows higher velocities to persist in the recirculation region behind the spike. The total pressure displayed on figure 3.16 depicts that the total pressure drop behind the nose cone is less severe compared to the blunt nose cone, leading to reduced pressure drag. The density plane contour on figure 3.17 shows a moderated pressure gradient near the nose, effectively shaping the flow into a conical form and decreasing drag.

The aerodisk configuration demonstrates the best overall performance in terms of drag reduction. The velocity distribution on figure 3.20 shows a larger and more effective recirculation region behind the aerodisk, resulting in a weaker bow shock compared to the aerospike. This configuration maintains higher velocities near the surface of the nose cone. The total pressure drops behind the aerodisk is more emphasized, as illustrated on figure 3.21, which implies that drag is significantly decreased. The density plane contour plane shown on figure 3.22 exhibits a reduction in the pressure gradient downstream of the disk, which minimizes the drag coefficient. This closely matches the results of the current simulations, reinforcing the aerodisk's effectiveness [10].

The comparison of these configurations illustrates how modifications to the nose cone shape influence the aerodynamic characteristics, particularly by altering the shockwave patterns and flow structures. The simulation results validate the aerodisk's ability to reduce drag significantly, supporting the findings presented in the literature [10]. This agreement emphasizes the potential of aerodisk configurations to enhance the aerodynamic efficiency of rocket nose cones, which will be the focus of the next chapter.

Chapter 4. Parametric Optimization of Aerodisk Nose Cones

4.1 Introduction

Building upon the computational fluid dynamics (CFD) analyses conducted in Chapter 3, this chapter expands on the investigation of nose cone (NC) aerodynamics by focusing specifically on the aerodisk nose cone concept. The primary objective of this study is to evaluate how variations in aerodisk length and width influence the aerodynamic performance of the nose cone, with a focus on minimizing drag. The aerodisk concept is a promising method for reducing the aerodynamic drag experienced by high-speed vehicles, particularly in supersonic and hypersonic flight regimes. By altering the dimensions of the aerodisk, such as its length and width, the overall flow characteristics around the nose cone can be manipulated, potentially leading to significant performance improvements. The simulations in this chapter aim to identify the optimal aerodisk configuration by analyzing multiple flow parameters, including Mach number distributions, pressure contours, density variations, and temperature effects.

4.2 Methodology

4.2.1 Computational Setup

The CFD simulations conducted in this chapter follow a methodology similar to that used in Chapter 3, ensuring consistency in approach and comparability of results. The aerodynamic behavior of the aerodisk nose cone is analyzed using ANSYS Fluent, with a compressible flow solver applied to capture supersonic flow characteristics.

4.2.2 Geometric Configurations

Five different aerodisk configurations are considered in this study, each representing a unique combination of length and width. These configurations are as follows:

(1) (2) (3) (4) (5)

Figure 4.1 NC Aerodisk Configurations

Table 4.1 NC aerodisk configuration parameters

Configuration #	NC Aerodisk Length	NC Length	NC Aerodisk Diameter	NC Max Diameter	Length of aerodisk as a % of NC Length	Diameter of aerodisk as a % of NC Diameter
1	**4.319**	**13.25**	**1**	**5.2**	**32.60%**	**19.23%**
2	**4.319**	**13.25**	**0.5**	**5.2**	**32.60%**	**9.62%**
3	**2.569**	**13.25**	**1**	**5.2**	**19.39%**	**19.23%**
4	**8.819**	**13.25**	**1**	**5.2**	**66.56%**	**19.23%**
5	**4.139**	**13.25**	**2**	**5.2**	**31.24%**	**38.46%**

These configurations will enable us to determine how aerodisk dimensions influence aerodynamic performance, particularly with respect to minimizing drag, through CFD simulation comparisons of Mach, pressure, density, and temperature contour distributions.

4.2.3 Simulation Parameters

Each simulation is conducted under supersonic flow conditions, similar to the ones used in the previous chapter. The primary simulation parameters include a Mach number of 2.5, representative of supersonic flight conditions. The simulations employ a density-based compressible solver with turbulence modeling to accurately capture high-speed aerodynamic effects. Boundary conditions consist of a velocity inlet set to the freestream Mach number, a pressure outlet maintained at ambient atmospheric pressure, and adiabatic no-slip wall conditions applied to the nose cone surface. To ensure precise resolution of shock structures and flow separations, an unstructured mesh configuration is used, with refined grid elements concentrated around the aerodisk and nose cone regions. This setup provides a detailed computational environment that enables accurate assessment of the aerodynamic performance of each aerodisk configuration.

4.3 Simulation Results

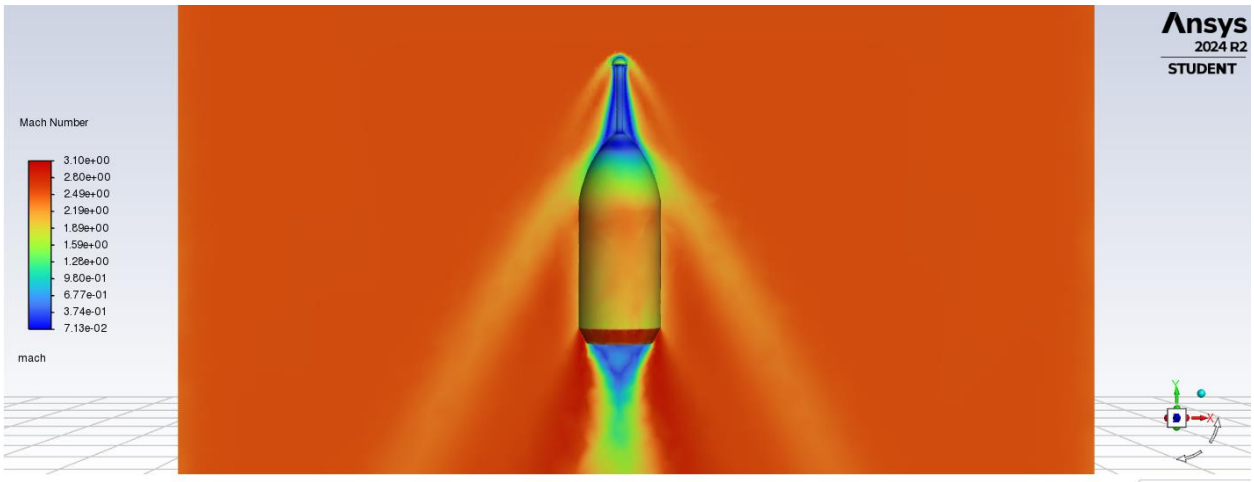

Figure 4.2 NC configuration (1) mach contour distribution

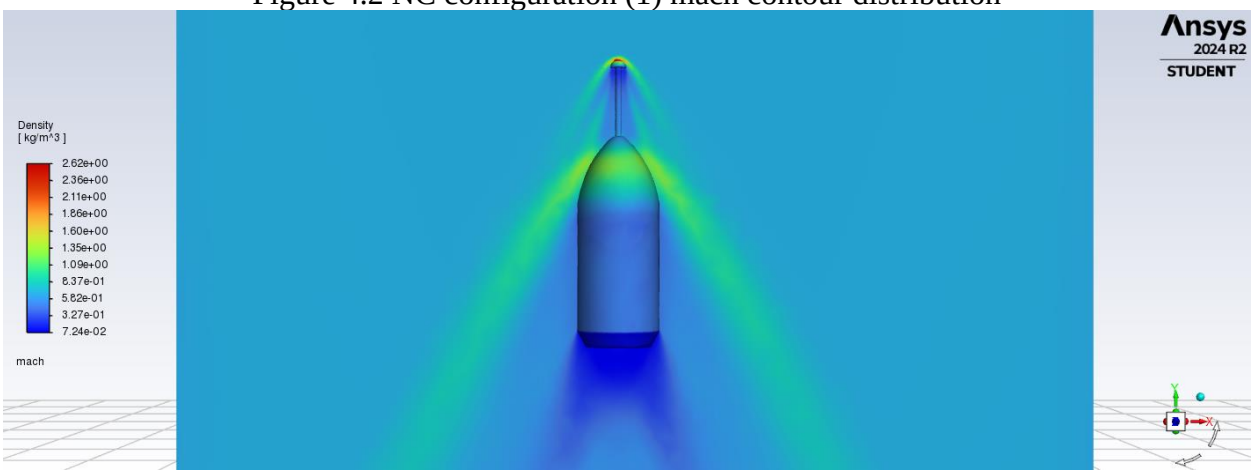

Figure 4.3 NC configuration (1) density contour distribution

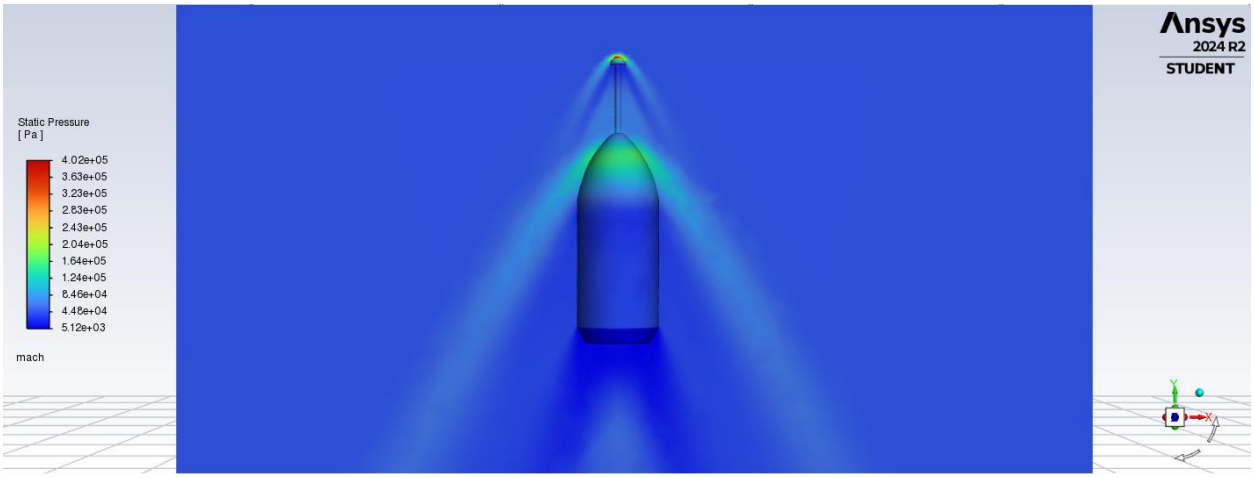

Figure 4.4 NC configuration (1) static pressure contour distribution

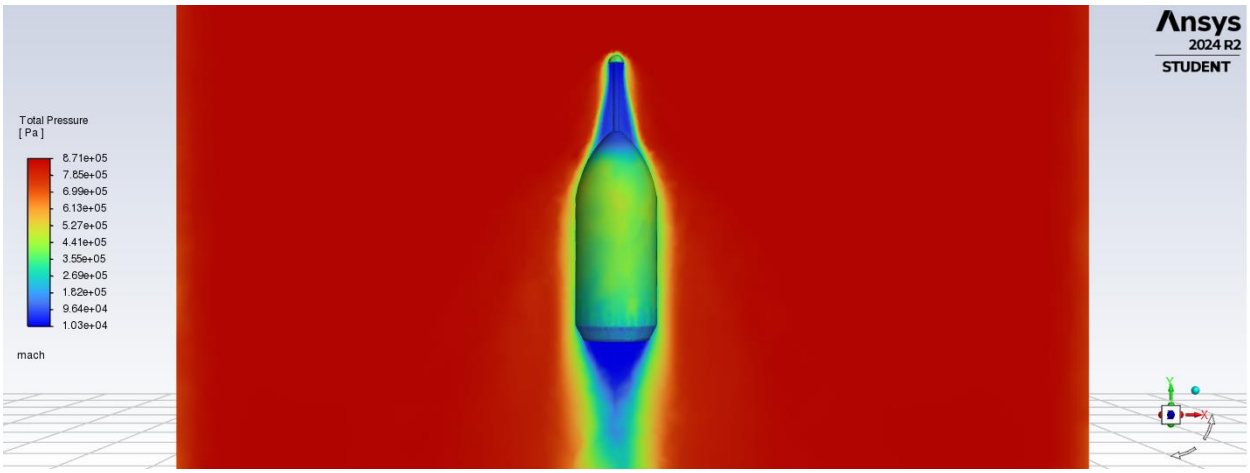

Figure 4.5 NC configuration (1) total pressure contour distribution

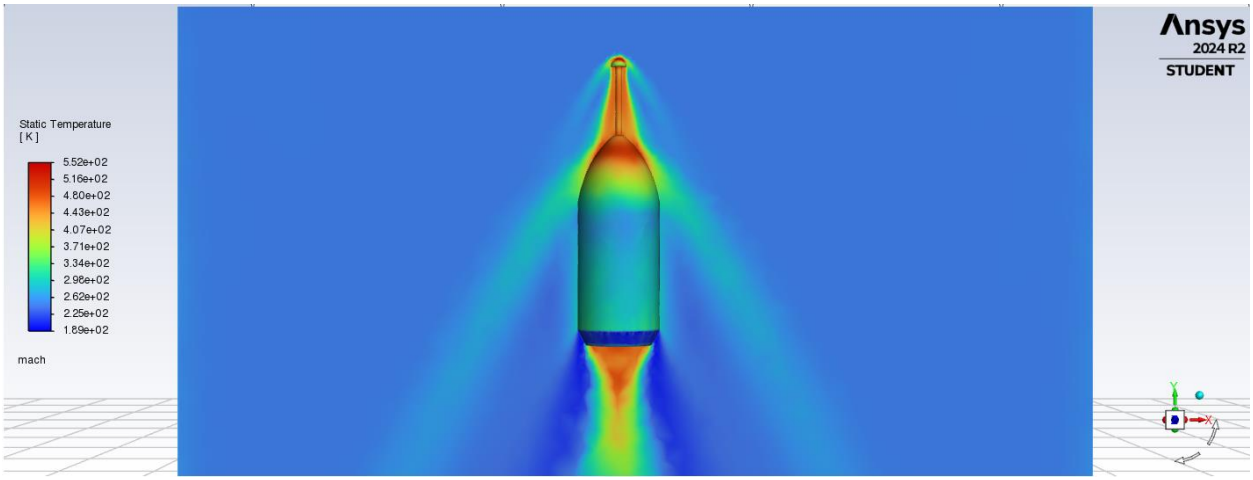

Figure 4.6 NC configuration (1) static temperature contour distribution

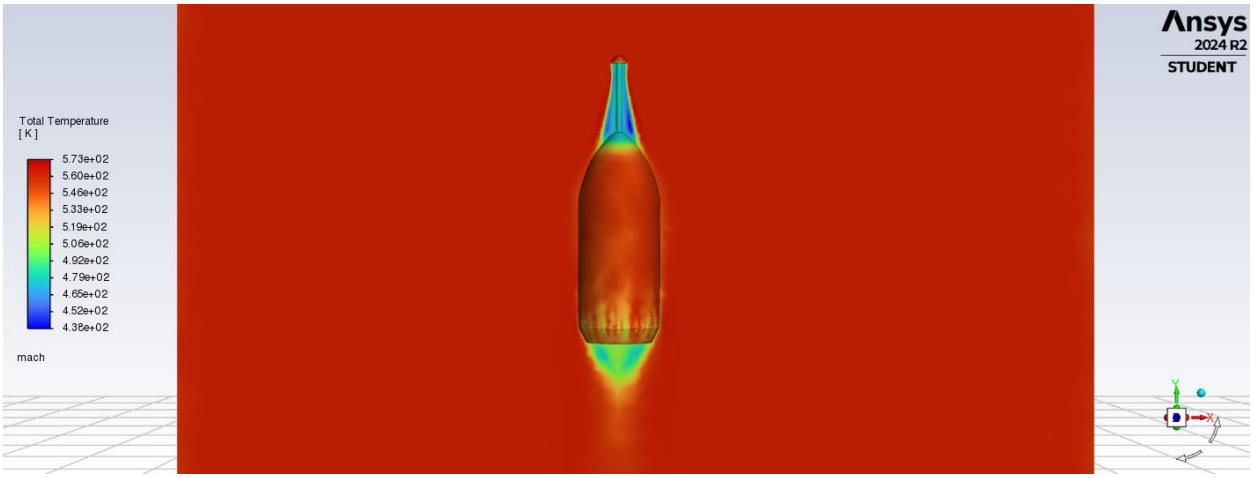

Figure 4.7 NC configuration (1) total temperature contour distribution

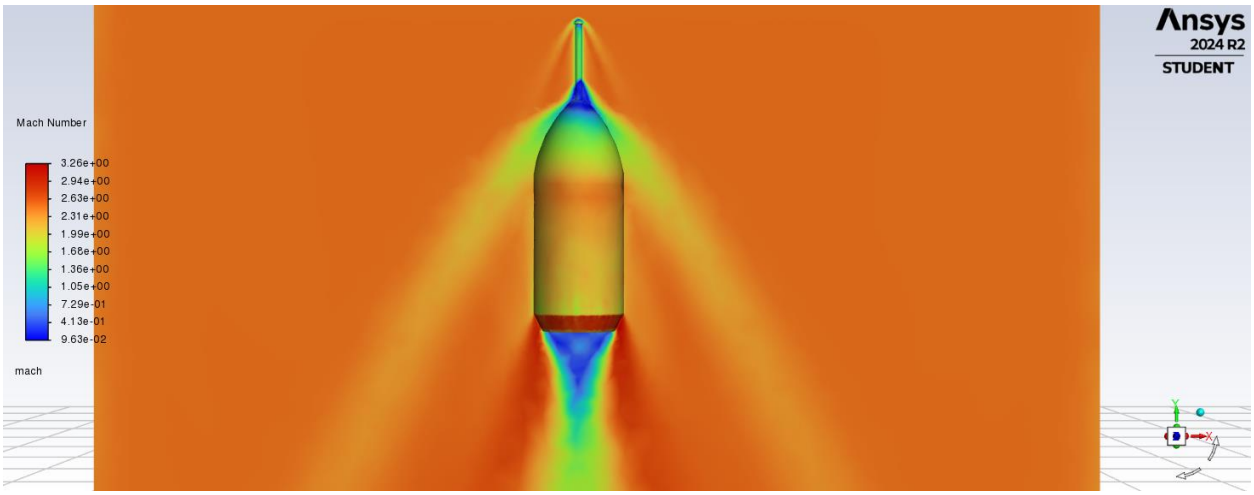

Figure 4.8 NC configuration (2) mach contour distribution

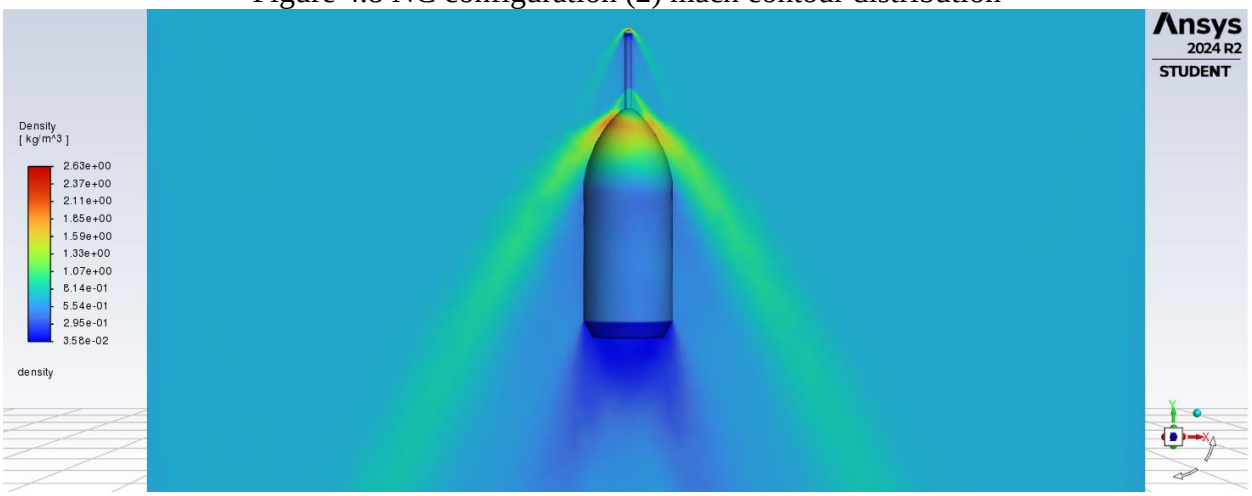

Figure 4.9 NC configuration (2) density contour distribution

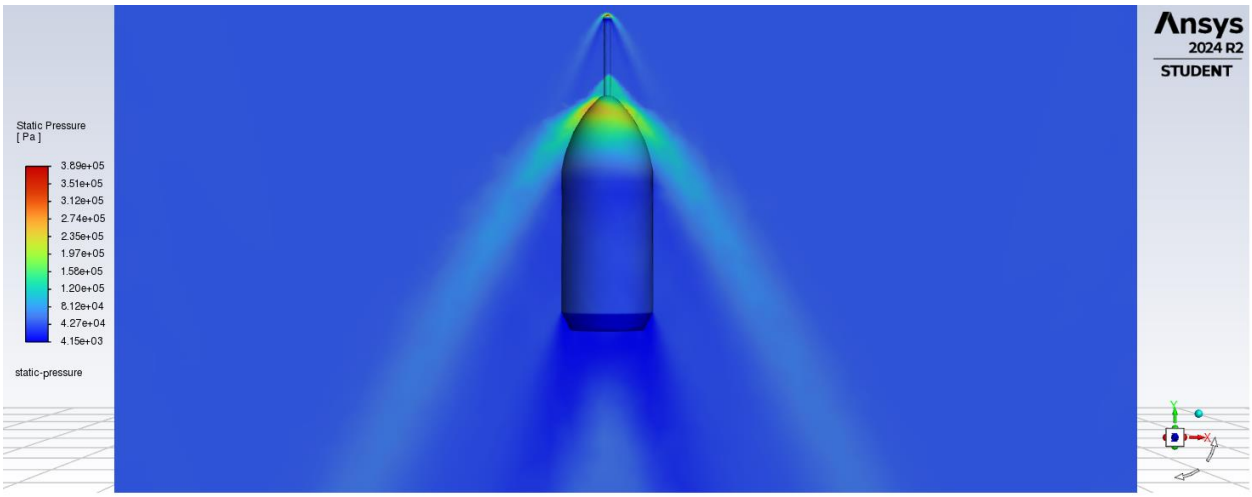

Figure 4.10 NC configuration (2) static pressure contour distribution

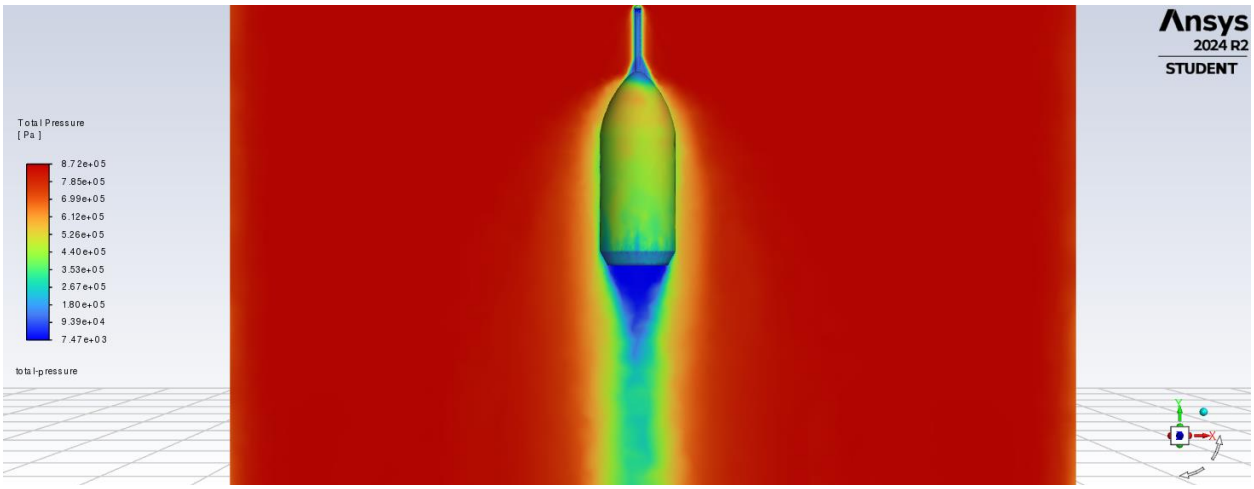

Figure 4.11 NC configuration (2) total pressure contour distribution

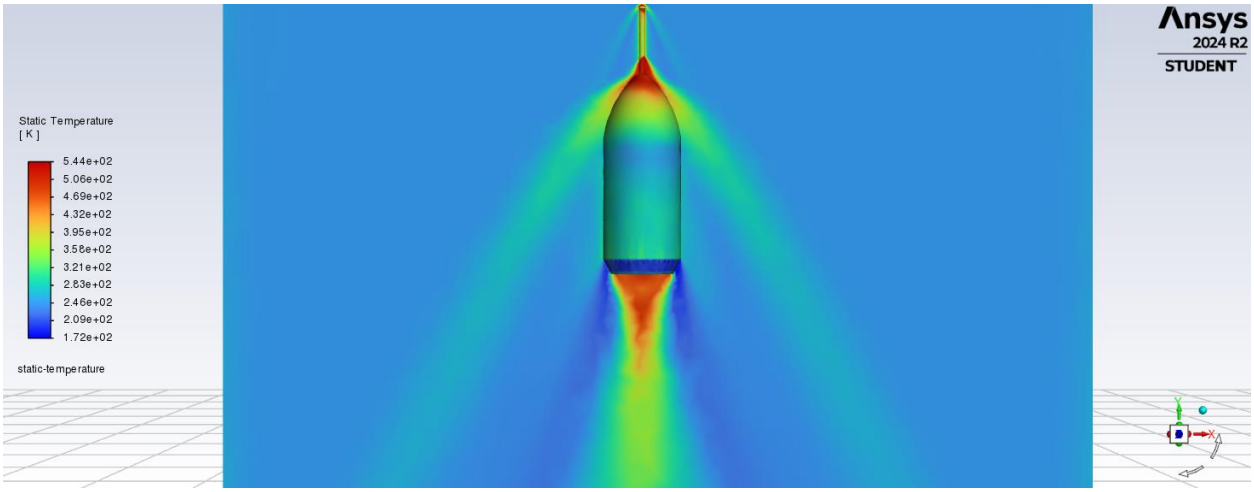

Figure 4.12 NC configuration (2) static temperature contour distribution

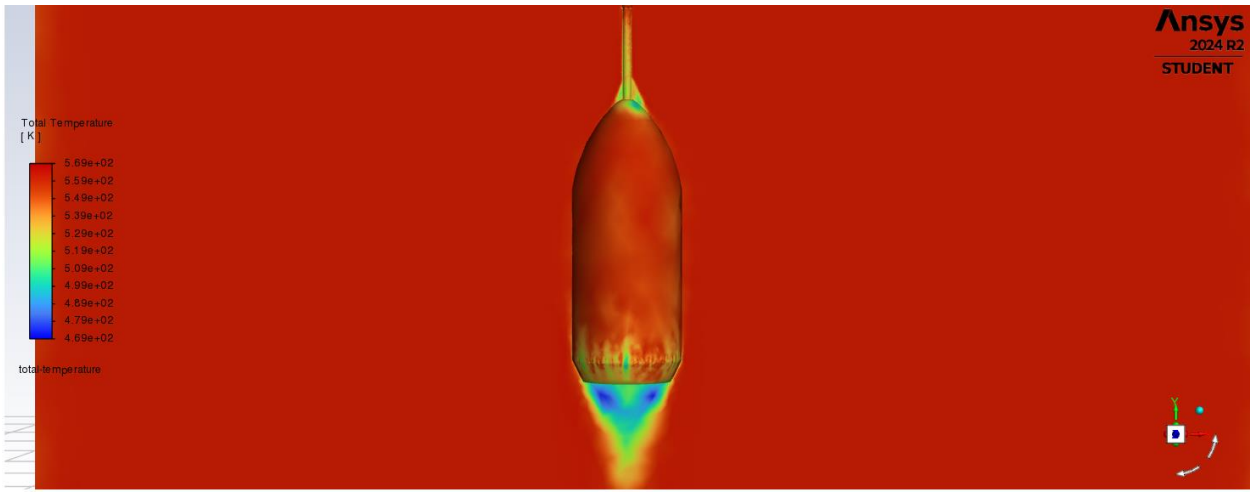

Figure 4.13 NC configuration (2) total temperature contour distribution

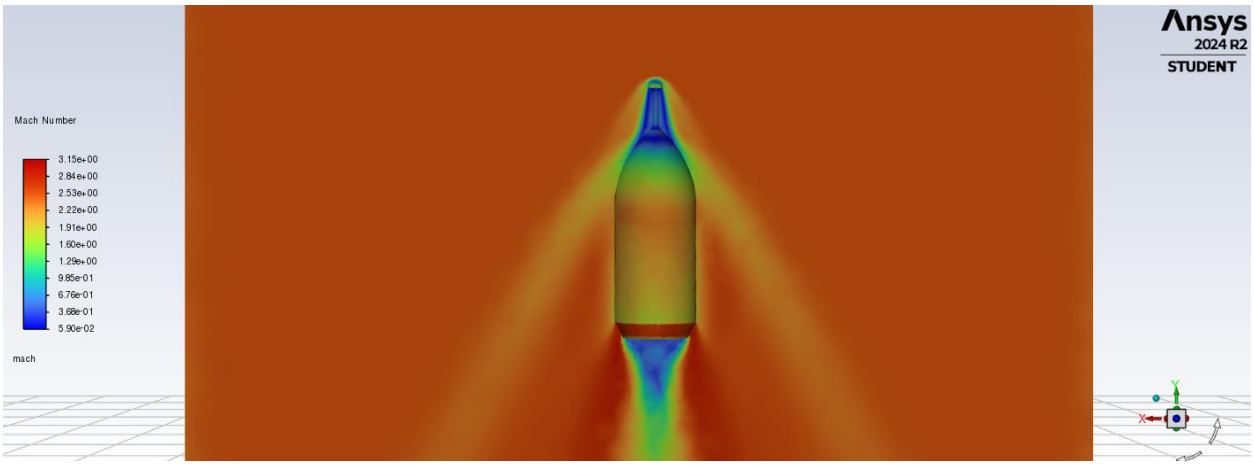

Figure 4.14 NC configuration (3) mach contour distribution

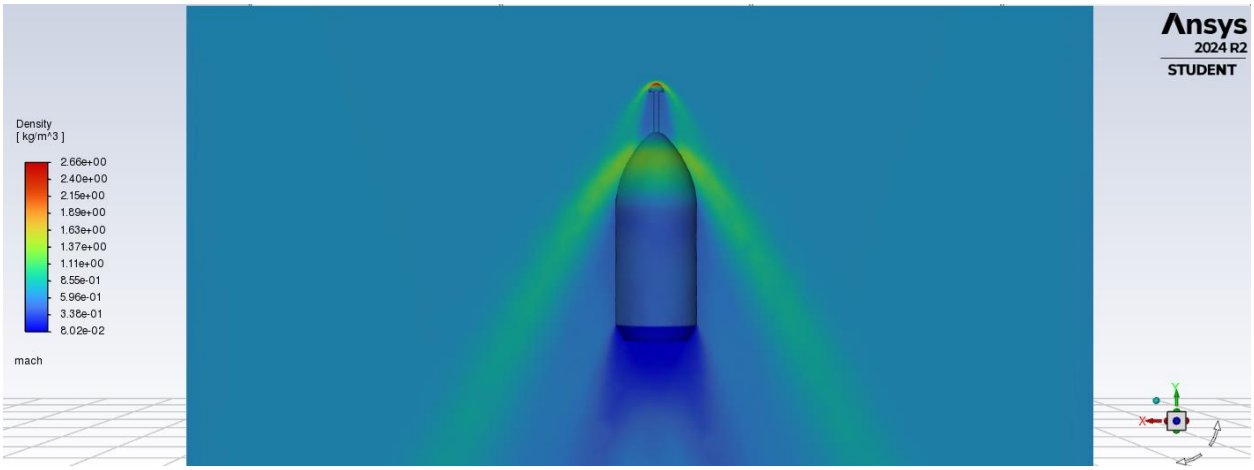

Figure 4.15 NC configuration (3) density contour distribution

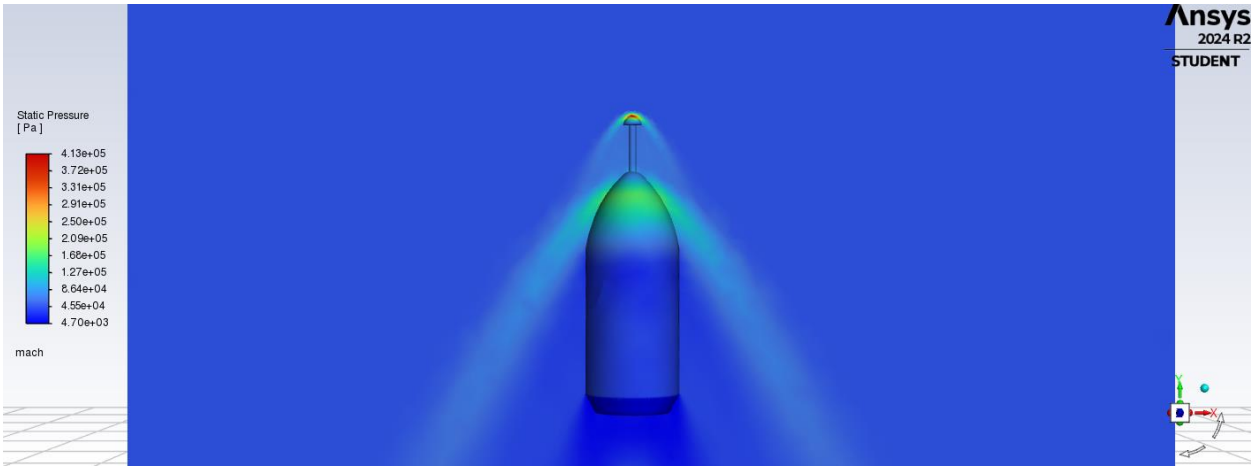

Figure 4.16 NC configuration (3) static pressure contour distribution

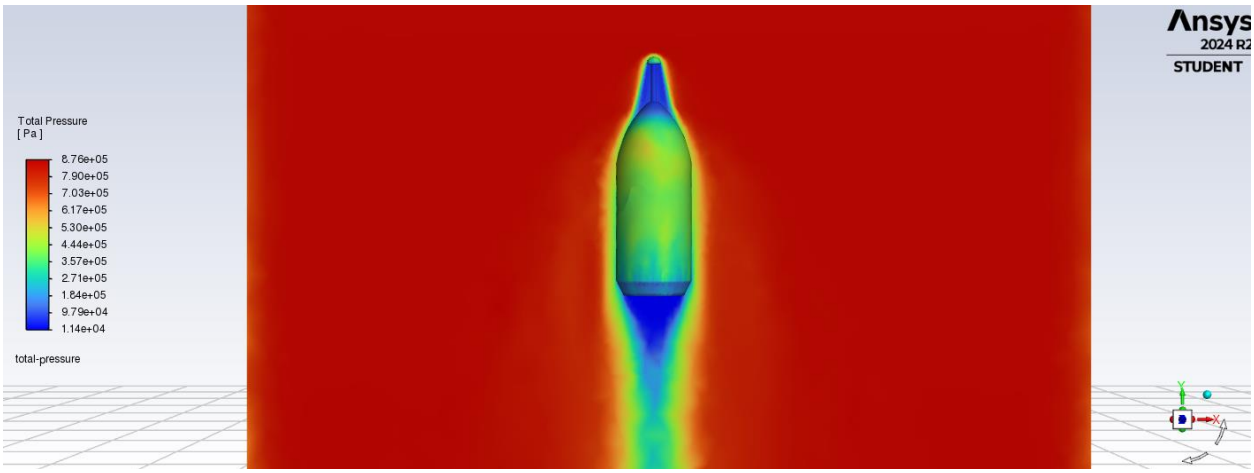

Figure 4.17 NC configuration (3) total pressure contour distribution

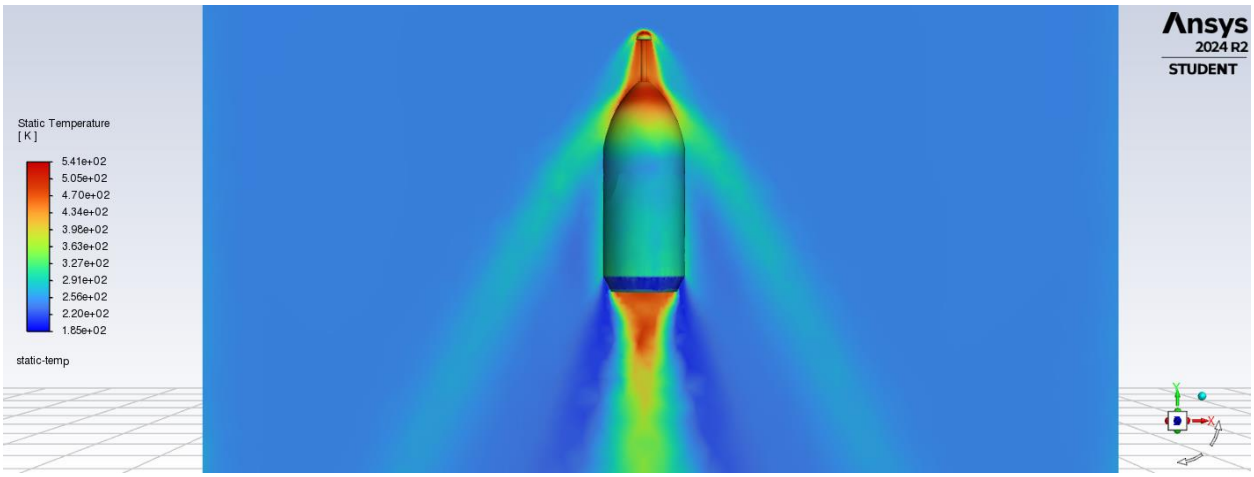

Figure 4.18 NC configuration (3) static temperature contour distribution

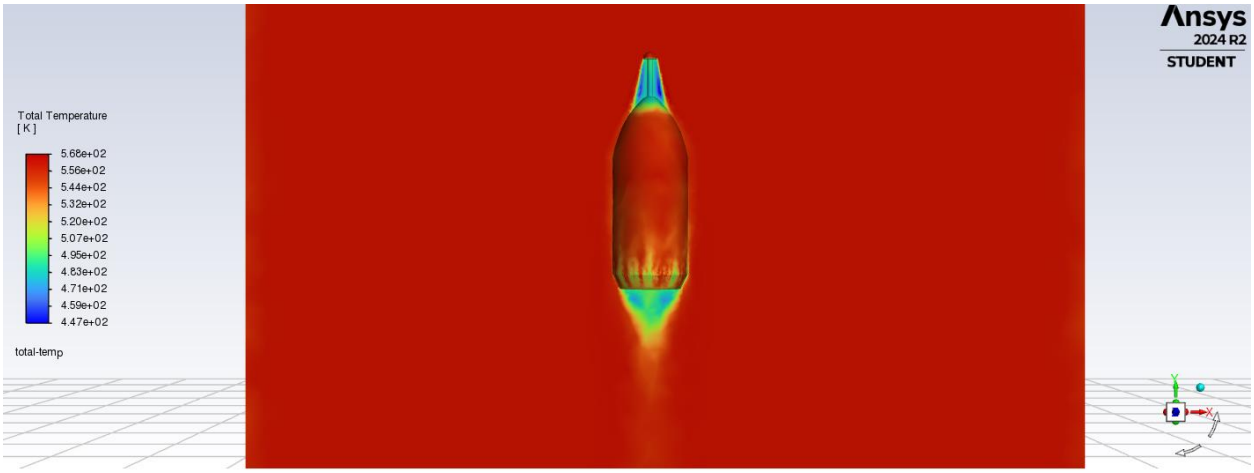

Figure 4.19 NC configuration (3) total temperature contour distribution

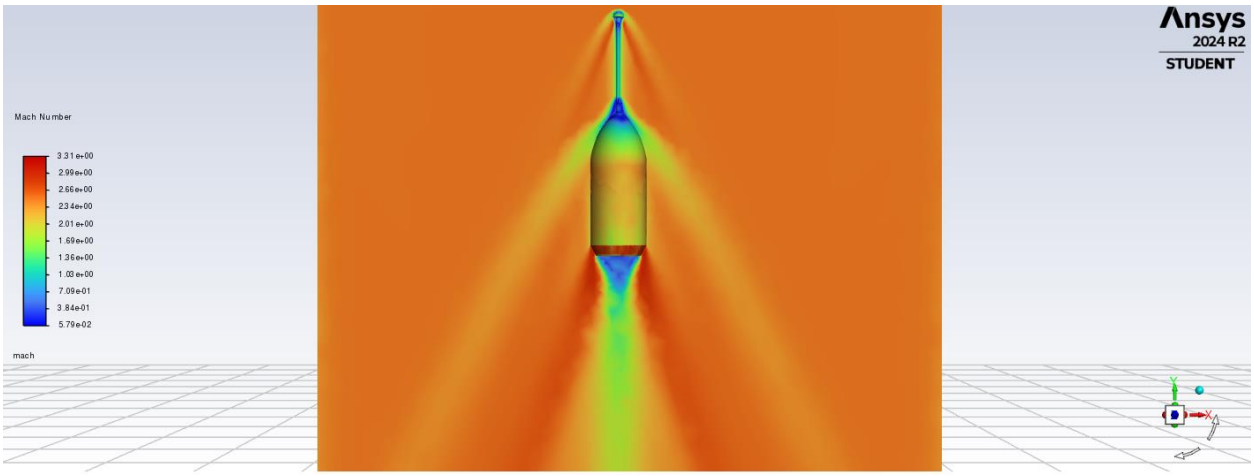

Figure 4.20 NC configuration (4) mach contour distribution

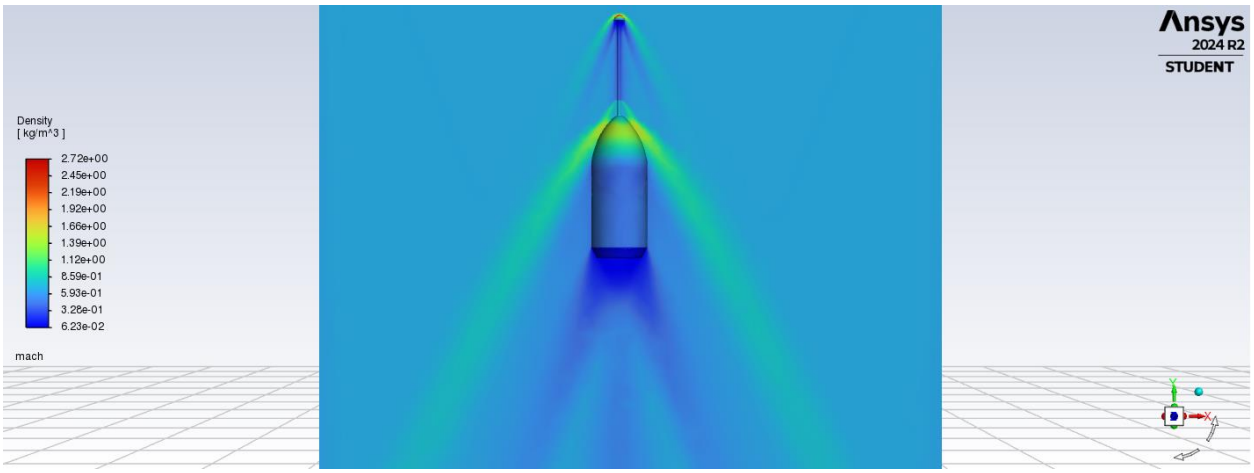

Figure 4.21 NC configuration (4) density contour distribution

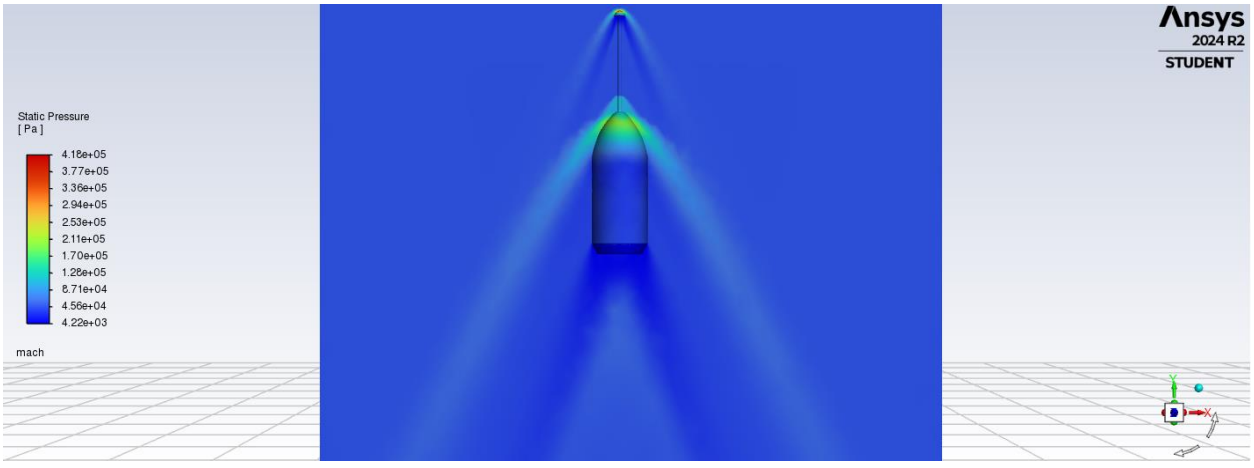

Figure 4.22 NC configuration (4) static pressure contour distribution

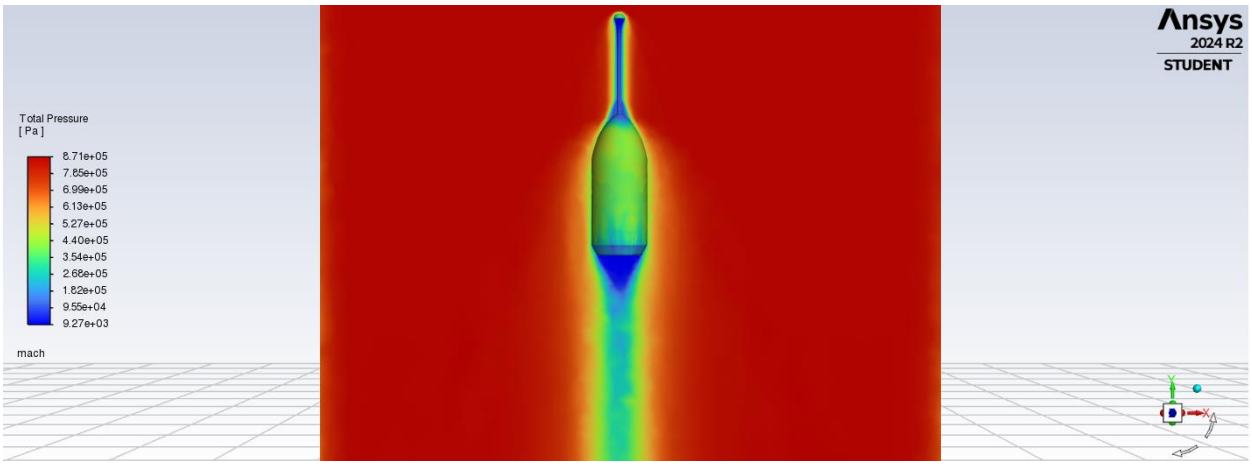

Figure 4.23 NC configuration (4) total pressure contour distribution

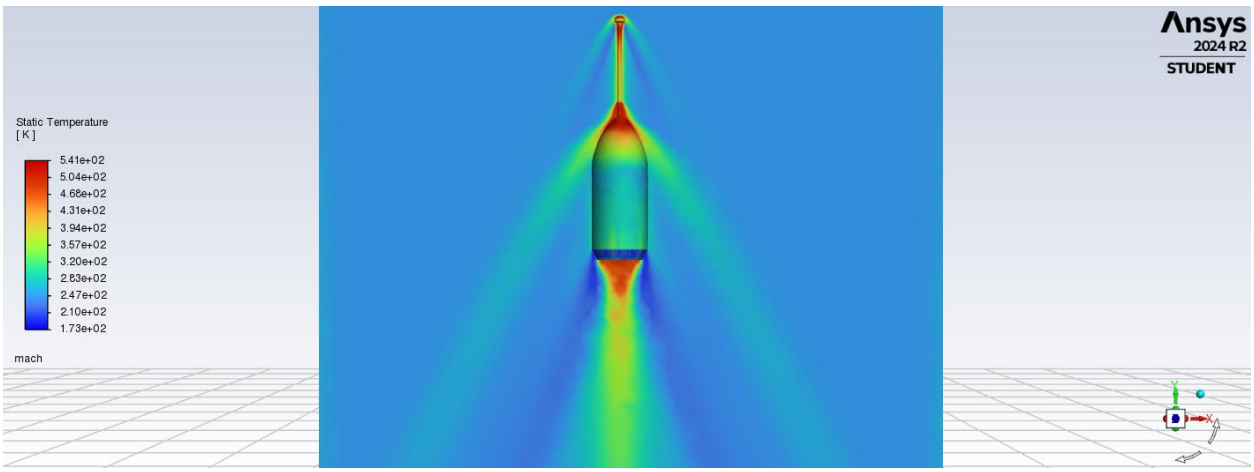

Figure 4.24 NC configuration (4) static temperature contour distribution

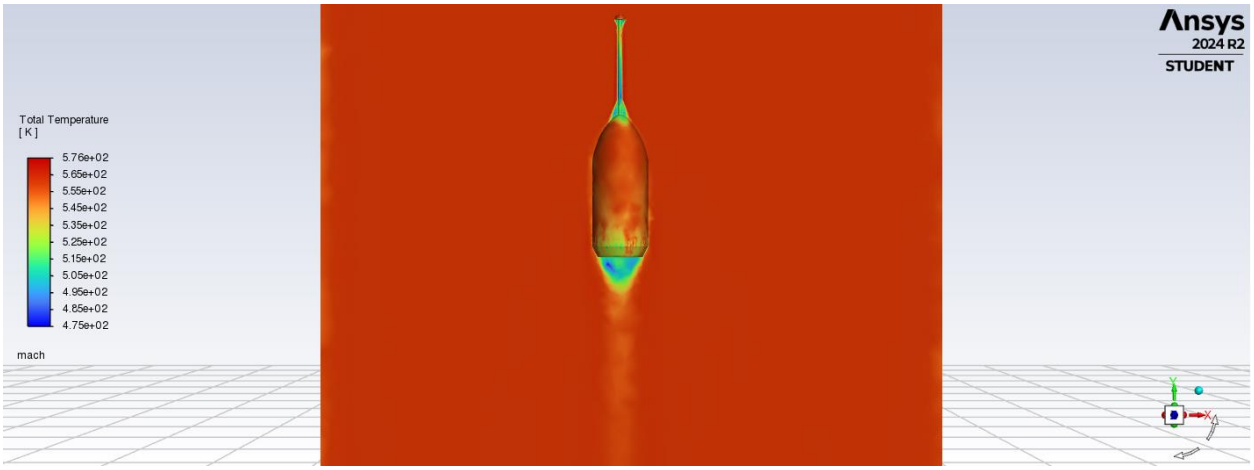

Figure 4.25 NC configuration (4) total temperature contour distribution

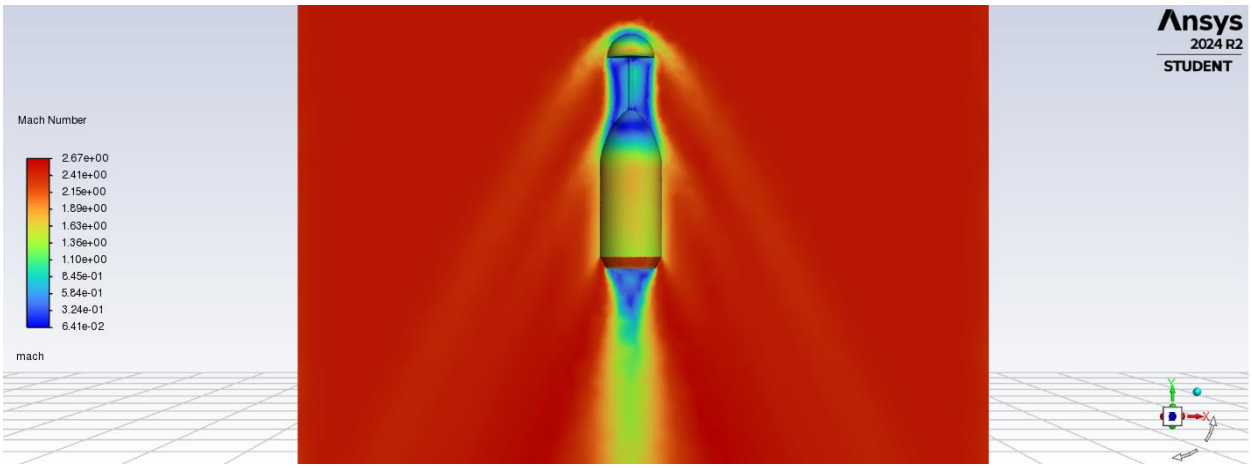

Figure 4.26 NC configuration (5) mach contour distribution

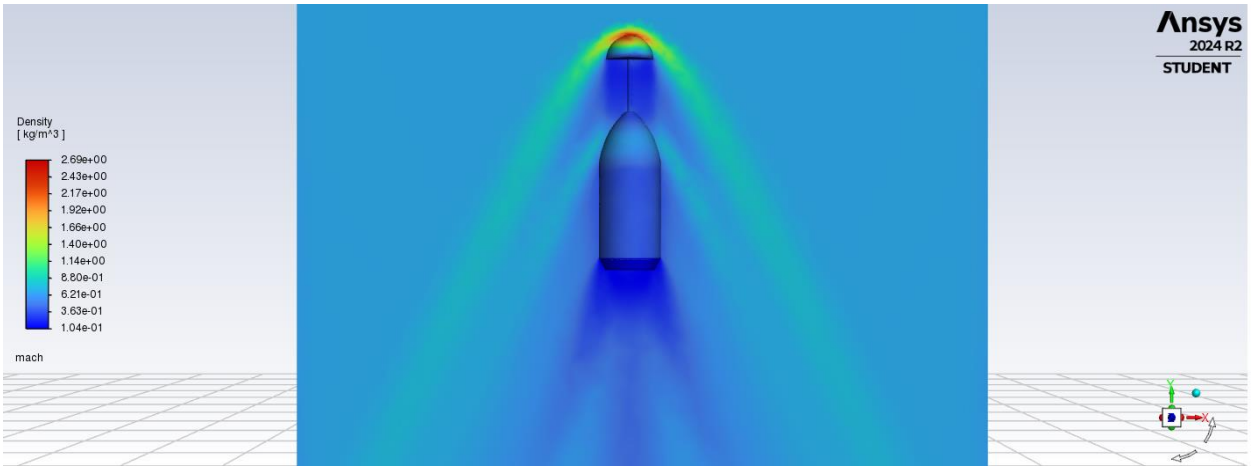

Figure 4.27 NC configuration (5) density contour distribution

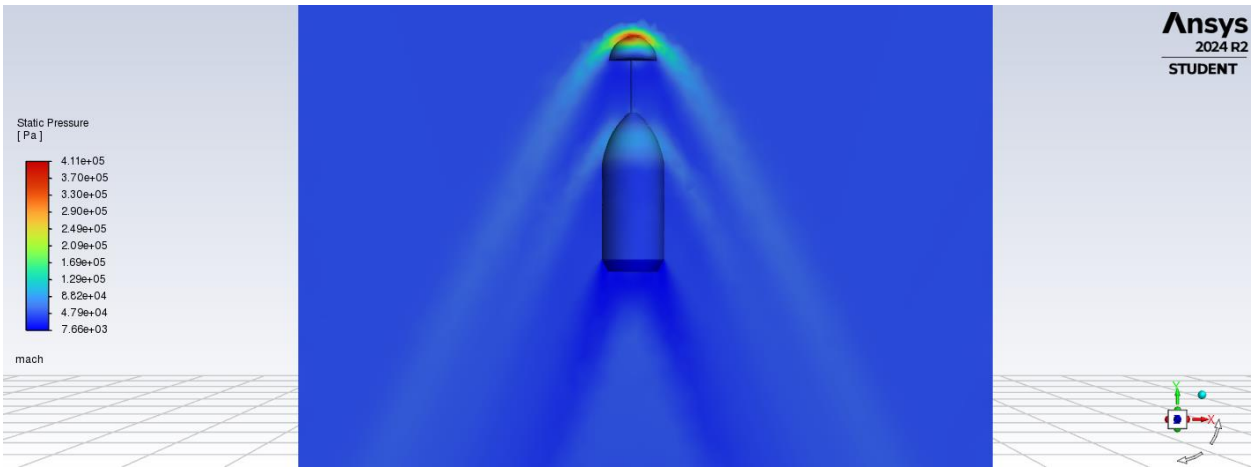

Figure 4.28 NC configuration (5) static pressure contour distribution

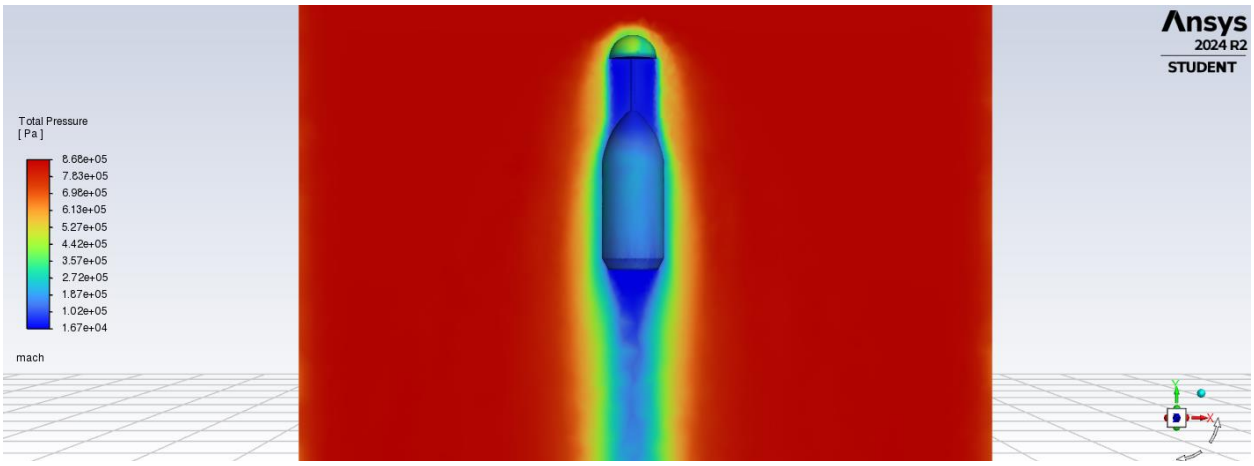

Figure 4.29 NC configuration (5) total pressure contour distribution

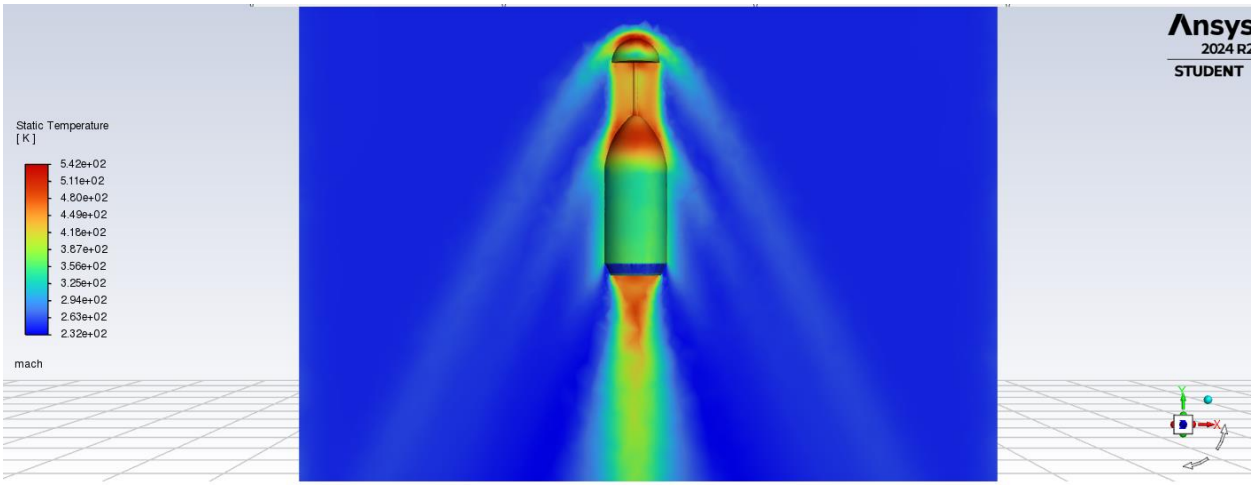

Figure 4.30 NC configuration (5) static temperature contour distribution

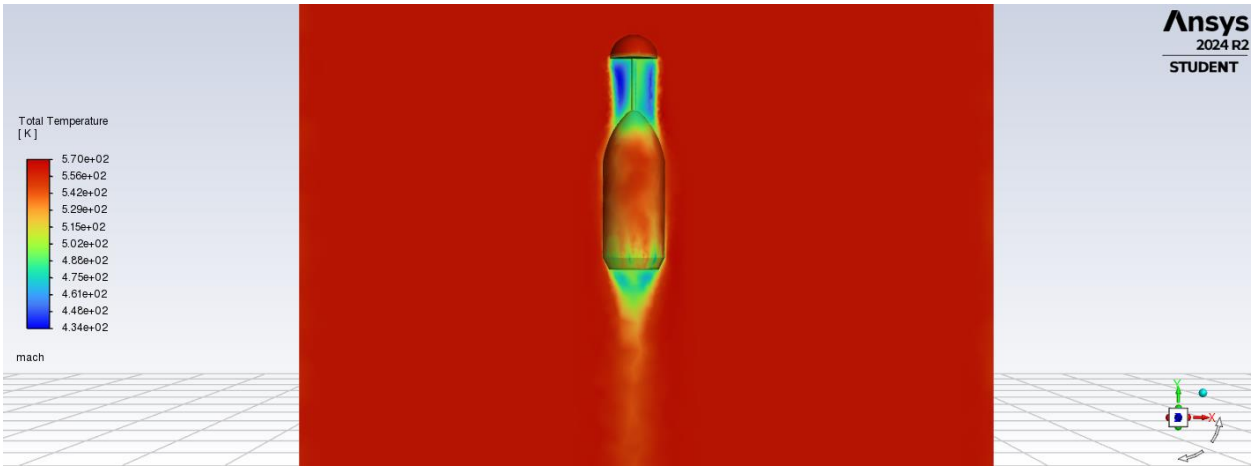

Figure 4.31 NC configuration (5) total temperature contour distribution

4.4 Discussion and Comparison

4.4.1 Mach Contour Analysis

To determine which aerodisk configuration is most effective in minimizing drag, we can begin by analyzing the mach contour distribution figures, since they can reveal how shock waves form and interact with the aerodisk. In an optimal design, the aerodisk should help manage the detached bow shock, reducing its strength and shifting it further downstream. If a configuration exhibits a highly compressed shock wave near the nose cone, this suggests increased drag due to strong pressure buildup. A favorable configuration should show a weaker, more diffused bow shock, indicating a more streamlined airflow and lower drag forces.Based on figure 4.8, configuration (2) illustrates an initial minimal shock wave at the aerodisk, however, further downstream a major shock wave is formed by the nose cone. Configuration (5) illustrates a different shock wave pattern than that of configuration (2). Looking at figure 4.25, for configuration (5), the aerodisk helped reduce the downstream shock significantly. The mach distribution shown on figure 4.14 for configuration (3) performs similarly to configuration (2), it does not reduce the bow shock downstream the NC. Lastly, configuration (4) shows the smallest visible bow shock experienced by the NC, illustrated on figure 4.20. Comparing all these results to the base configuration (1), configuration (4)'s mach distribution is so far the most promising at minimizing drag, based on mach distribution figures alone thus far.

4.4.2 Density Contour Analysis

Density contours provide insight into the expansion and compression of airflow around the nose cone. A smoother density gradient and reduced density buildup behind the aerodisk indicate a more effective design in minimizing flow separation and reducing drag. Configurations with abrupt changes in density typically experience higher aerodynamic resistance, suggesting inefficient shock wave management. Based on the density distribution figures, figures 4.9 and 4.27 illustrate a poor density gradient transition, meaning configurations (2) and (5) respectively are not effective at minimizing drag thus far. The density distribution figures 4.15 and 4.21 for configuration (3) and configuration (4) show a smoother density gradient, more so for configuration (3). This is due to the distance between the aerodisk and the tip of the NC, by observing table 4.1, we can observe that configuration (3) has a shorter length for the aerodisk than that of configuration (4) by approximately factor of 3. This implies that the closer the aerodisk to the tip of the rocket NC, the smoother the density gradient will be, thus less air buildup is likely to occur behind the aerodisk.

4.4.3 Static Pressure Contour Analysis

Static pressure distributions help assess the pressure buildup at the stagnation point and along the surface of the nose cone. A configuration with lower pressure differentials between the stagnation region and the surrounding flow will generally experience less pressure drag. A more effective aerodisk should distribute pressure more uniformly, preventing excessive buildup at the front and reducing adverse pressure gradients that contribute to drag. Looking at the static pressure distribution figures 4.4, 4.10 and 4.24, configuration (2) and configuration (5) depict a greater pressure build up for both the aerodisk and the tip of the NC when compared to configuration (1). Configuration (3) performs slightly better than configuration (1) in terms of minimizing pressure build up at the tip of the aerodisk, based on their static pressure figures 4.4 and 4.16. However, configuration (4) shows lower pressure differentials when compared to the rest of the

configurations, suggesting that configuration (4) is thus far the most optimal aerodisk configuration to minimize drag.

4.4.4 Static Temperature Contour Analysis

Temperature variations correlate with shock strength and flow energy dissipation. A well-optimized aerodisk should mitigate excessive heating caused by intense shock waves and stagnation effects. If a configuration exhibits localized high-temperature regions, it suggests stronger shocks and greater thermal loads, which could indicate higher drag. The most optimal aerodisk design will result in a more uniform temperature distribution, signifying smoother airflow and reduced shock interactions. The static temperature distribution figures that depict poor temperature transitions are figures 4.12 and 4.30 for configurations (2) and (3) respectively. Based on figure 4.24, Configuration (4) static temperature distribution depicts a strong thermal load at the tip of the aerodisk and the tip of the NC, indicating that this configuration will face thermal challenges at higher mach values. Figures 4.6 and 4.18 show minimal temperature variation compared to the rest of the configurations, meaning that configuration (1) and (3) perform exceptionally well when it comes to handling thermal loads. This is most likely due to configuration (4) having a longer length for the aerodisk when compared to configuration (1) and (3), implying that a longer length will result in greater thermal loads.

4.4.5 Identifying the Most Optimal Configuration

By comparing the results across all five configurations, the most effective aerodisk design is configuration (4), as it exhibits the most favorable aerodynamic characteristics. Configuration (4) demonstrated the weakest and most streamlined bow shock in the Mach contour analysis, indicating reduced drag forces. Additionally, its density gradient transition was smoother than most other configurations, suggesting improved airflow management and minimized flow separation. In terms of static pressure distribution, configuration (4) had the lowest pressure buildup at both the aerodisk and the nose cone tip, further supporting its effectiveness in reducing drag. However, while configuration (4) was optimal in terms of aerodynamic performance, it exhibited a significant thermal load at the tip of the aerodisk and the nose cone, which may present challenges at higher Mach numbers. Despite this, based on drag reduction alone, configuration (4) is identified as the most effective aerodisk configuration for minimizing aerodynamic resistance.

4.5 Conclusion

The results of this chapter highlight the impact of aerodisk design on aerodynamic performance, particularly in terms of minimizing drag. Through the analysis of Mach distribution, density gradients, static pressure, and thermal variations, configuration (4) was determined as the most effective aerodisk configuration in reducing drag forces. While thermal management remains a concern for this design, its ability to streamline shock waves and maintain a low-pressure differential makes it a promising candidate for supersonic applications.

The next chapter will build upon these findings by shifting focus to nozzle design optimization. Similar to the approach taken in Chapters 3 and 4, nozzle configurations will be examined through CFD simulations to determine the most efficient design for thrust optimization and reduced flow separation.

Chapter 5. Rocket Nozzle Design and Performance Evaluation

5.1 Introduction

Building upon the aerodynamic optimization of the rocket nose cone in Chapters 3 and 4, this chapter focuses on the analysis and optimization of rocket nozzle designs. The nozzle plays a crucial role in converting thermal energy from combustion into kinetic energy, thereby generating thrust. It also impacts the overall aerodynamic drag of the rocket body, especially at transonic and supersonic speeds.

The primary objective of this chapter is to investigate four different nozzle configurations using Computational Fluid Dynamics (CFD) simulations to identify the design that most effectively minimizes drag while maximizing flow efficiency. The chosen configurations include a conic nozzle, bell nozzle, double-bell nozzle, and aerospike nozzle. Each nozzle has unique characteristics that affect its aerodynamic performance under different flow conditions. The investigation will involve analyzing the Mach, pressure, velocity, temperature and density distribution across each nozzle. The nozzle that depicts the highest exit velocity while maintaining effective flow expansion will be identified as the most efficient design. Following this, the optimal nozzle will be further refined through parametric variations to maximize performance in the next chapter.

5.2 Nozzle Geometry Selection & Design Rationale

Four distinct nozzle geometries were selected for this study, each representing a widely recognized design used in modern rocket propulsion systems:

1. Conic Nozzle:
    - A simple and efficient design with a linear expansion.
    - Often used in early rocket designs due to its ease of manufacturing.
    - Provides adequate performance for short-duration missions.
2. Bell Nozzle:
    - Features a parabolic contour for improved expansion efficiency.
    - Reduces the formation of shocks within the nozzle.
    - Frequently used in launch vehicles like the Falcon 9.
3. Double-Bell Nozzle:
    - Incorporates a dual-expansion profile to optimize performance at different altitudes.
    - Offers improved efficiency across a broader range of atmospheric conditions.
4. Aerospike Nozzle:
    - Maintains performance across a wide range of altitudes by using external atmospheric pressure for flow shaping.
    - Frequently used in experimental or next-generation launch vehicles.

Each nozzle was designed using Autodesk Inventor, incorporating geometric principles and validated references from literature. Key design parameters, such as throat diameter, expansion ratio, and nozzle length, were applied to ensure comparability during the CFD analysis. Visual

representations of these nozzles will be presented in subsequent sections. The rationale behind selecting these geometries stems from their unique aerodynamic behaviors. By comparing their performance using identical boundary conditions, a clear understanding of their respective strengths and weaknesses will be established.

5.3 CAD Modeling & Mesh Setup

The CAD models of the conic, bell, double-bell, and aerospike nozzles were created using Autodesk Inventor. Each design adhered to standard nozzle geometry guidelines, ensuring appropriate expansion ratios and smooth transitions from the combustion chamber to the nozzle exit. Below are some figures of the four nozzle configurations.

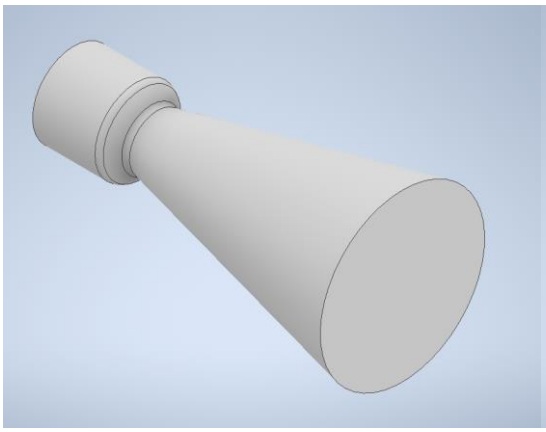

Figure 5.1 Conic CAD

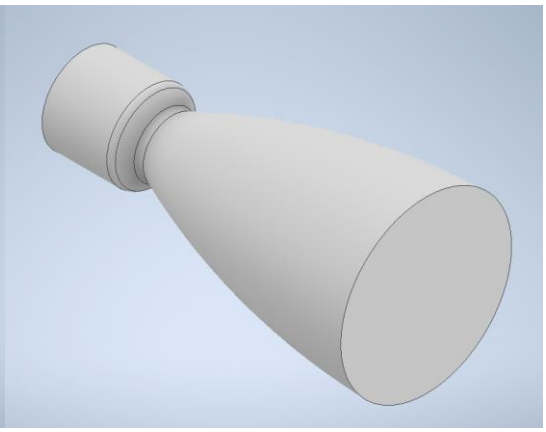

Figure 5.2 Bell CAD

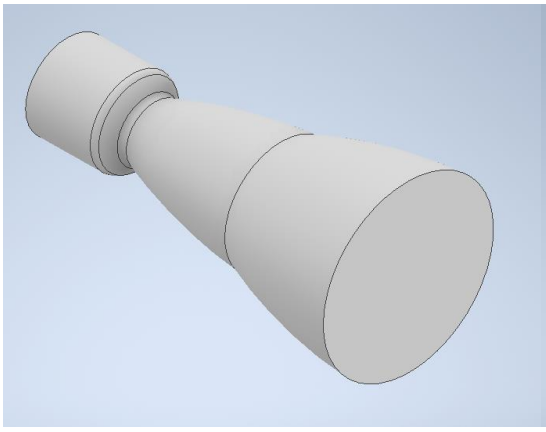

Figure 5.3 Double bell CAD

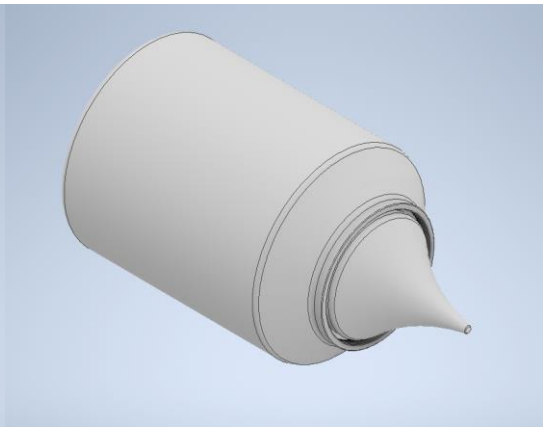

Figure 5.4 Aerospike CAD

All the nozzle designs were similar to design besides the Aerospike Nozzle. Below is a split view of the aerospike nozzle represented by figure 5.5, illustrating the inside of the geometry.

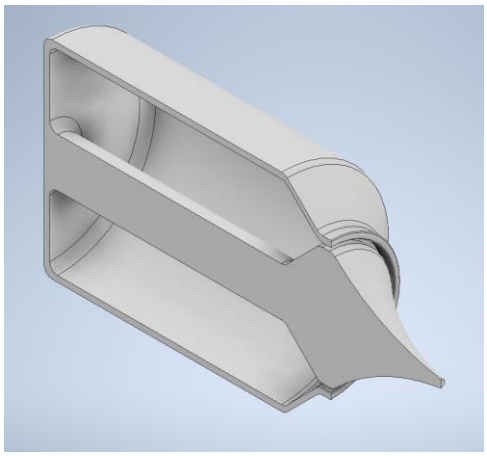

Figure 5.5 Split aerospike nozzle

Once the designs were completed, the models were exported in STEP format for import into ANSYS Fluent. A structured mesh was generated using the ANSYS Meshing tool. Special attention was given to refining the mesh around regions of interest, particularly near the nozzle throat and along the nozzle wall, to accurately capture boundary layer effects and shockwave formation. On figure 5.6, a mesh sizing face control was utilized around the throat section for every nozzle configuration apart from the aerospike nozzle. The mesh sizing value was set for 0.0001 m, with a growth rate of 5% to ensure smooth mesh transitions and avoid unnecessary computational expense. Similarly, the same process was followed for the upstream and downstream section of the nozzles, except with different values as viewed in figures 5.7 and 5.8.

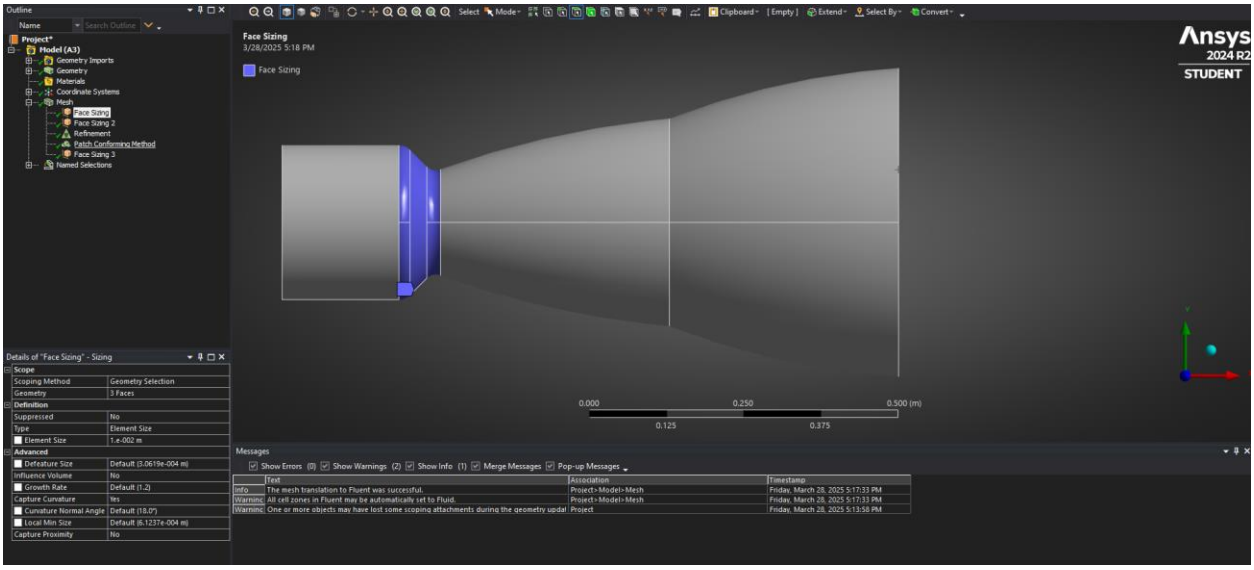

Figure 5.6 Mesh face sizing for throat section example

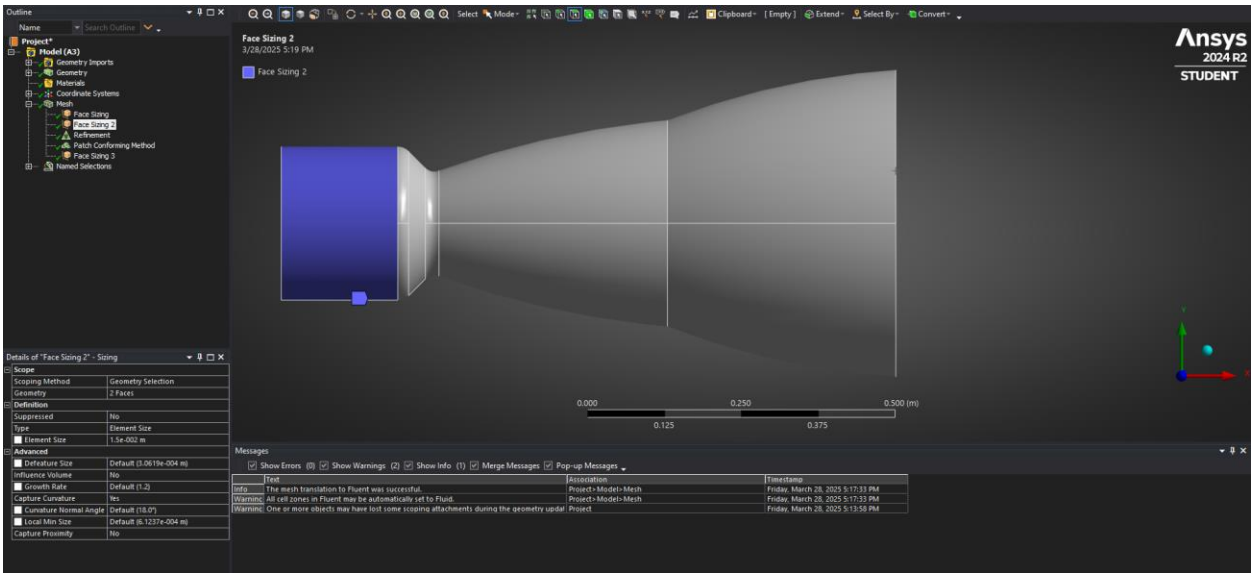

Figure 5.7 Mesh face sizing for upstream section example

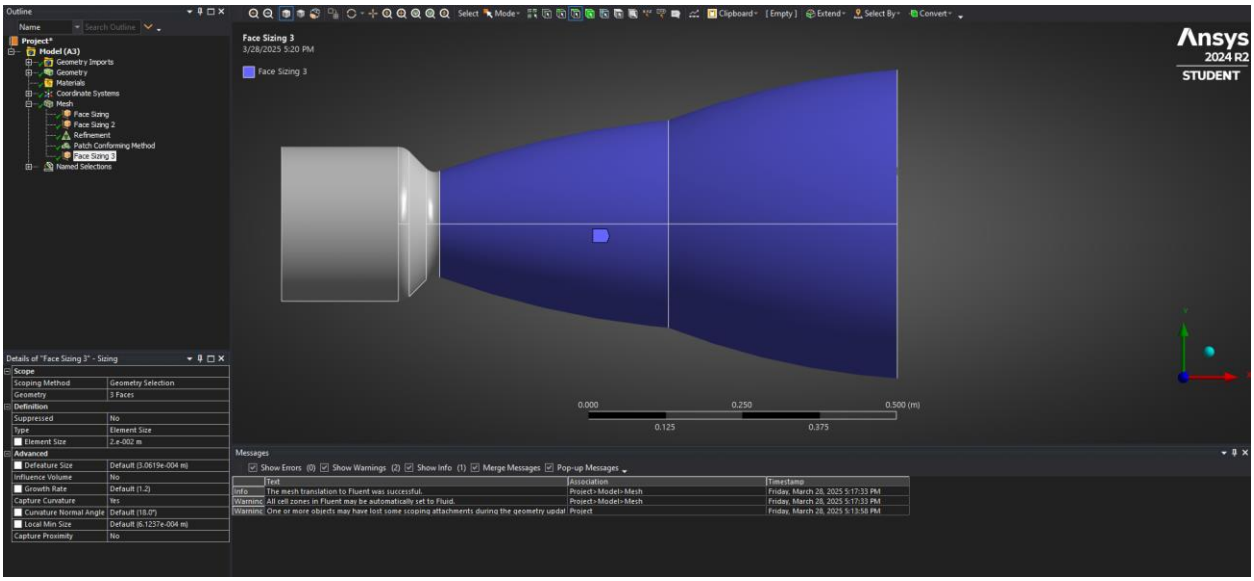

Figure 5.8 Mesh face sizing for downstream section example

Furthermore, mesh refinement was necessary to ensure accurate resolution of flow features, especially in regions where rapid changes in pressure, velocity, and density were expected. This included areas where shockwaves formed and in the boundary layer along the nozzle walls. Refining the mesh in these regions minimizes numerical errors and improves the accuracy of the simulation results. For this purpose, localized face sizing and body refinement techniques were applied using ANSYS Meshing. The goal was to achieve a higher mesh density near the nozzle throat and expansion regions, where flow gradients are most pronounced. Mesh independence studies were conducted to ensure that further refinements did not lead to significant changes in the results, confirming the adequacy of the selected mesh resolution.

Additionally, for this analysis, tetrahedral elements were chosen as the primary mesh type due to their versatility in capturing complex geometric features and flow structures. Unlike structured hexahedral meshes, which are often preferable for simpler geometries, tetrahedral meshes offer greater flexibility when modeling the curved contours and intricate shapes of the nozzle configurations. This selection also enabled the implementation of adaptive mesh refinement in key regions, improving the resolution of essential flow characteristics. While tetrahedral elements may result in slightly higher computational costs compared to structured meshes, their ability to provide accurate results for the complex flow fields encountered in nozzle simulations justified their use in this study.

After conducting mesh refinements, sizing, and improving the overall quality of the mesh, a viable tetrahedral mesh of the geometry was achieved and ready for simulation. Tetrahedral elements were selected due to their flexibility in handling complex geometries such as the curved ramp and chamber transitions of the nozzle. This type of mesh conforms more easily to complex surface geometries, whereas structured hexahedral meshes would require extensive manual blocking to achieve similar accuracy. Additionally, tetrahedral meshes enabled local refinement in regions of expected flow gradients, such as near the throat and spike tip, improving resolution without significantly increasing overall cell count. Figure 5.9 illustrates the final mesh used for the simulation, showcasing its density distribution and surface conformity.

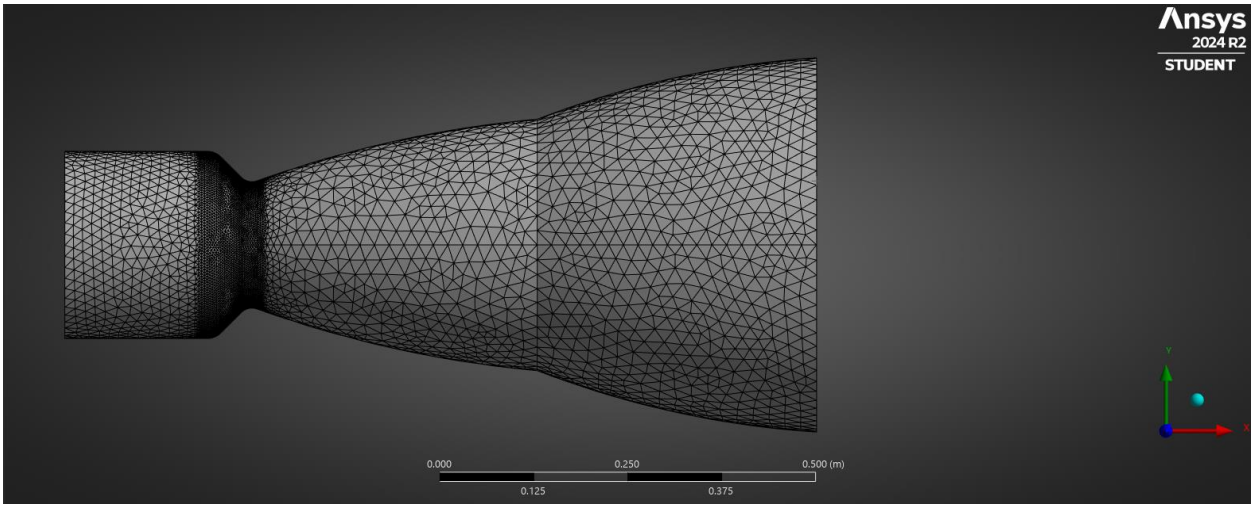

Figure 5.9 Double bell nozzle final mesh

Despite multiple attempts, the mesh for the aerospike nozzle could not be successfully generated due to persistent error messages. This issue was likely caused by the complex geometry of the aerospike nozzle, which introduces sharp edges and intricate flow paths that pose challenges for mesh generation. The presence of small, tightly curved surfaces near the spike can lead to poor element quality and convergence difficulties during the meshing process. This issue was attempted to be solved by curving the end of the nozzle spike, however it proved to be futile, the mesh could still not be generated. Additionally, the requirement for a refined mesh to capture the detailed flow features around the spike increased the level of complexity of the issue, by augmenting an increase in computational needs and leading to element skewness or negative volume errors. As a result, simulation results were only obtained for the conic, bell, and double-bell nozzles. Future work

could involve exploring alternative meshing techniques or simplifying the situation by conducting a 2D CFD simulation of an aerospike nozzle geometry opposed to doing one in 3D as intended.

The next section will cover the governing equations and physics applied during the CFD analysis, establishing the framework for evaluating the performance of each nozzle configuration.

5.4 Physics and Continua

5.4.1 Governing Equations and Physics

The CFD analysis conducted in this study is governed by the fundamental principles of fluid mechanics, represented by the compressible form of the Navier-Stokes equations. These equations describe the conservation of mass, momentum, and energy within the flow field, and are used to predict the aerodynamic performance of the nozzle configurations. The equations mentioned can be found in chapter 3 in section 3.4, where a very similar approach was used in that chapter to simulate flow for a rocket nose cone, the only difference now is that the simulation will be done on a rocket nozzle. The equations in section 3.4, paired with appropriate turbulence modeling and boundary conditions, form the basis for the simulation for this chapter. The k-omega SST turbulence model was selected due to its accuracy in predicting boundary layer separation and shockwave interactions, both of which are critical for nozzle performance evaluation.

5.4.2 Boundary conditions

The following boundary conditions were applied in the CFD simulations to ensure accurate representation of the aerodynamic environment within the rocket nozzles.

At the inlet, a pressure inlet condition was specified, representing the combustion chamber pressure. The total pressure and total temperature values were set to approximately 7MPa and 3500K, respectively, simulating the high-energy exhaust gases. These values are typical of combustion conditions in rocket engines.

At the outlet, a pressure outlet condition was applied, with the ambient pressure set to 101325 Pa to represent sea-level conditions. This allows the exhaust gases to expand through the nozzle and reach the desired exit velocity.

The nozzle walls were defined as no-slip, adiabatic walls to account for viscous effects and thermal insulation, preventing heat transfer through the nozzle material. Additionally, appropriate wall boundary conditions ensured accurate modeling of shear forces and flow separation.

For numerical stability, initial conditions were estimated based on the expected pressure and temperature gradients within the nozzle. The domain was initialized with a pressure and temperature distribution using ANSYS Fluent standard initialization method.

These boundary conditions were consistently applied across all three nozzle configurations to ensure a fair comparison of aerodynamic performance.

5.4.3 Assumptions

The following assumptions were made to simplify the simulations and ensure computational efficiency while maintaining accuracy. The fluid was treated as compressible, as rocket nozzle flows inherently involve high-speed, supersonic, and sometimes transonic conditions. Air was modeled as an ideal gas with temperature-dependent properties to account for variations in density, pressure, and temperature. A pressure-based solver was used to handle the compressible nature of the flow, ensuring a smooth convergence for all nozzle configurations. Additionally, gravity effects were neglected, as their influence on the high-speed, short-duration nozzle flow is negligible.

The simulations were conducted using a steady-state flow analysis to reduce computational time while capturing the primary aerodynamic characteristics of the nozzle configurations. Although transient effects such as shockwave oscillations and turbulent fluctuations may occur, the steady-state approach was deemed sufficient for assessing comparative performance. Additionally, all nozzle walls were assumed to be adiabatic with no heat transfer through the surface, representing insulated nozzle walls. This assumption simplifies the thermal analysis and focuses the study on aerodynamic effects. Combustion reactions within the nozzle were not modeled, and the flow was considered a single-phase gas.

These assumptions, while limiting certain physical effects, provided a practical and efficient framework for evaluating the aerodynamic behavior of the nozzle configurations in a consistent and reliable manner.

5.5 Simulation Results and Discussion

The following figures are simulation results for conic, bell, and double bell nozzle configurations for the following distribution contours:

- Mach
- Velocity
- Static Temperature
- Static Pressure
- Density

5.5.1 Conic Nozzle Contour Distribution Planes

Figures 5.10 to 5.14 illustrate the contour distribution planes for the conic nozzle configuration. On figure 5.10 and 5.11, the mach and velocity distributions depict how the flow converges to the throat to about mach ~1 and then rapidly expands downstream reaching a maximum escape velocity of ~2000 m/s (mach ~2.8). The next figures, 5.12 and 5.13, illustrate the static temperature and pressure distribution across the nozzle, both display similar behavior for the flow. The flow first begins with higher temperature and pressure, but as the flow passes through the converging area, it speeds up and drops in both temperature and pressure, an effect of energy conservation.

Lastly, as shown in Figure 5.14, the density distribution highlights the effects of compressibility. As the flow passes through the nozzle throat, it accelerates to supersonic speeds, resulting in a significant decrease in density. This reduction occurs due to the rapid conversion of thermal energy into kinetic energy, in accordance with the principles of mass and momentum conservation. As the velocity increases, the pressure and temperature decrease, leading to a corresponding drop in density.

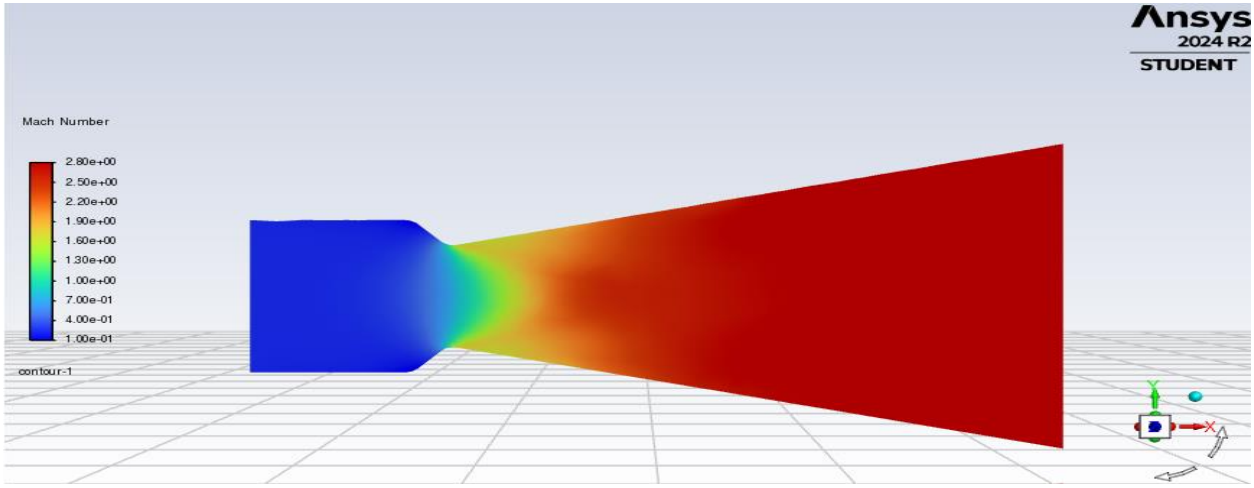

Figure 5.10 Mach distribution for conic nozzle

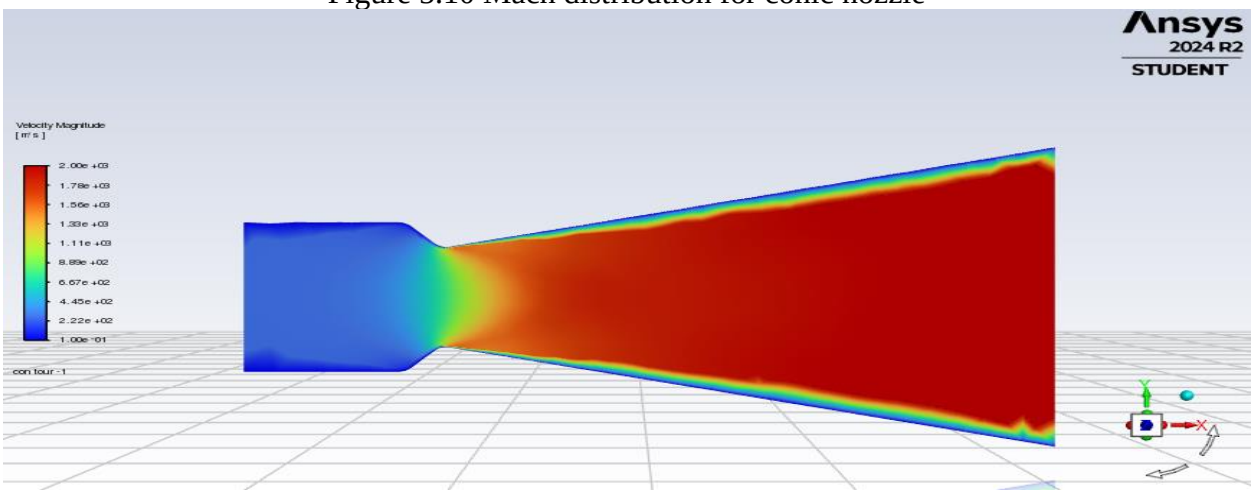

Figure 5.11 Velocity distribution for conic nozzle

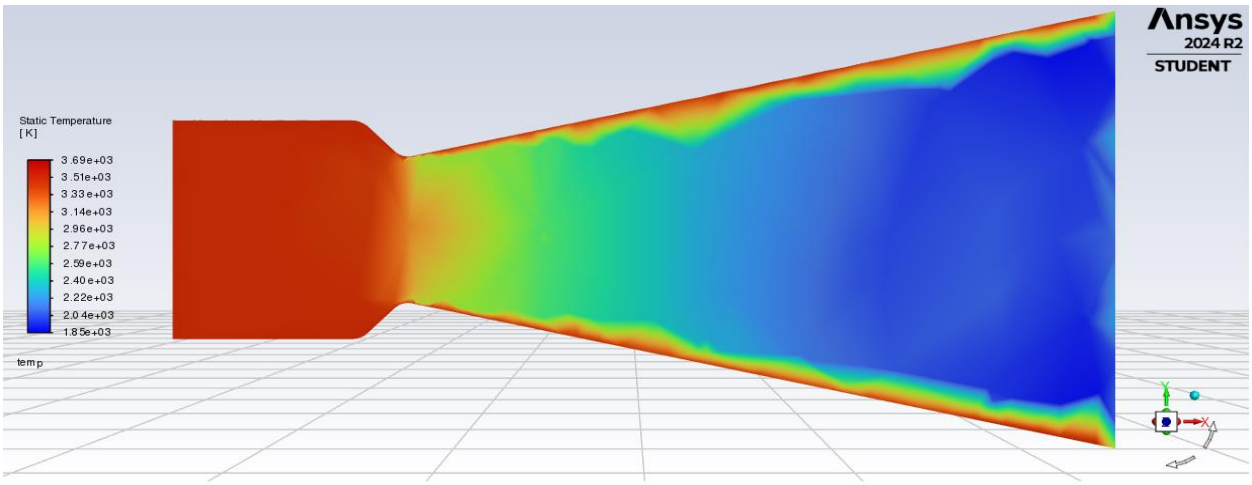

Figure 5.12 Static Temperature distribution for conic nozzle

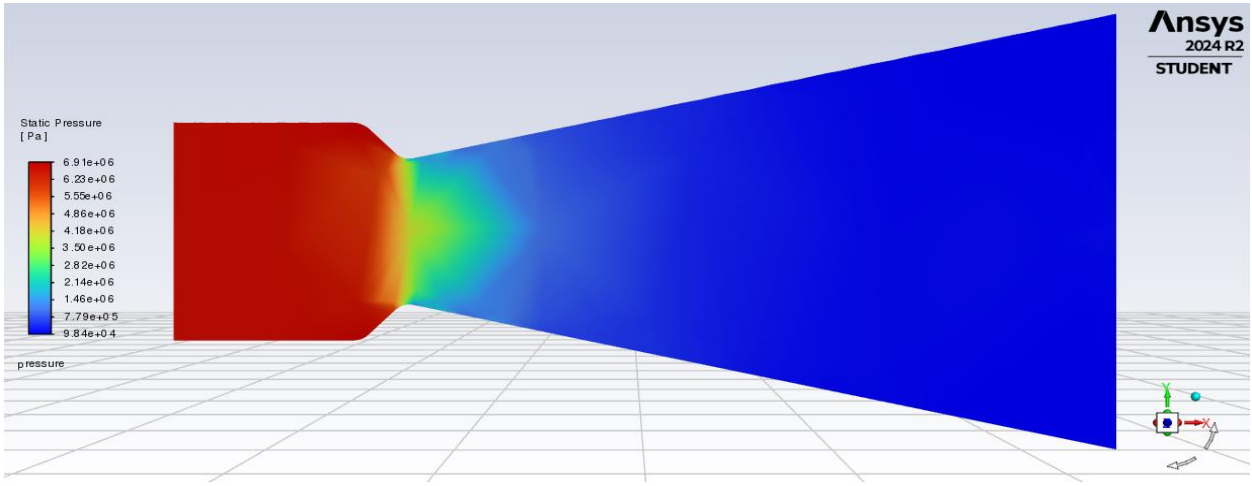

Figure 5.13 Static Pressure distribution for conic nozzle

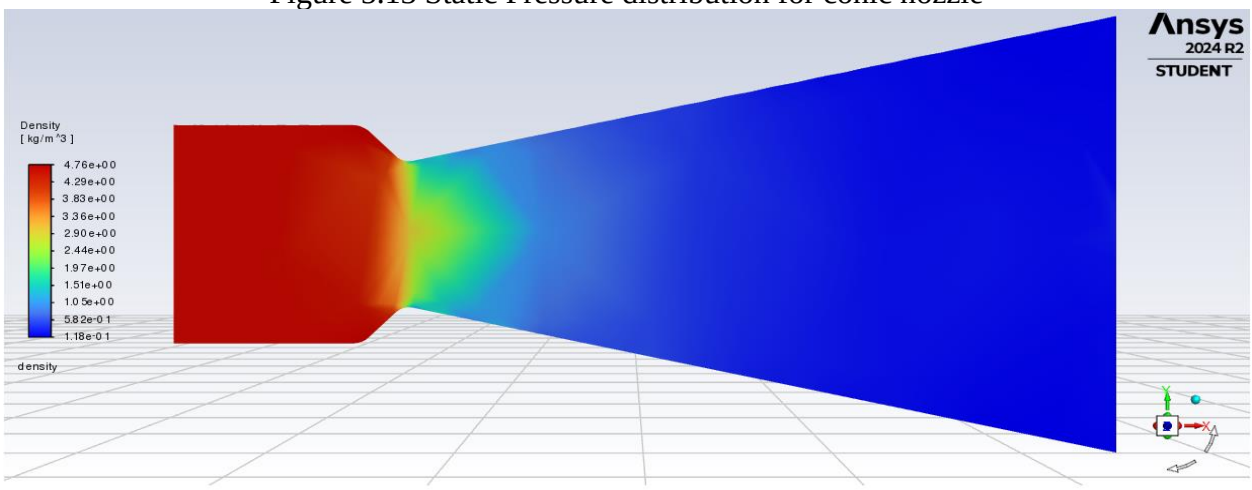

Figure 5.14 Density distribution for conic nozzle

5.5.2 Bell Nozzle Contour Distribution Planes

Figures 5.15 to 5.19 illustrate the contour distribution planes for the bell nozzle configuration. On figure 5.15 and 5.16, the Mach and velocity distributions depict how the flow passes through the nozzle throat, reaching Mach ~1 before expanding downstream to a maximum escape velocity of approximately ~2110 m/s (Mach 2.92). The parabolic contour of the bell nozzle enables a smoother and more efficient flow expansion compared to the conic nozzle.

Next, figures 5.17 and 5.18 show the static temperature and pressure distributions. Similar to the conic nozzle, the flow begins with high temperature and pressure, which decrease significantly as the flow accelerates through the throat and expands within the nozzle. However, the bell nozzle demonstrates more gradual pressure and temperature drops, indicating efficient energy conversion. Lastly, as presented in Figure 5.19, the density distribution highlights the effects of compressibility. As the flow accelerates, its density decreases due to the conversion of thermal energy into kinetic energy. The density drop remains more uniform across the nozzle's contour, reducing the likelihood of flow separation and ensuring greater thrust efficiency.

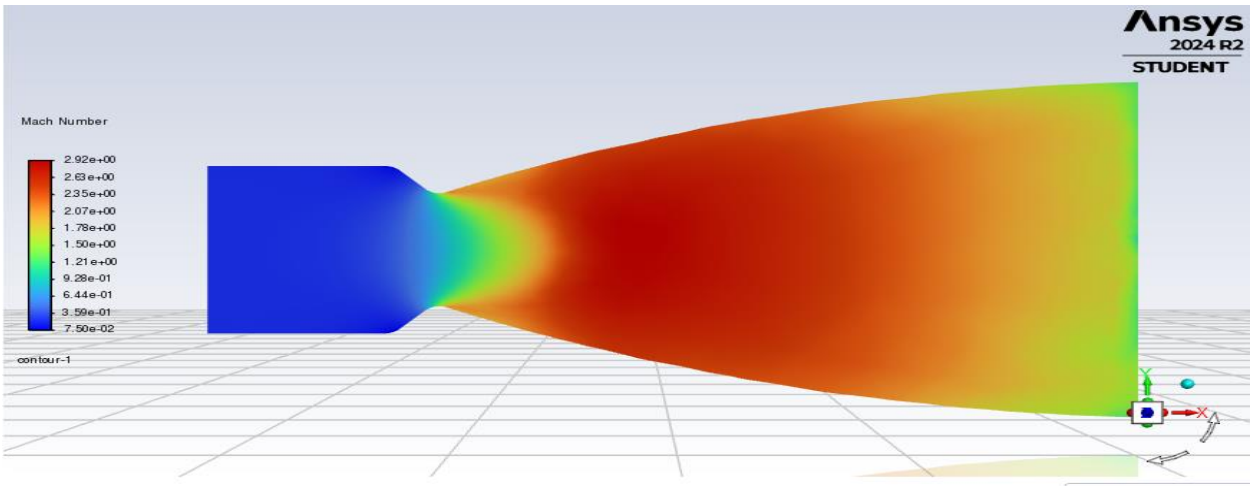

Figure 5.15 Mach distribution for bell nozzle

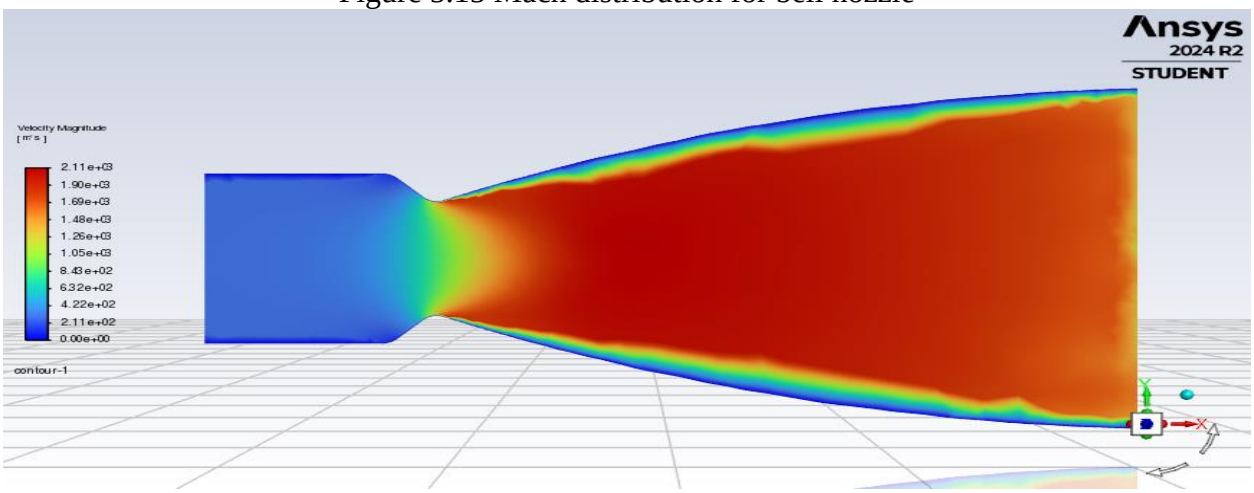

Figure 5.16 Velocity distribution for bell nozzle

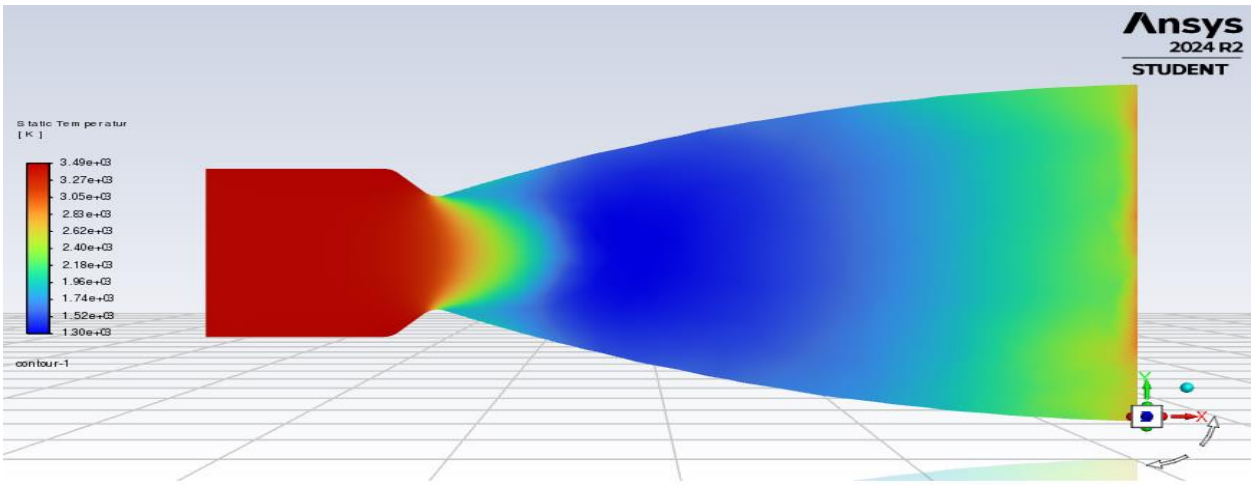

Figure 5.17 Static temperature distribution for bell nozzle

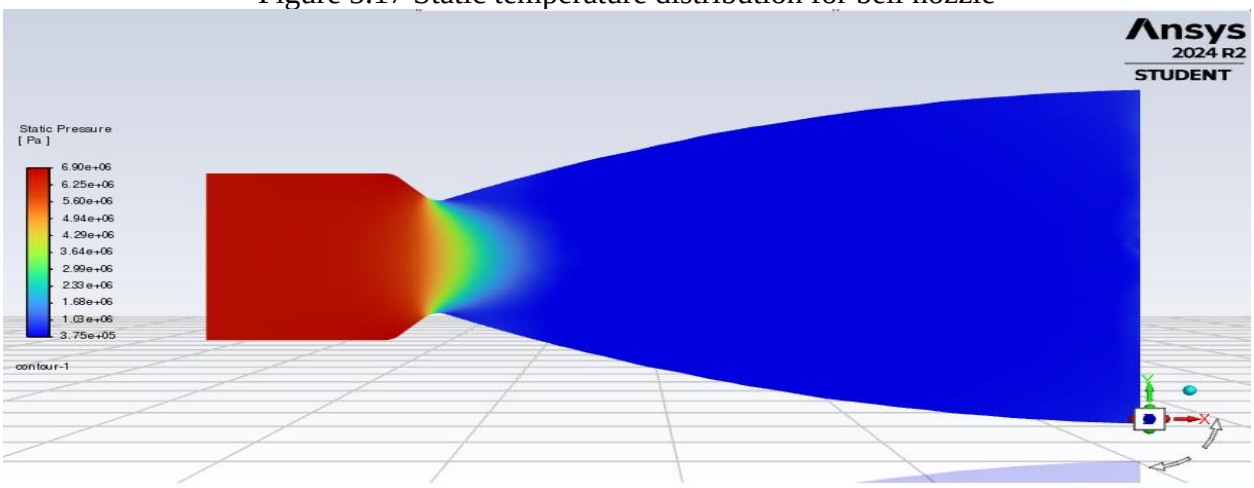

Figure 5.18 Static pressure distribution for bell nozzle

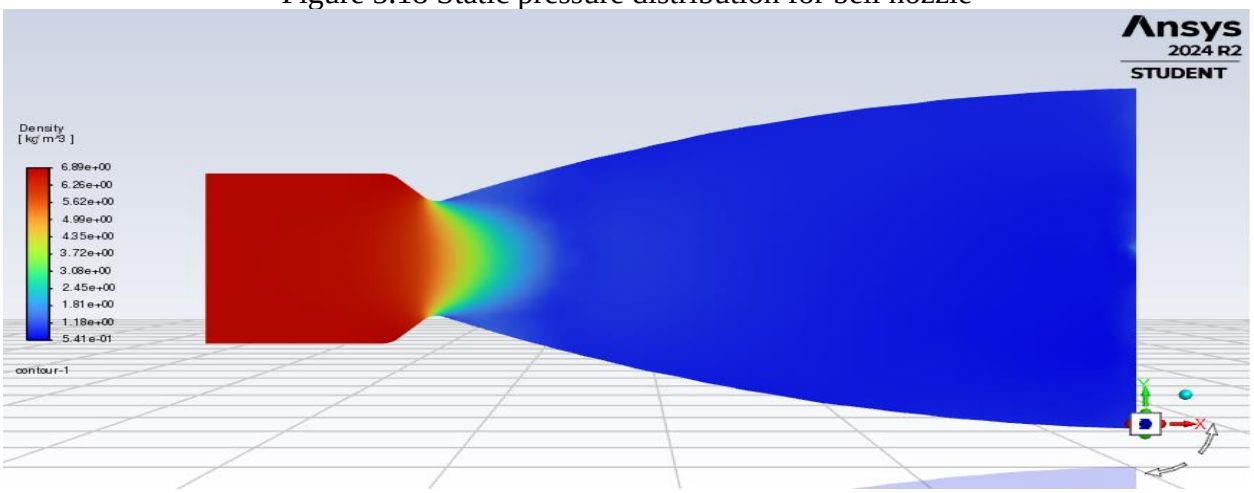

Figure 5.19 Density distribution for bell nozzle

5.5.3 Double Bell Nozzle Contour Distribution Planes

Figures 5.20 to 5.24 display the contour distribution planes for the double-bell nozzle configuration. On figures 5.20 and 5.21, the Mach and velocity distributions illustrate how the

flow expands through the first bell contour before transitioning to the second expansion contour. At sea level, the flow reaches a maximum velocity of approximately ~2240 m/s (Mach ~3.40) . However, at higher altitudes, the second contour would engage, reducing flow separation and further increasing the exit velocity.

Figures 5.22 and 5.23 represent the static temperature and pressure distributions, demonstrating a similar trend to the bell nozzle. The temperature and pressure decrease as the flow expands, with the second bell section mitigating energy losses. This staged expansion process ensures improved performance at varying altitudes. Finally, Figure 5.24 shows the density distribution, revealing the compressibility effects within the nozzle. The dual-expansion design maintains smoother density gradients, reducing the formation of shockwaves and enhancing the overall nozzle efficiency across a broader range of atmospheric pressures.

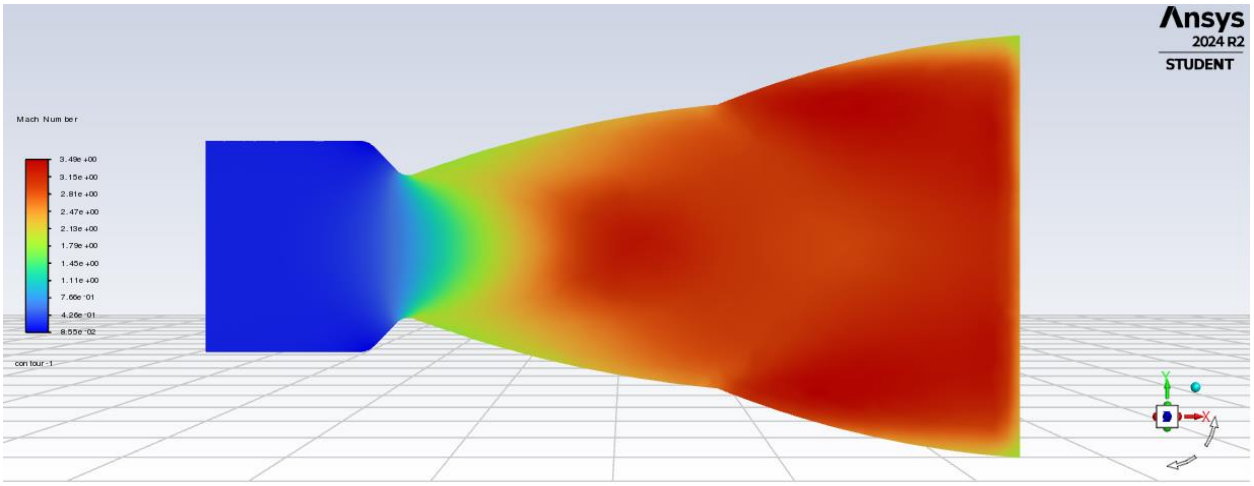

Figure 5.20 Mach distribution for double bell nozzle

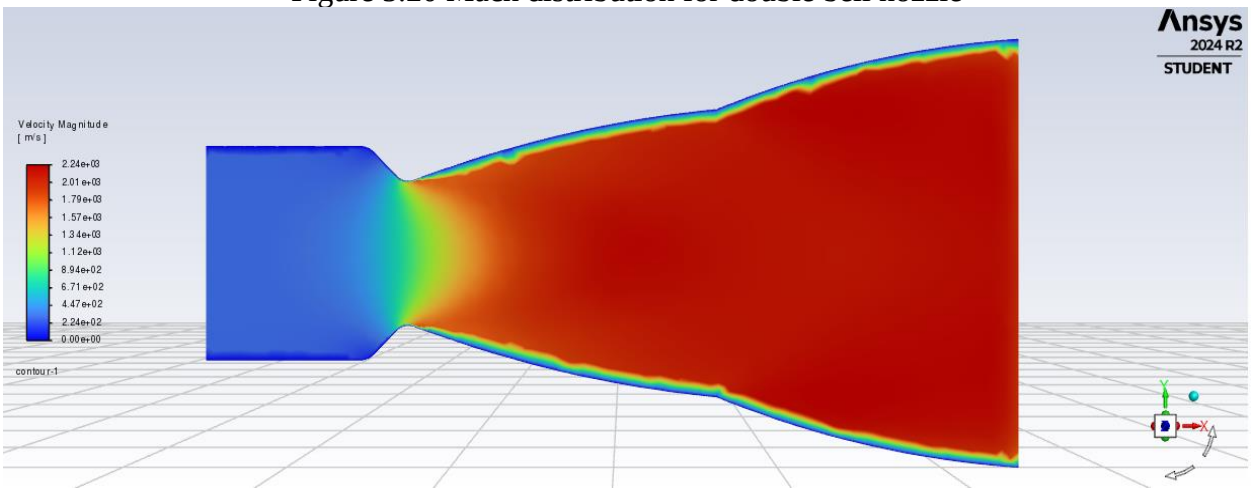

Figure 5.21 Velocity distribution for double bell nozzle

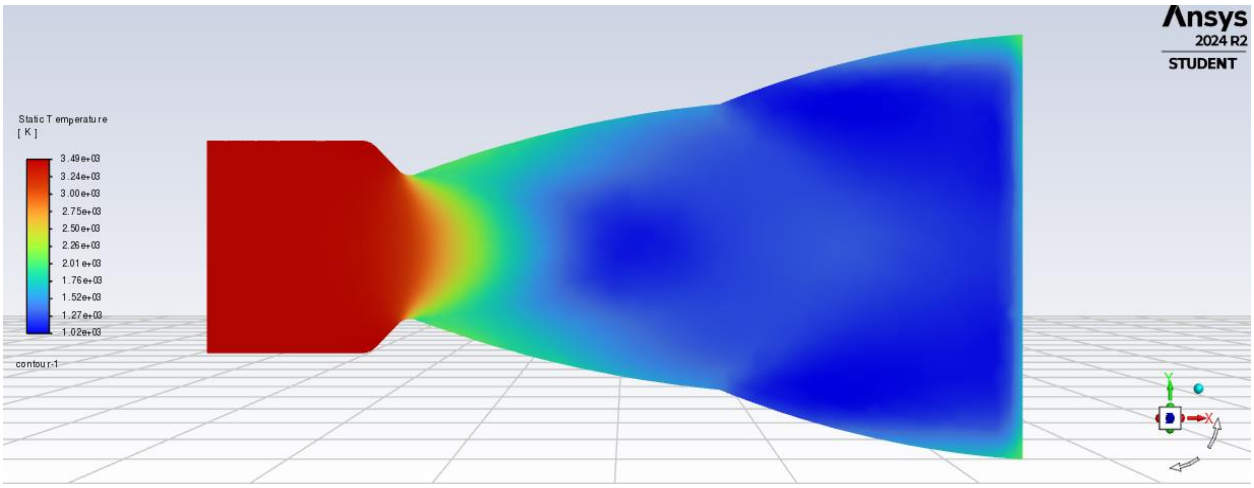

Figure 5.22 Static temperature distribution for double bell nozzle

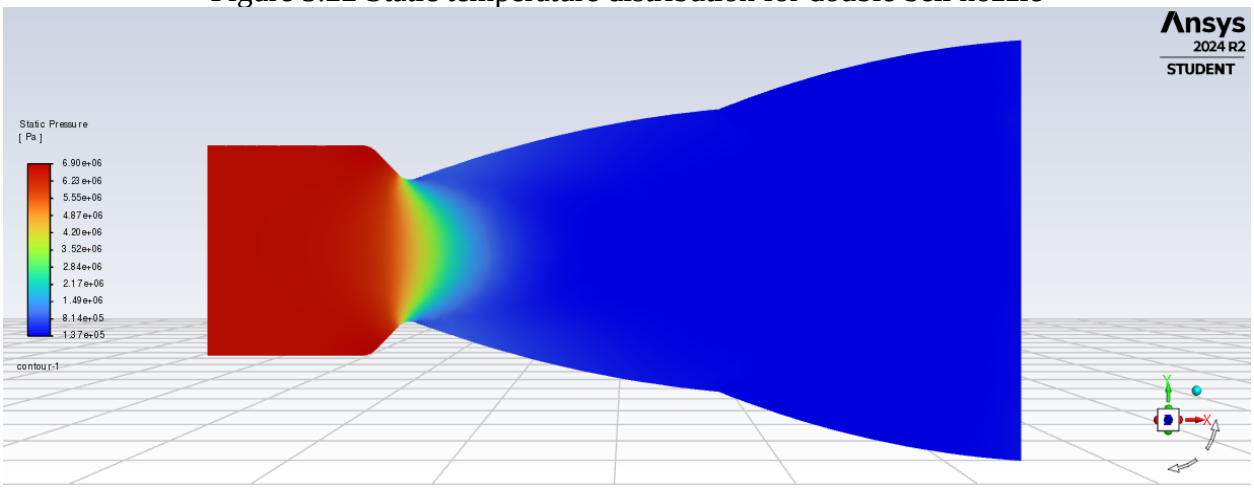

Figure 5.23 Static pressure distribution for double bell nozzle

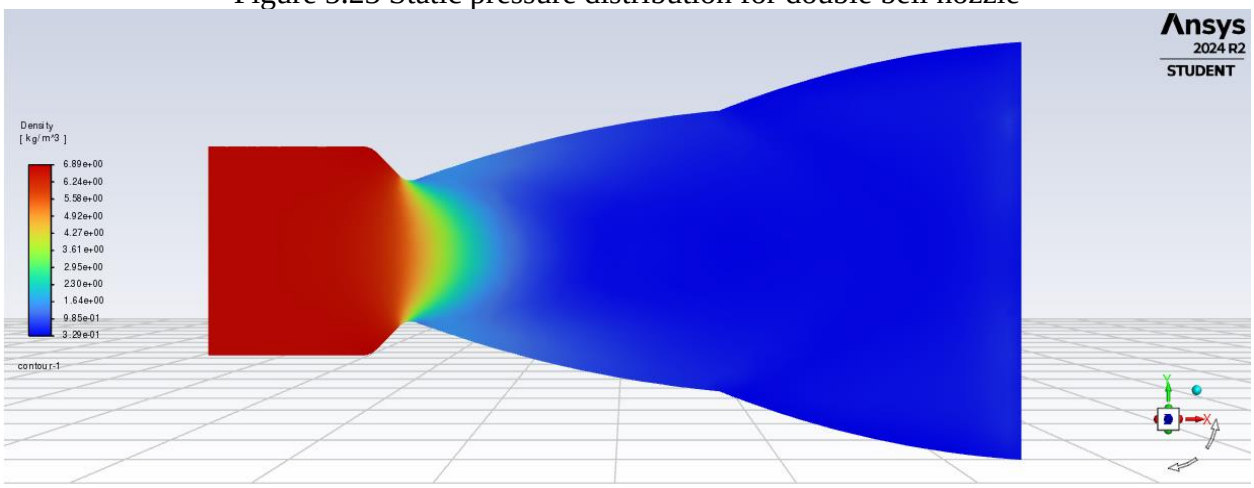

Figure 5.24 density distribution for double bell nozzle

5.5.4 Discussion of all the results

Based on the results of the CFD simulations, both single and double bell nozzles demonstrated the highest performance at sea level. Its parabolic contour efficiently expanded the

exhaust gases, achieving a high exit velocity and reducing the formation of shockwaves. The pressure and temperature distributions showed smooth and continuous flow expansion, resulting in minimal flow separation and low aerodynamic drag. Additionally, the density distribution indicated effective conversion of thermal energy into kinetic energy, maximizing thrust production.

The conic nozzle, while simpler in design, exhibited noticeable flow separation and higher pressure losses. The Mach number contours revealed inefficient expansion, with localized shockwave formation near the nozzle walls. This led to a lower exit velocity compared to the bell nozzle, confirming its reduced performance at sea level.

The double-bell nozzle displayed competitive performance under sea-level conditions, though its primary advantage lies in its adaptability at higher altitudes. While the Mach number and pressure contours at sea level were comparable to those of the bell nozzle, the dual-expansion contour of the double-bell nozzle would allow for improved flow expansion at reduced ambient pressures. This dynamic transition to the second expansion contour reduces flow separation and minimizes energy losses in vacuum or near-vacuum conditions.

Therefore, while the bell nozzle is optimal for low-altitude operations, the double-bell nozzle offers superior performance for multi-stage rockets or missions extending into the upper atmosphere. Future simulations at varying altitudes could further validate this expectation by analyzing how the nozzle adapts to different external pressures. Overall, the results reinforce the bell nozzle's suitability for sea-level launches and the double-bell nozzle's advantages for higher-altitude operations.

5.6 Conclusion

In this chapter, the aerodynamic performance of conic, bell, and double-bell nozzles was analyzed using CFD simulations to evaluate their effectiveness in minimizing drag and maximizing thrust. Both the single and double bell nozzle demonstrated the most efficient flow expansion and produced the highest exit velocity at sea level, owing to its parabolic contour that minimizes shock formation and flow separation. The double-bell nozzle, while slightly less efficient at sea level, showed promising adaptability for higher altitudes due to its dual-expansion design, which reduces energy losses during expansion.

The conic nozzle, although simpler and easier to manufacture, exhibited lower performance compared to the other two designs. Higher pressure losses and localized flow separation resulted in reduced exit velocity, confirming its limitations in high-performance applications.

The next chapter will focus on revisiting the aerospike nozzle simulation that had previously encountered meshing and convergence issues. In future chapters, further optimization of the aerospike nozzle configuration and several new design variations will be investigated, including modifications to throat area, chamber area, ramp curvature, and ambient pressure conditions, with the goal of identifying the most efficient aerospike geometry. Comparative studies between the updated aerospike designs and the baseline results will be conducted to assess improvements in aerodynamic and propulsion performance.

Chapter 6. 3D CFD Simulation of Aerospike Nozzle

6.1 Introduction

Following the challenges encountered in Chapter 5 regarding the 3D meshing of the aerospike nozzle, this chapter revisits the aerospike nozzle design by successfully conducting a full 3D CFD analysis. The initial difficulty stemmed from the complex geometry of the aerospike, where sharp corners created meshing errors within ANSYS. To resolve this, the aerospike geometry was refined by smoothing out sharp transitions, thereby facilitating a high-quality mesh generation. With the updated model, a comprehensive CFD analysis was performed to evaluate the aerodynamic behavior of the aerospike nozzle, specifically focusing on Mach number, velocity, pressure, temperature, density, and enthalpy distributions. The goal of this chapter is to assess the aerospike nozzle's performance and determine the corresponding exit velocity, enabling a direct comparison with previously analyzed nozzles.

6.2 Updated Geometry and Mesh

The redesigned aerospike nozzle was modeled using Autodesk Inventor. In the revised version, sharp edges at the nozzle base and spike tip were replaced with smooth fillets, minimizing abrupt curvature changes that previously hindered mesh generation. Figure 6.1 illustrates the previous design that was causing meshing difficulties, while figure 6.2 represents the updated version of the aerospike nozzle.

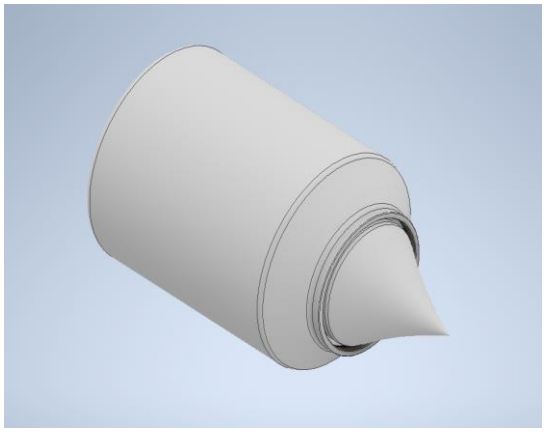

Figure 6.1 First iteration

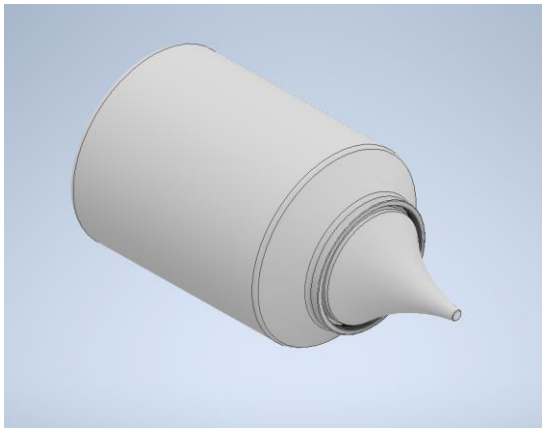

Figure 6.2 Second iteration

Below is a comparison of the 2D sketch of the aerospike nozzle for the first and second iteration as shown by figures 6.3 and 6.4. The main difference between them is the smooth out end of the aerospike. On figure 6.4, the second iteration shows a smoother end of the ramp surface, while the first iteration on figure 6.3 does not. In the initial iteration of the aerospike nozzle design, the spike tip was modeled with a sharp, pointed geometry rather than a smooth, rounded curvature. This sharp feature was the primary cause of the persistent meshing errors encountered in ANSYS, ultimately preventing successful mesh generation and simulation. The lack of smoothness at the tip created highly localized gradients and mesh distortion that the solver could not accommodate, necessitating a redesign of the geometry to include a smoother, more continuous surface profile.

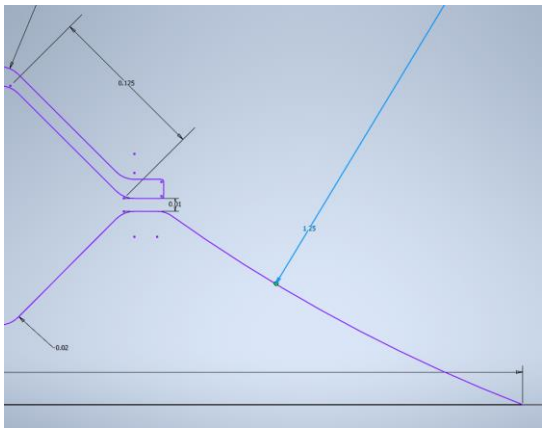

Figure 6.3 2D sketch of first iteration

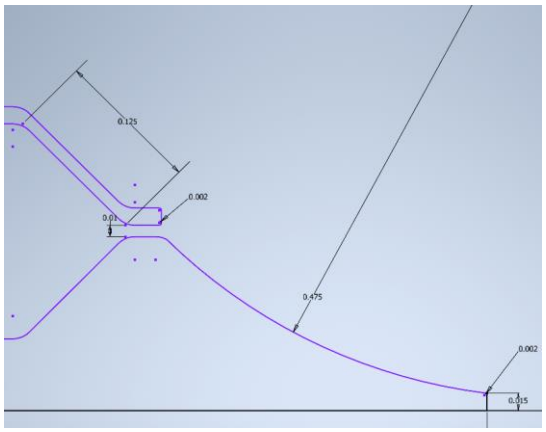

Figure 6.4 2D sketch of second iteration

It is also worth noting that the aerospike surface in this study was designed with a slight curvature rather than a purely flat ramp. This design choice was made as part of an experimental effort to explore alternative geometries and was partially inspired by the work of Liu et al. [5], who demonstrated that incorporating curvature into the aerospike ramp surface can promote more efficient, isentropic flow expansion in nozzle designs. After exporting the geometry as a STEP file, the model was imported into ANSYS Fluent.

Within ANSYS, a body-fitted mesh was created using tetrahedral elements, suitable for capturing the complex aerospike contours. Additional mesh refinements were applied near the nozzle throat, spike surface, and flow expansion regions to accurately resolve high gradients in pressure, temperature, and velocity.

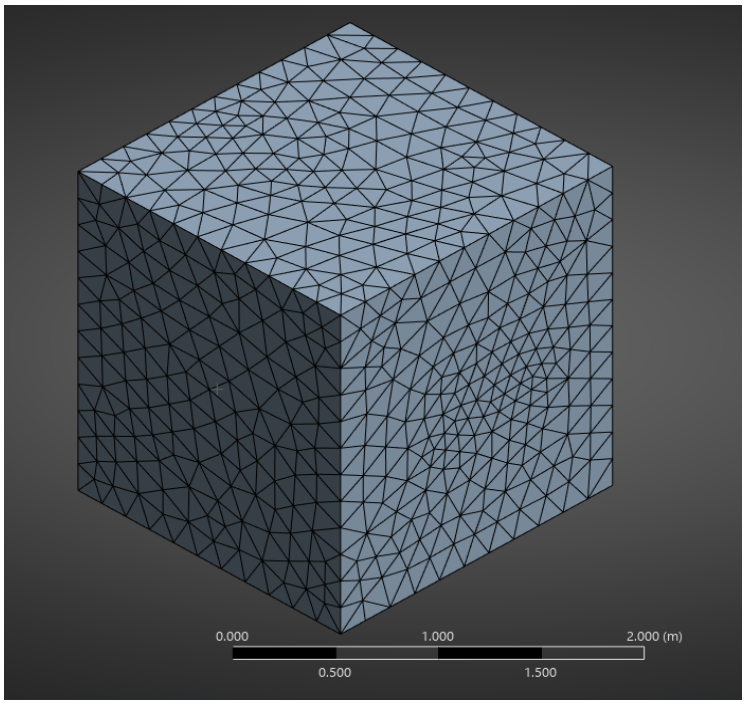

Figure 6.5 Domain mesh of Aerospike

Mesh sizing at the throat region was set to 0.0001 m with a gradual growth rate of 1.05 to ensure smooth transition and minimize numerical errors. A mesh independence study was conducted to verify that further refinements did not significantly change the simulation results, ensuring both accuracy and computational efficiency.

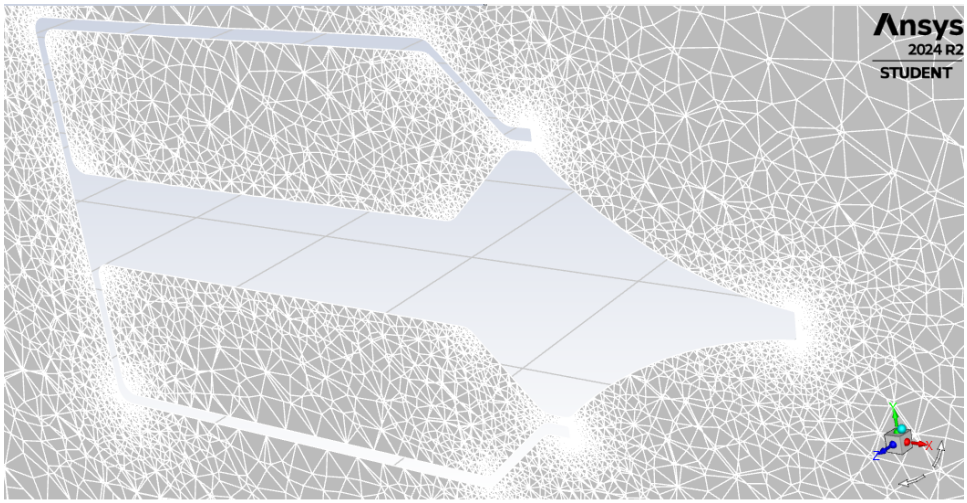

Figure 6.6 Final mesh of Aerospike

6.3 Physics and Simulation Setup

The simulation was conducted under steady-state, compressible flow conditions using ANSYS Fluent. The governing equations applied were the compressible Navier-Stokes equations, coupled with the k-ω Shear Stress Transport (SST) turbulence model to accurately capture boundary layer separation and shock structures.

Boundary Conditions:

- Inlet: Total pressure of 7 MPa and total temperature of 3500 K, representing typical combustion chamber conditions.
- Outlet: Static pressure set to 101,325 Pa, simulating sea-level atmospheric conditions.
- Walls: Adiabatic no-slip walls.

Assumptions:

- Air was modeled as an ideal gas.
- Gravity effects were neglected.
- No chemical reactions or phase changes were considered.

These settings mirror those used in Chapters 3 to 5 to maintain consistency across all nozzle evaluations.

6.4 Aerospike Nozzle CFD Results

The following contour distributions were obtained for the aerospike nozzle:

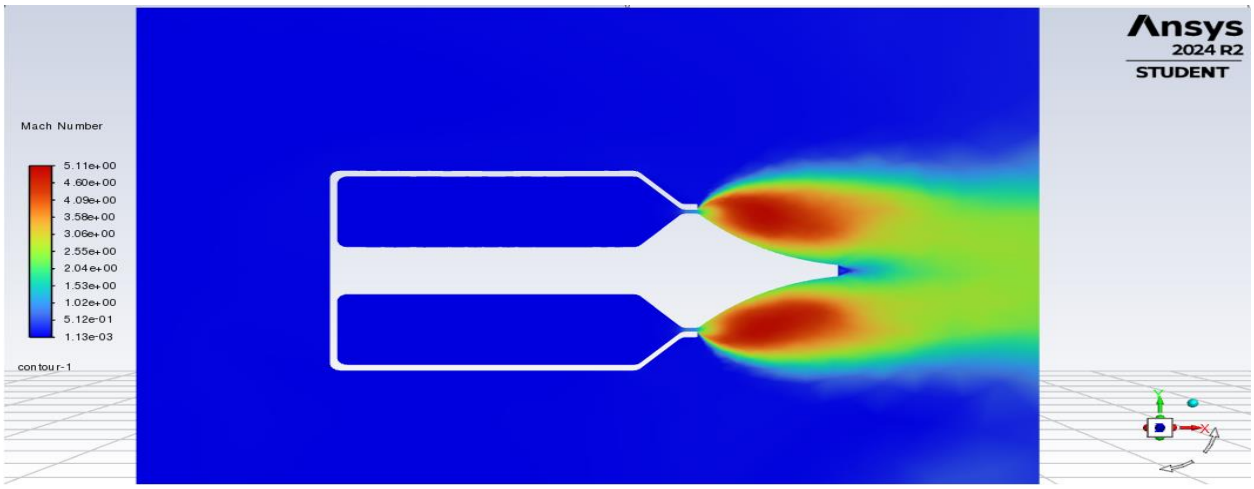

Figure 6.7 Mach distribution for aerospike nozzle

The Mach distribution illustrates a robust acceleration of flow along the aerospike surface, reaching supersonic speeds downstream of the throat. A maximum Mach number of approximately 5.11 was observed along the exit of the throat and downstream at the nozzle exit the flow slowed down to a Mach number of about 3.06.

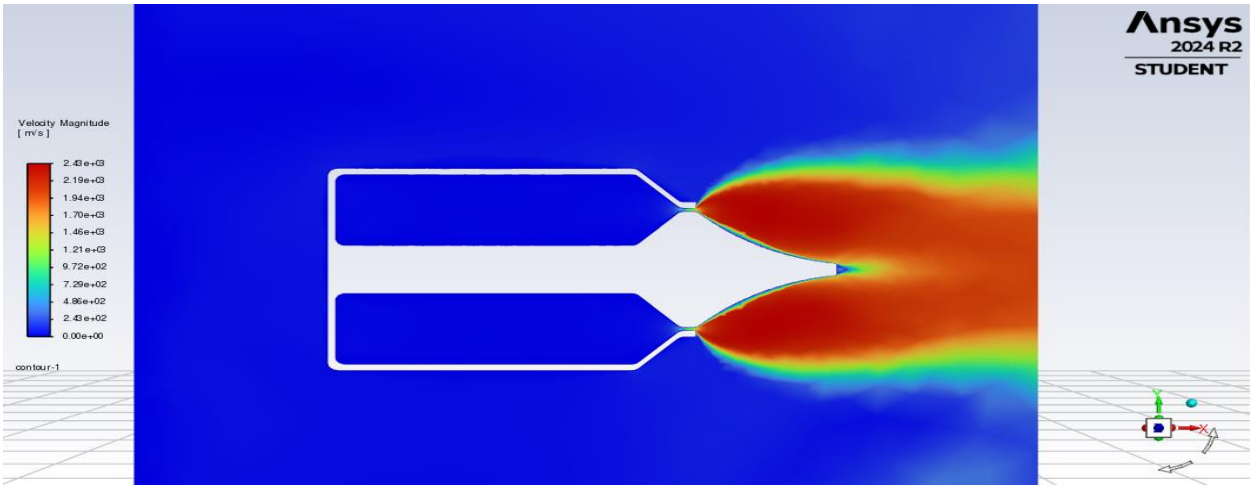

Figure 6.8 Velocity distribution for aerospike nozzle

Velocity distribution reveals a maximum exit velocity of approximately 2,430 m/s at the nozzle exit plane. The flow accelerates progressively along the spike, demonstrating the aerospike's capability to maintain high exit velocities without requiring a conventional bell expansion.

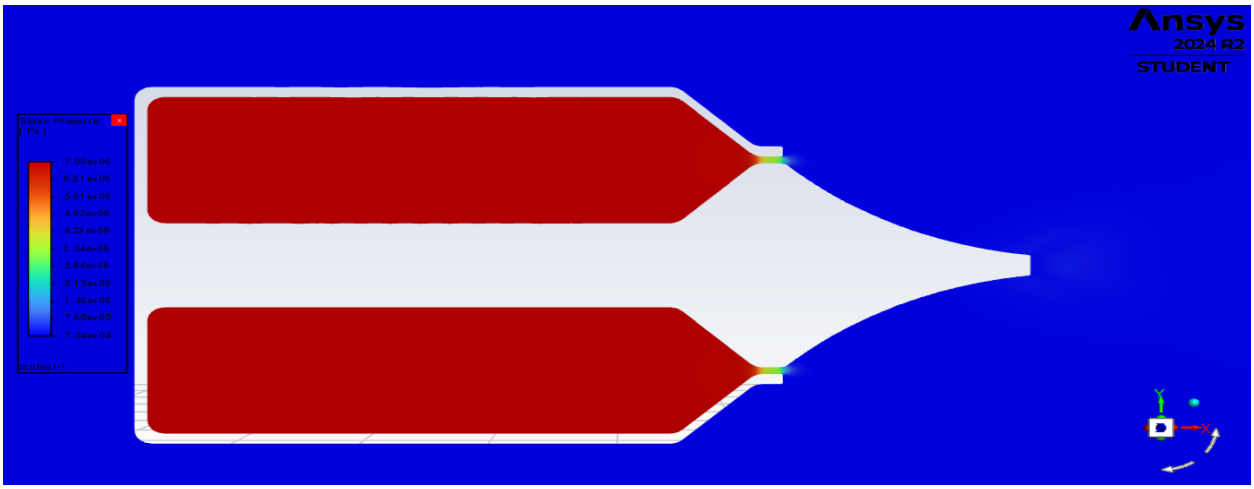

Figure 6.9 Static pressure distribution for aerospike nozzle

The pressure distribution shows a gradual decrease from the combustion chamber to the nozzle exit.

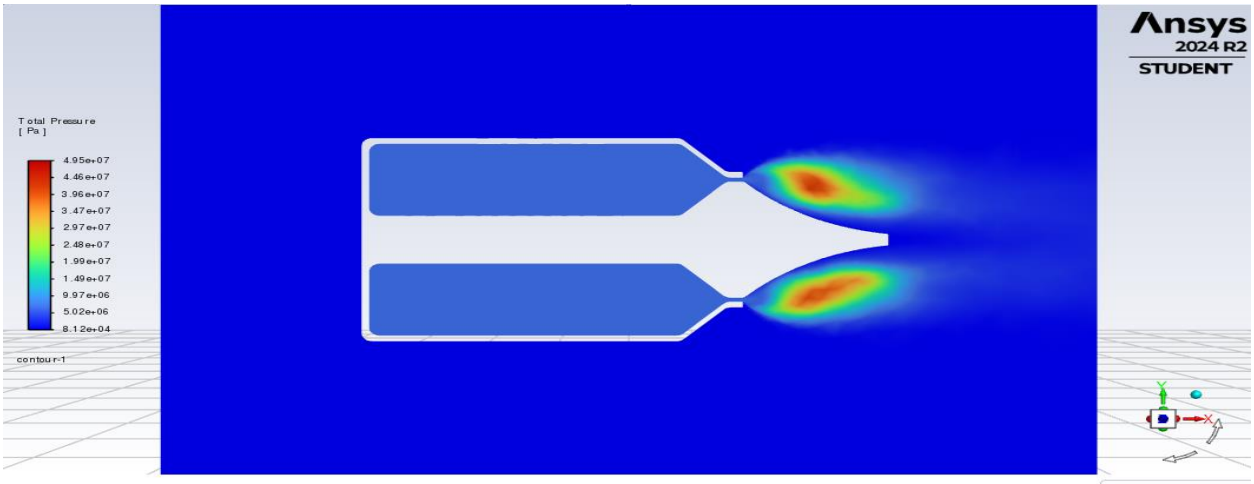

Figure 6.10 Total pressure distribution for aerospike nozzle

Figure 6.10 illustrates the total pressure distribution across the aerospike nozzle. High total pressure values are concentrated near the combustion chamber, gradually decreasing along the length of the nozzle and through the exhaust jet. This pattern confirms the expected energy transformation within the flow, where thermal and pressure energy is converted into kinetic energy as the flow accelerates downstream. The symmetry and smooth decay of total pressure also indicate minimal shock losses and efficient isentropic expansion along the ramp surface, a key performance indicator for optimized nozzle designs. The preserved core of high total pressure in the jet wake suggests strong thrust-carrying capability and efficient momentum transfer.

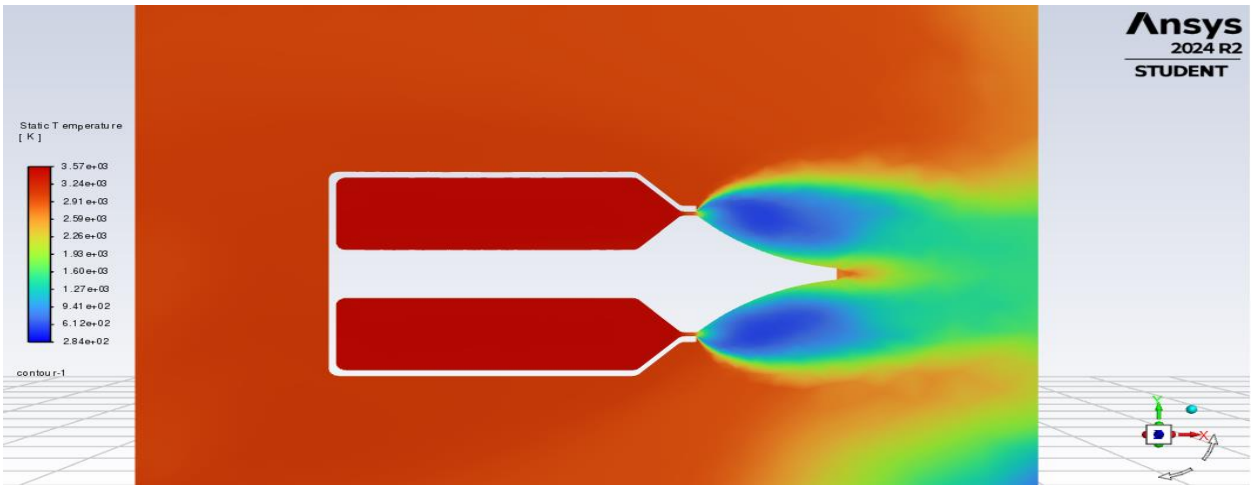

Figure 6.11 Static Temperature distribution for aerospike nozzle

Static temperature decreases significantly along the flow path, from the initial combustion temperature to much lower values at the nozzle exit. This energy conversion from thermal to kinetic energy is characteristic of effective nozzle designs. On figure 6.11, the static temperature drops from 3570 K down to a minimum of 284 K.

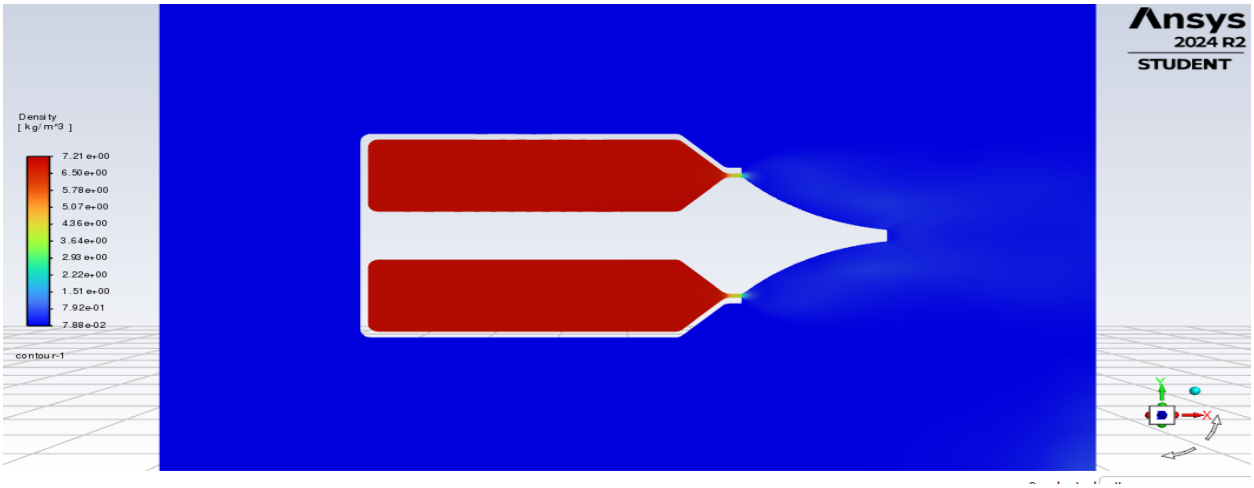

Figure 6.12 Density distribution for aerospike nozzle

A reduction in density is observed as the flow accelerates, consistent with compressible flow behavior through an expanding nozzle.

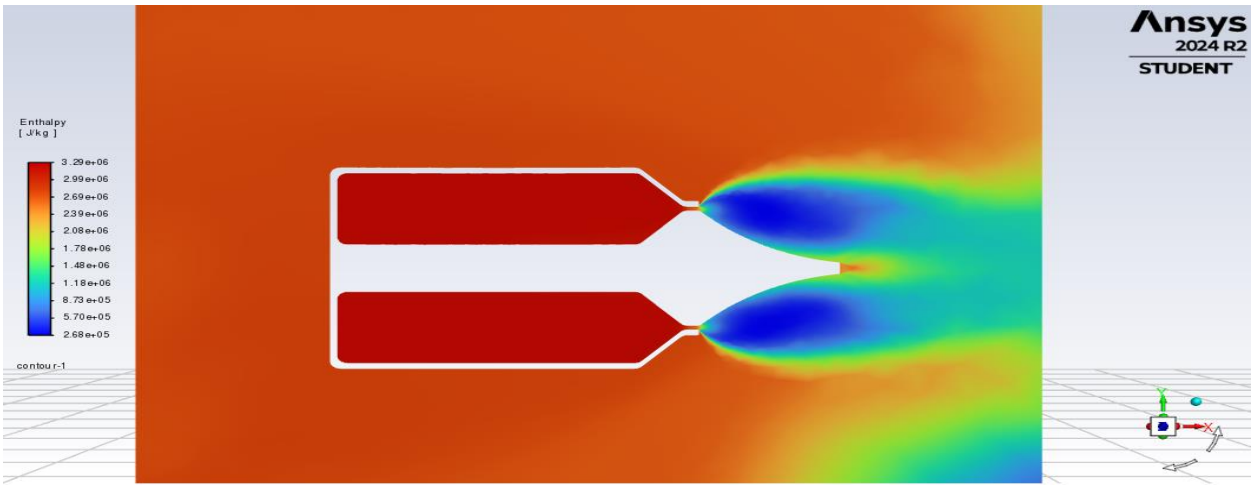

Figure 6.13 Enthalpy distribution for aerospike nozzle

The enthalpy distribution provides further insight into the energy transformation within the nozzle. High enthalpy regions near the combustion chamber decrease progressively along the spike surface, correlating with the acceleration of the flow and the drop in static temperature. This indicates an effective conversion of thermal energy into kinetic energy, reinforcing the aerodynamic efficiency of the aerospike nozzle design. The initial Enthalpy at the combustion chamber reads $3.29 * 10^6$ J/kg and as the flow accelerates down the nozzle throat out the exit, the enthalpy decreases to a minimum of $2.68 * 10^5$ J/kg.

6.5 CFD Validation

To further strengthen the credibility of the CFD results, theoretical calculations based on classical nozzle expansion relations were applied based on classical nozzle expansion theory, as outlined by Liu et al. [5]. Using the nozzle pressure ratio (NPR) derived from the combustion chamber and ambient pressures, the exit Mach number was estimated through isentropic flow equations. The exit Mach number (M_e) can be estimated from the nozzle pressure ($NPR = P_c/P_a$) ratio as follows:

$$Me = \sqrt{[2/(\gamma - 1) * ((NPR)\text{^}((\gamma - 1)/\gamma) - 1)]} \quad (6.1)$$

The theoretical exit Mach number was calculated to be 3.43, which closely matched the Mach number observed in the CFD simulations ($M_{CFD} = 3.06$) , reinforcing the validity of the computational results.

Additionally, the theoretical area ratio A/A_t was determined, which describes the necessary expansion from the nozzle throat to the exit for achieving the target supersonic Mach number. The area ratio (A/A_t)throughout the nozzle is governed by:

$$A/At = (1/M) * [2/(\gamma + 1) * (1 + (\gamma - 1)/2 * M^2)]\text{^}((\gamma + 1)/(2(\gamma - 1))) \quad (6.2)$$

This area ratio serves as a critical geometric constraint in supersonic nozzle design, ensuring that the nozzle cross-sectional expansion is consistent with the desired flow acceleration. The agreement between the CFD-predicted expansion behavior and the theoretical area ratio

further validated the accuracy of the mesh design and boundary condition setups. This equation will be further utilized in a future chapter to optimize the aerospike nozzle.

The Prandtl-Meyer expansion angle ω was also calculated to assess the required isentropic turning of the flow along the aerospike surface. The expansion angle associated with a given Mach number can be determined using the Prandtl-Meyer function:

$$\omega = \sqrt{[(\gamma + 1)/(\gamma - 1)]} * tan^{-1}[\sqrt{((\gamma - 1)/(\gamma + 1) * (M^2 - 1))}] - tan^{-1}[\sqrt{(M^2 - 1)}] \quad (6.3)$$

This expansion angle is essential for designing the ramp curvature to enable smooth, shock-free expansion of the flow. The geometry's ramp angle is estimated to be about 55 degrees and on the theoretical side, using the Prandtl-Meyer function, it was calculated to be about 57 degrees. By comparing the computed Prandtl-Meyer angles to the observed flow turning in the simulation, it was confirmed that the aerospike geometry supported nearly ideal isentropic expansion, minimizing total pressure losses and maximizing thrust efficiency.

To evaluate nozzle performance further, thrust contributions were considered, outlined by Liu et al. [5]. The thrust generated at the exit plane, ramp surface, and base were estimated using:

$$F_{exit} = \dot{m} * W_{exit} + (P_{exit} - P_a) * A_{exit} \quad (6.4)$$

$$F_{ramp} = \int (P_w - P_a)\, dA_{ramp} \quad (6.5)$$

$$F_{base} = \int (P_w - P_a)\, dA_{base} \quad (6.6)$$

where $\dot{m}$ is the mass flow rate, $W_{exit}$is the axial velocity at the exit, $P_{exit}$is the static pressure at the exit, P_{wall} is the wall pressure, $P_a$is ambient pressure, and A represents respective areas. The total thrust is obtained by:

$$F = F_{exit} + F_{ramp} + F_{base} + F_{friction} \quad (6.7)$$

These theoretical evaluations complement the CFD results and help quantify the efficiency of the aerospike nozzle configuration, however for this case, F_{base} and $F_{friction}$ will be neglected, due to their small contribution to the overall thrust. The simulation assumes ideal conditions, such as no slip walls and negligible friction. Thus, the only force to be calculated is F_{exit} which will be the overall estimated thrust for the nozzle. The calculated thrust using theoretical relations showed strong consistency with the net forces measured directly in ANSYS Fluent, further validating the CFD setup. This multi-pronged validation approach involving flow Mach numbers, expansion area ratios, turning angles, and thrust measurements, provides confirmation that the simulated aerospike nozzle performance accurately reflects physical behavior.

Table 6.1 Summary of values comparing CFD vs theoretical results

Quantities	Theoretical	CFD	Percent error

Exit Mach (M_{exit})	3.43	3.06	12.09%
Exit Velocity (v_{exit}) [m/s]	2750.65	2430	13.20%
Area ratio (A/A_t)	6.364	6.6	3.58%
Prandtl-Meyer Expansion Angle ω	57.411	55	4.38%
Exit Thrust (F_{exit}) [N]	338467.24	298000	13.58%

As seen from Table 6.1, the comparison between theoretical and CFD results shows strong agreement across all critical performance metrics. The calculated exit Mach number of 3.43 closely aligns with the CFD-predicted value of 3.06, with a percent error of just 12.09%. Similar trends are observed in exit velocity and thrust, where deviations remain under 14%. The small discrepancy is expected due to the simplifications inherent in the theoretical model, which assumes ideal conditions and neglects effects such as turbulence and viscous dissipation.

Notably, the area ratio and Prandtl-Meyer expansion angle exhibit extremely low percent errors of 3.58% and 4.38%, respectively. This provides strong validation that the nozzle geometry, including the throat expansion and ramp angle, was appropriately designed to support isentropic flow expansion. Furthermore, the thrust predicted by Fluent (298,000 N) was in good agreement with the analytically computed thrust (338,467 N), affirming the simulation's accuracy in capturing momentum and pressure forces across the nozzle exit.

6.7 Discussion

The aerospike nozzle performed exceptionally well in both CFD and theoretical analyses. Unlike traditional conical or bell-shaped nozzles explored in earlier chapters, the aerospike maintains high exit velocity and thrust performance. This is evident in the smoother Mach and pressure gradients observed along the nozzle ramp, as well as the concentrated total pressure core in the jet stream. In chapter 7, more experimental studies will be analyzed across a wide range of ambient pressures for the aerospike nozzle.

Compared to the conic and bell nozzles previously analyzed, the aerospike demonstrated reduced total pressure losses, lower boundary layer separation, and better preservation of kinetic energy in the exhaust jet. The integrated ramp structure allows for continuous, efficient flow turning, eliminating the need for a diverging section while still achieving high supersonic speeds. Additionally, the curved ramp surface, an innovation inspired by Liu et al. [5], enabled more

isentropic expansion, confirmed by the close agreement between the simulated and theoretical Prandtl-Meyer angles.

These factors collectively contribute to the aerospike nozzle's superior performance in both thrust generation and expansion efficiency. The CFD results reinforce the design's potential for real-world applications, particularly in high-performance or variable-altitude aerospace missions.

6.8 Conclusion

In conclusion, Chapter 6 successfully revisited the aerospike nozzle through a complete 3D CFD analysis, following the resolution of prior meshing challenges. The updated geometry enabled accurate simulation of key flow parameters, including velocity, pressure, Mach number, temperature, density, and enthalpy. The results confirmed high-speed, isentropic flow expansion across the nozzle ramp.

The CFD results were validated using theoretical equations derived from classical compressible flow theory, including calculations of exit Mach number, area ratio, Prandtl-Meyer expansion angle, and thrust. The close agreement between simulation and theory emphasizes the reliability of the nozzle design and simulation setup.

These findings layed a foundation for continued optimization. In Chapter 7, this work will be extended by conducting a parametric study of the aerospike geometry, exploring how modifications to the throat diameter, ramp curvature, and chamber area may further enhance nozzle performance. The goal will be to fine-tune the nozzle configuration to achieve even higher thrust efficiency under various flight conditions.

Chapter 7. Parametric Optimization of Aerospike Nozzle

7.1 Introduction

Building upon the validated 3D CFD analysis of the baseline aerospike nozzle conducted in Chapter 6, this chapter focuses on the parametric optimization of the aerospike geometry. While the original design demonstrated excellent performance, further improvements may be achievable by strategically adjusting key geometric and environmental parameters.

Four distinct configurations will be investigated in this chapter:

- Variation of throat area,
- Variation of chamber area,
- Variation of ramp curvature,
- Variation of ambient pressure conditions.

Each configuration aims to enhance specific aspects of nozzle performance, such as maximizing thrust, minimizing flow separation, or improving expansion efficiency across varying altitudes. CFD simulations will be conducted for each case, and results will be compared against the baseline aerospike nozzle from Chapter 6. Additionally, theoretical predictions using classical nozzle expansion theory will be employed to validate the CFD findings, with comparative data summarized in tabular form similar to the approach used previously.

The ultimate objective of this chapter is to identify the most optimal aerospike nozzle configuration based on aerodynamic efficiency, thrust output, and practical manufacturability considerations.

7.2 Geometric and Environmental Variations

The following parametric changes will be applied:

Table 7.1 Summary of configurations

Configuration	Parameter Varied	Change
Base Config	None	Serves as the baseline for comparison
Config 1	Throat Area	Decreased 10%
Config 2	Chamber Area	Increased 15%
Config 3	Ramp Curvature	Increased curvature (sharper ramp)
Config 4	Combination	Combines all three previous configurations into one

These variations were selected based on their significant influence over nozzle expansion behavior, flow attachment, and overall thrust efficiency. Other variables, such as inlet total pressure and temperature, will remain consistent with Chapter 6 unless otherwise noted to isolate the effects of each geometric or environmental change.

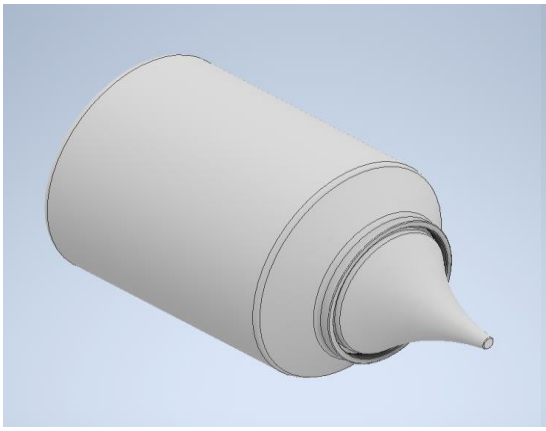

Figure 7.1 Configuration 1

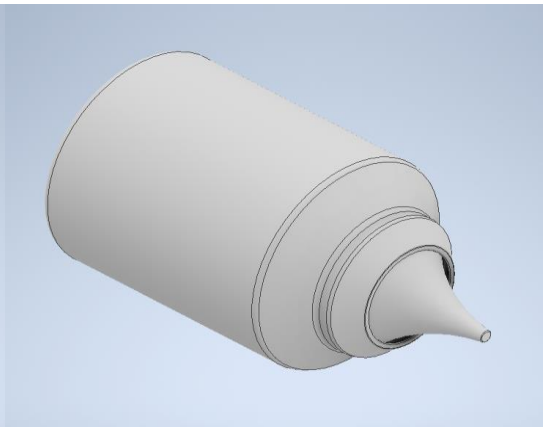

Figure 7.2 Configuration 2

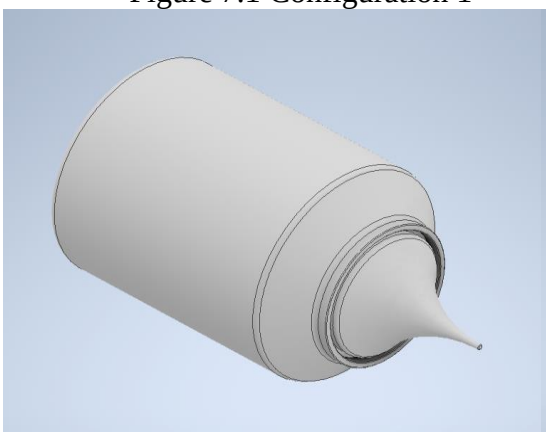

Figure 7.3 Configuration 3

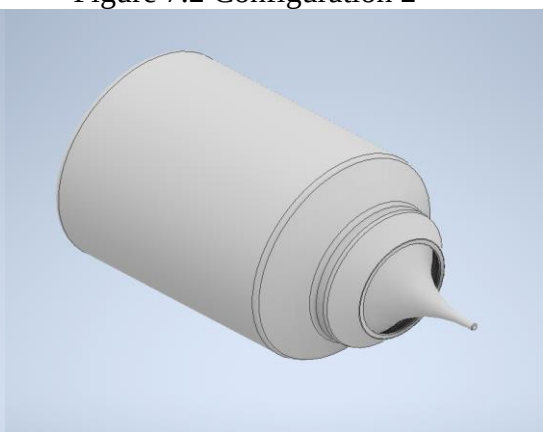

Figure 7.4 Configuration 4

At first glance, looking and comparing the figures above, one might notice that there isn't much that changed between the different configurations. However, by taking a closer inspection of the images, one can notice some details differ from the configurations, figure 7.3 and 7.4 seem to have a sharper ramp than the configurations on figures 7.1 and 7.2. Moreover, Configuration 2 and 4 show similarities in their newly implemented chamber configurations. Below are figures of the configurations depicting a better understanding of the main differences between the configurations.

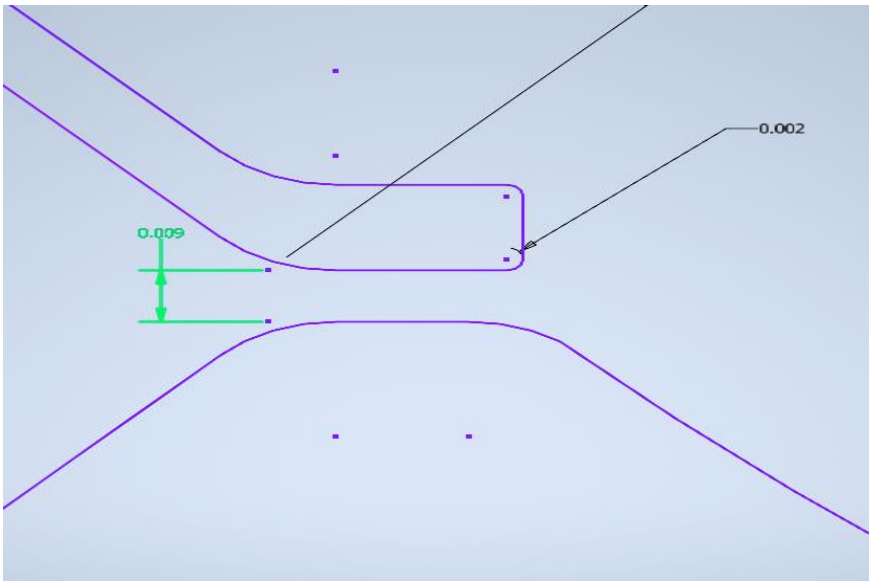

Figure 7.5 Close up view of throat diameter reduction for config. 1

Figure 7.5 presents a close-up view of Configuration 1, highlighting the reduction in the throat area. This modification was achieved by revisiting the baseline aerospike nozzle design and adjusting the throat diameter, which had been recalculated in advance using simple algebraic relations.

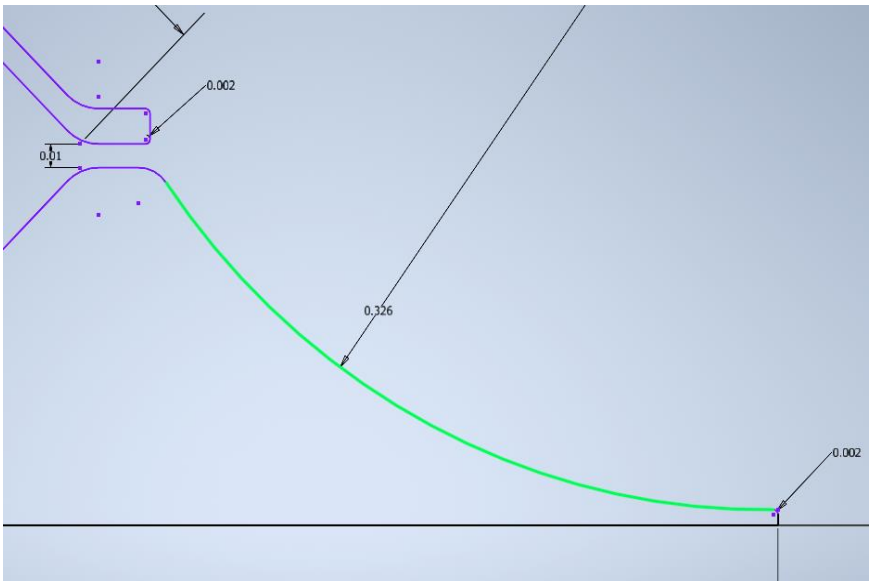

Figure 7.6 Close up view of ramp variation for config. 3

Figure 7.6 highlights the ramp modification for Configuration 3, featuring a noticeably steeper profile compared to the baseline design from Chapter 6. In the original configuration, the ramp was defined by an arc radius of 0.475 meters, whereas the updated configuration utilizes a tighter curvature with a reduced radius of 0.326 meters.

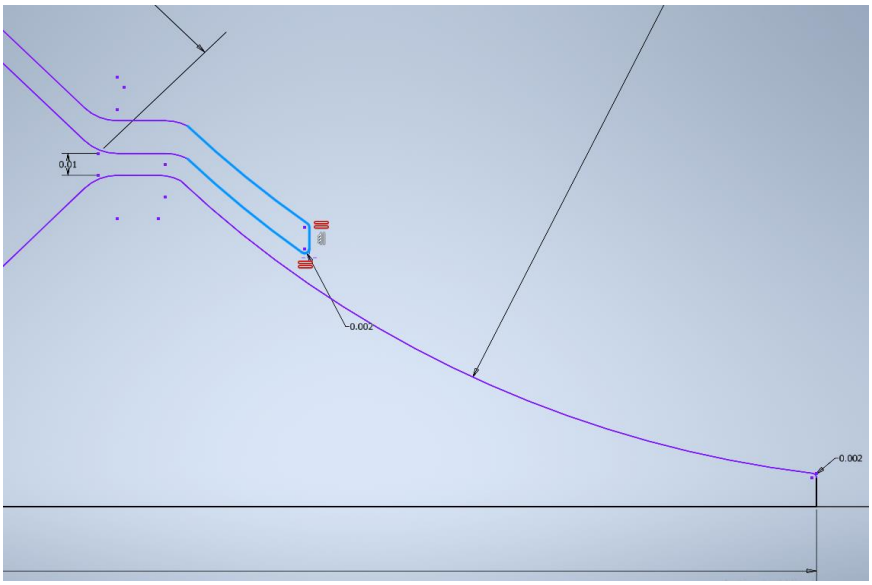

Figure 7.7 Close up view of chamber addition for config. 2

Figure 7.7 presents a close-up view of Configuration 2, where it is immediately apparent that the chamber extends further along the ramp surface. This design modification was introduced with the intention of better preserving the flow's energy and minimizing potential losses during expansion.

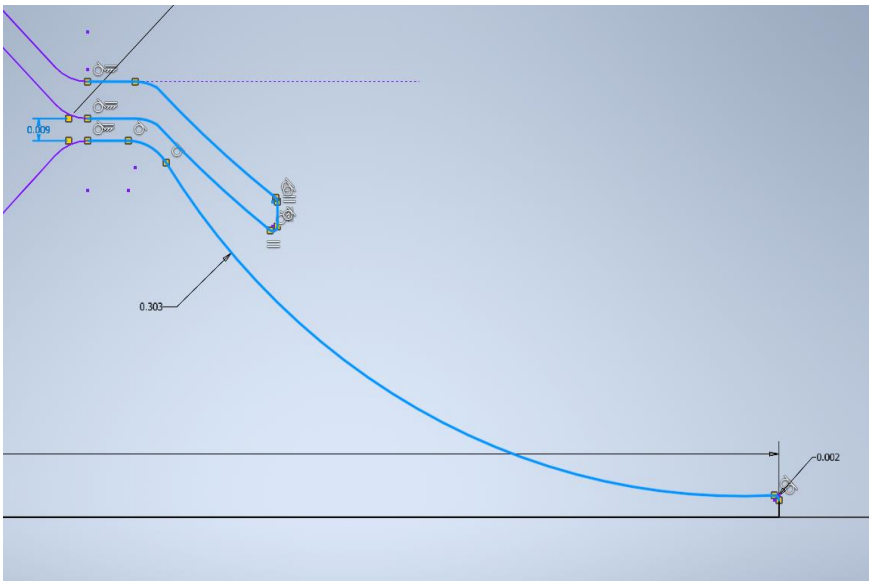

Figure 7.8 Close up view of changes added for config. 4

Figure 7.8 illustrates the final configuration, which combines the design changes from the previous three configurations into a single modified aerospike nozzle. The ramp curvature and throat reduction remain consistent with those introduced in Configurations 1 and 3. At first glance, the chamber exit area may appear different from that of Configuration 2, and it's in fact larger. The chamber design from Configuration 2 was directly incorporated into Configuration 4, as were the modifications from the other configurations. When combined, these changes result in an indirect

increase in the chamber exit area, primarily due to the simultaneous implementation of the ramp steepening and chamber extension.

7.3 Simulation Setup

The simulation methodology remains consistent with Chapter 6:

- Steady-state, compressible Navier-Stokes equations,
- k-ω SST turbulence model,
- Ideal gas assumption,
- No-slip, adiabatic wall boundary conditions,
- Pressure inlet and pressure outlet boundary setup.

Mesh refinement near the throat and ramp regions will be performed to ensure sufficient resolution of critical flow features, such as shock waves, expansion fans, and separation zones.

Each simulation will yield distribution results for:

- Mach number
- Velocity
- Density
- Total pressure
- Static temperature
- Enthalpy

The same theoretical equations used in Chapter 6 will be applied to calculate:

- Exit Mach number, M_e
- Exit velocity, v_e
- Thrust output. F_{exit}

This approach allows for direct and meaningful comparisons between the theoretical predictions and CFD simulation results for each configuration to help determine the most optimal aerospike design.

7.4 Results

7.4.1 Configuration 1 results at 51235 Pa

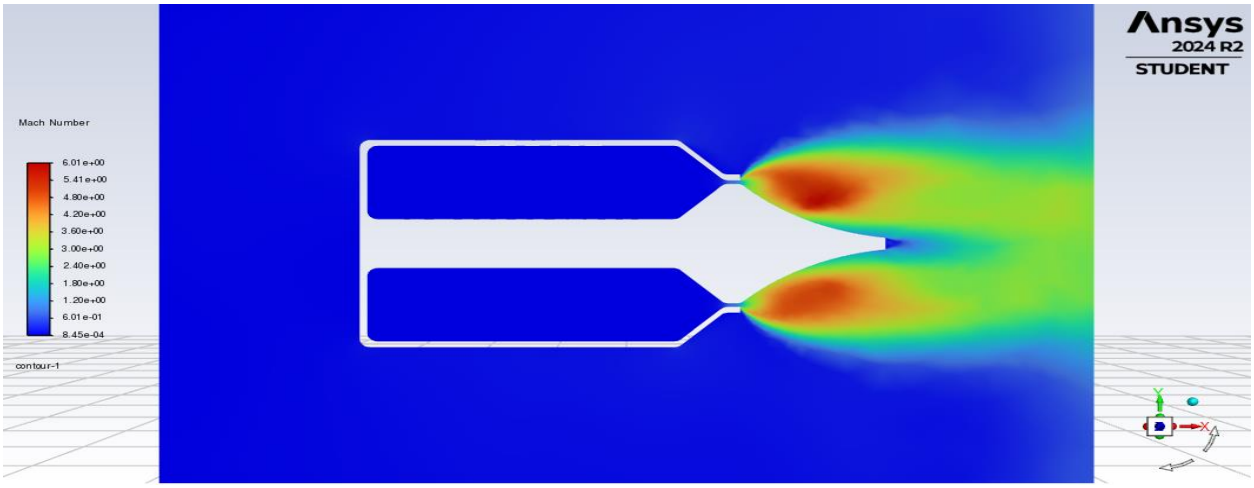

Figure 7.9 Mach distribution for config. 1

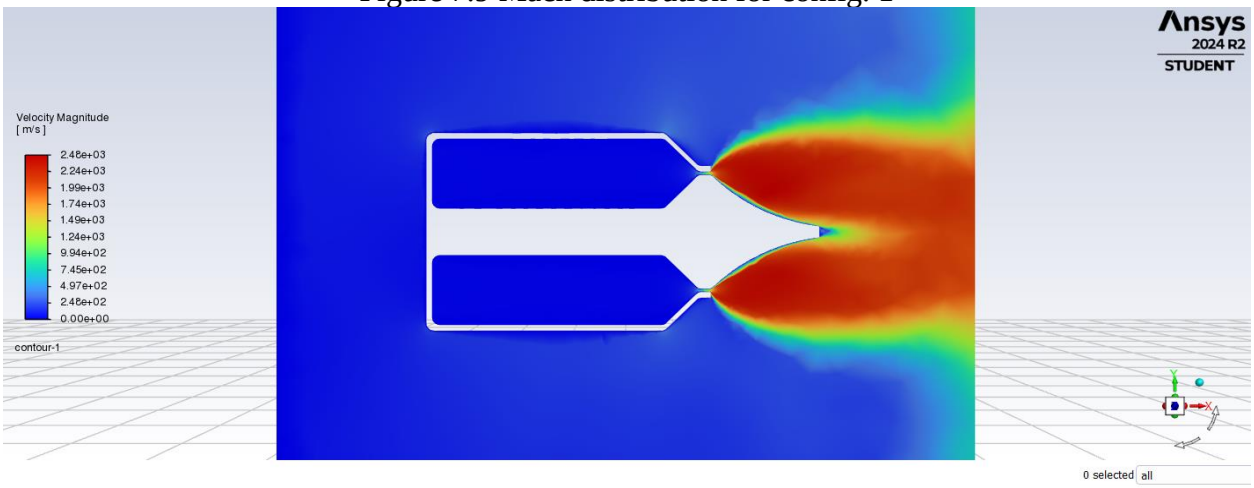

Figure 7.10 Velocity distribution for config. 1

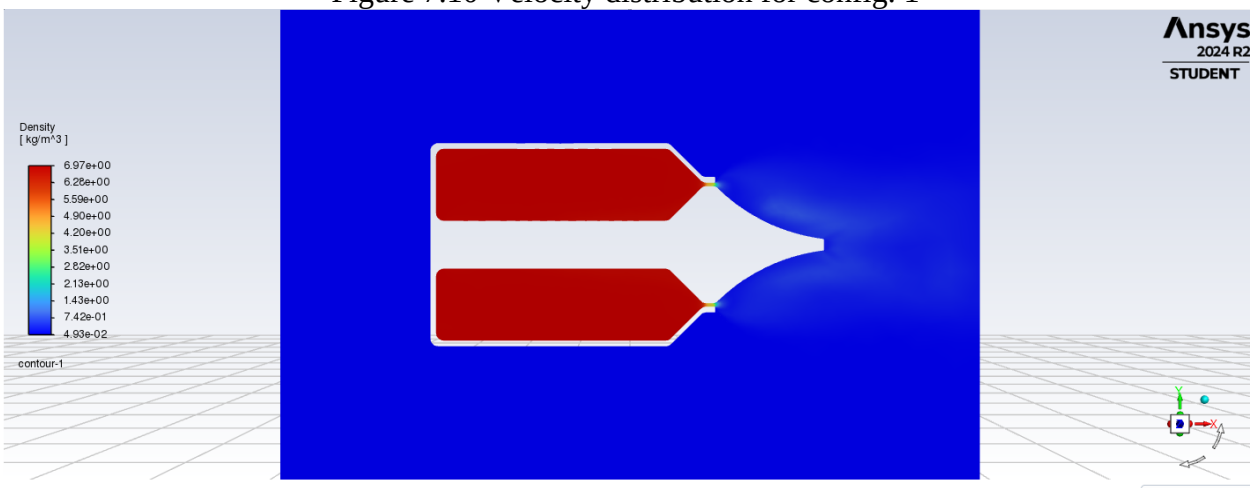

Figure 7.11 Density distribution for config. 1

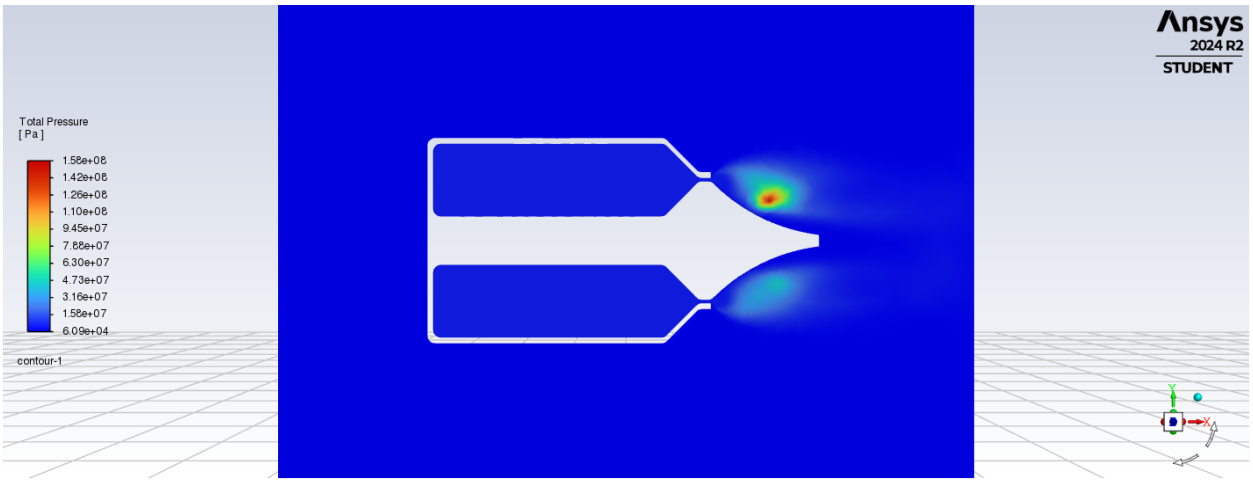

Figure 7.12 Total pressure distribution for config. 1

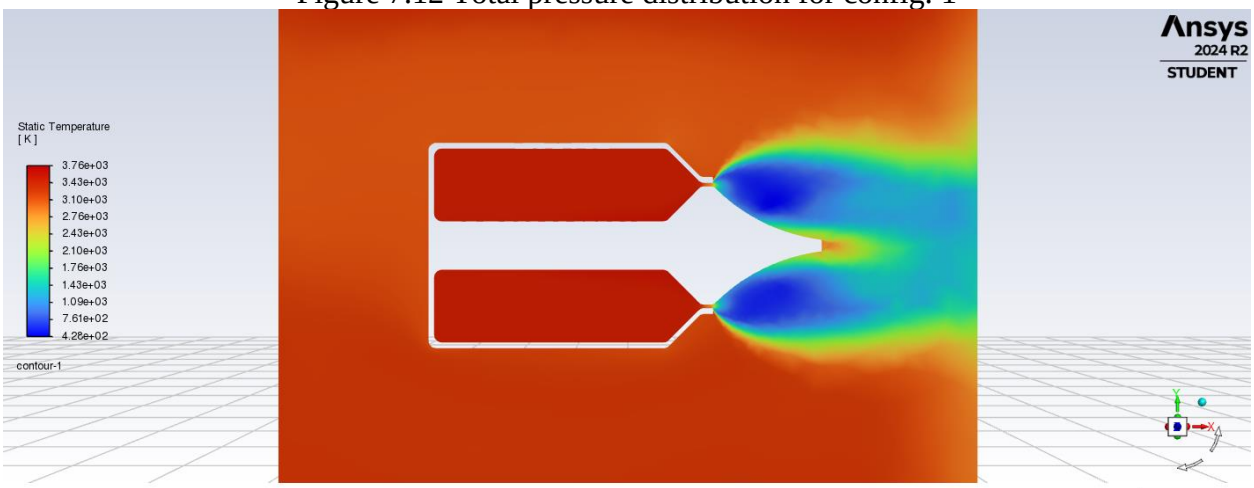

Figure 7.13 Static temperature distribution for config. 1

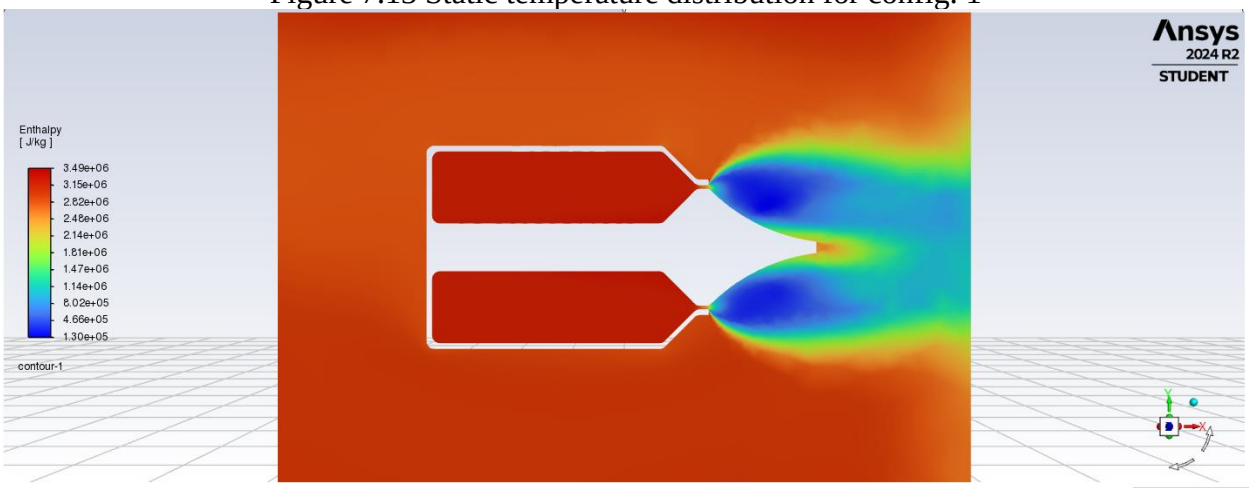

Figure 7.14 Enthalpy distribution for config. 1

7.4.2 Configuration 1 results at 81235 Pa

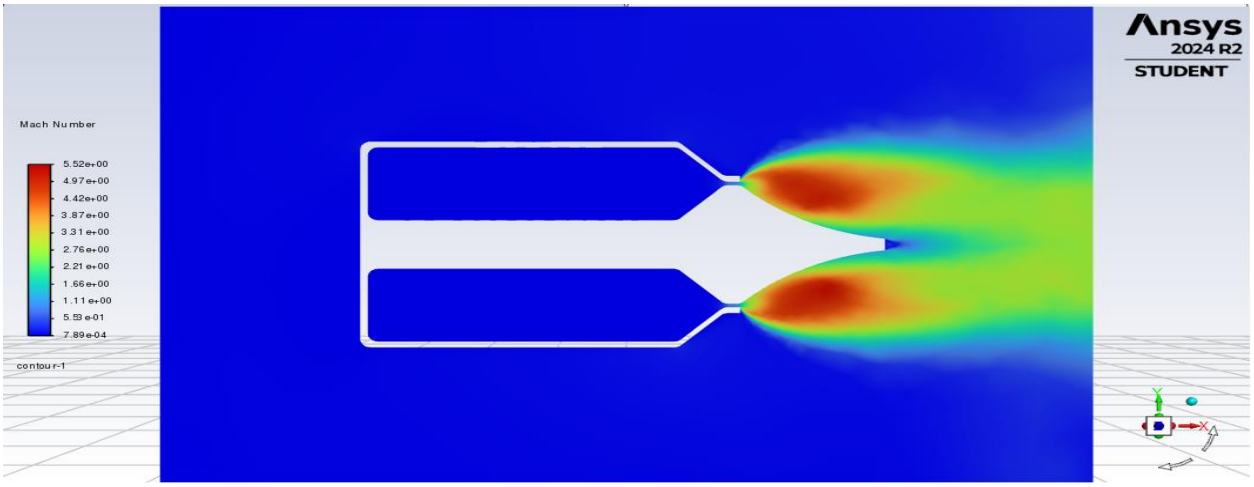

Figure 7.15 Mach distribution for config. 1

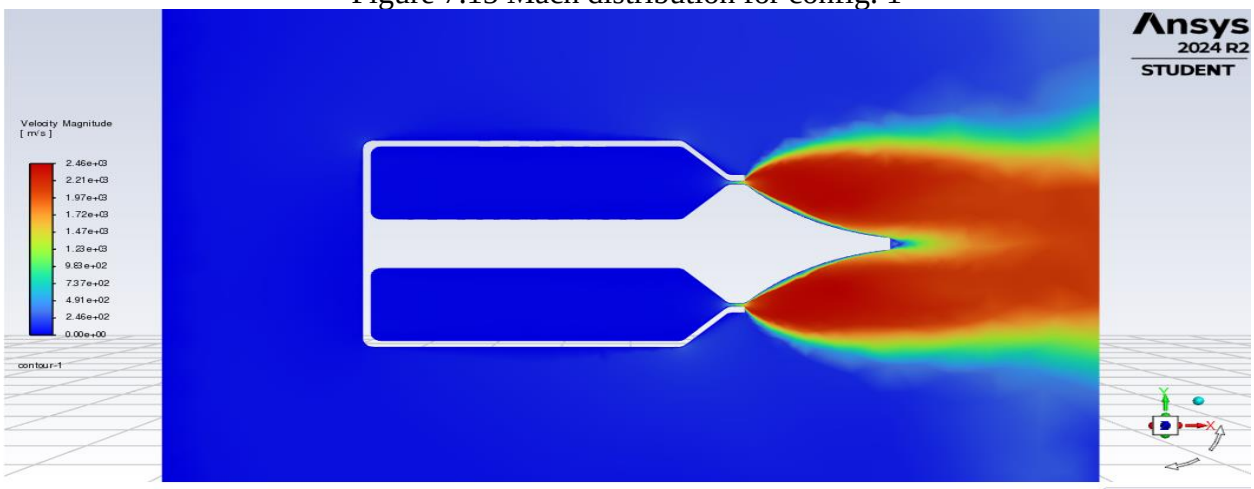

Figure 7.16 Velocity distribution for config. 1

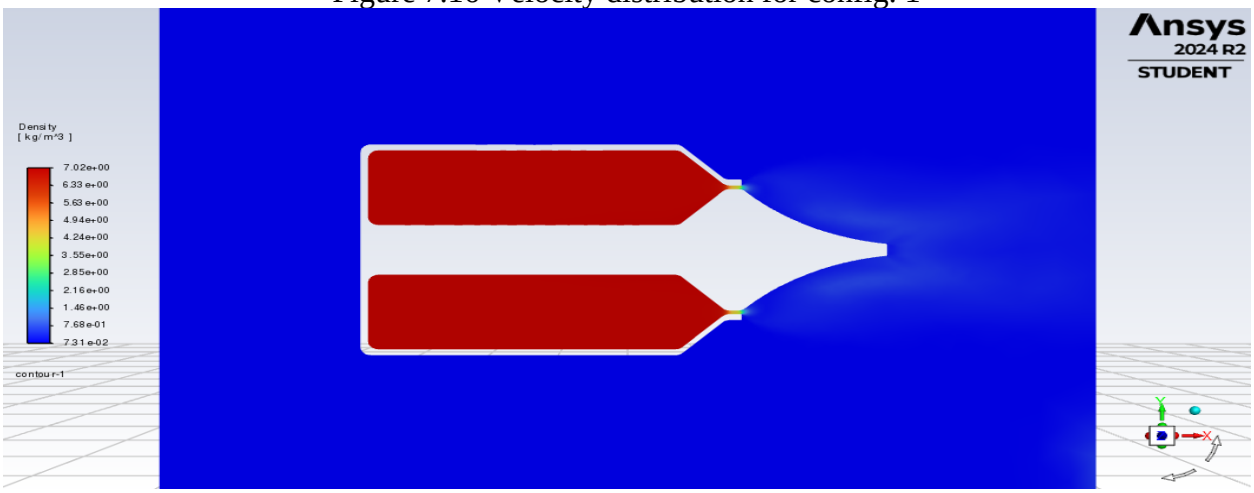

Figure 7.17 Density distribution for config. 1

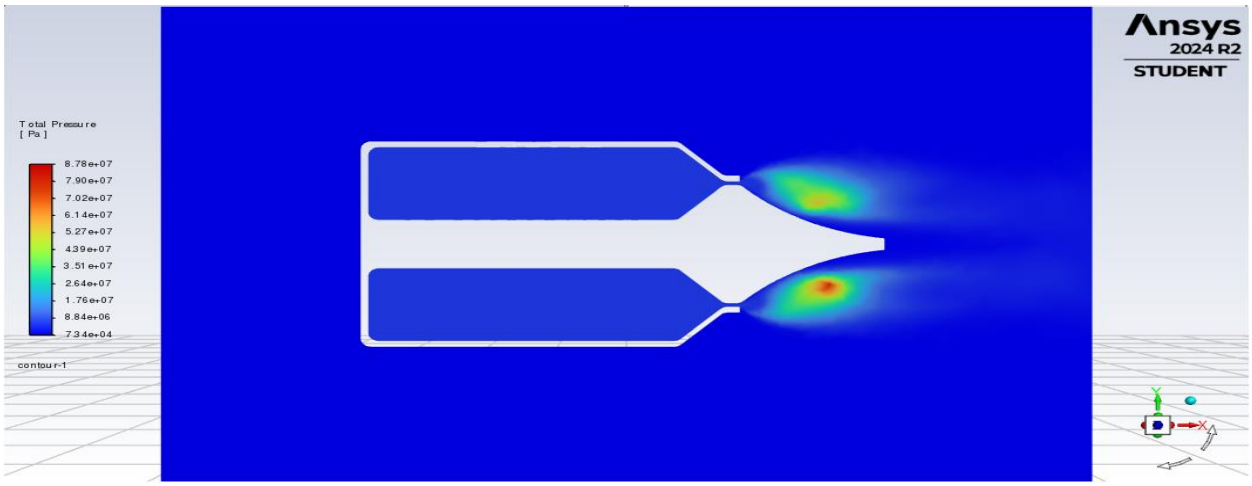

Figure 7.18 Total pressure distribution for config. 1

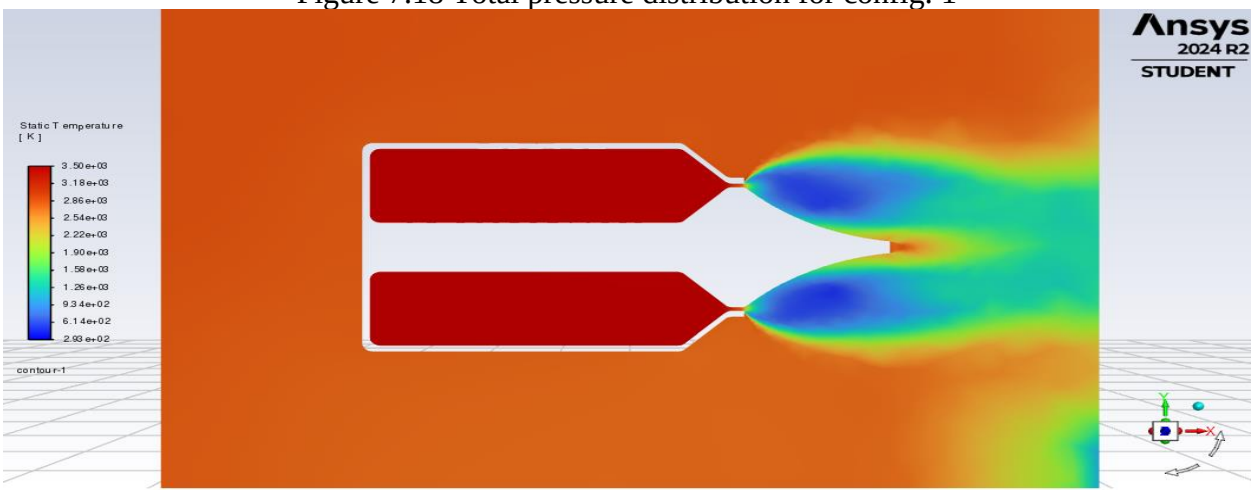

Figure 7.19 Static temperature distribution for config. 1

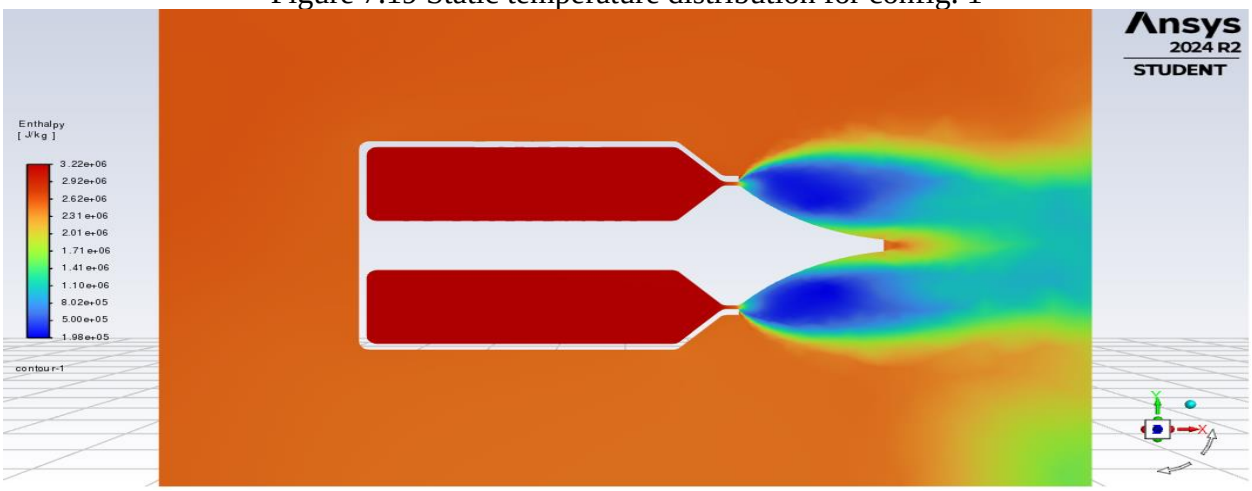

Figure 7.120 Enthalpy distribution for config. 1

7.4.3 Configuration 1 results at 101235 Pa

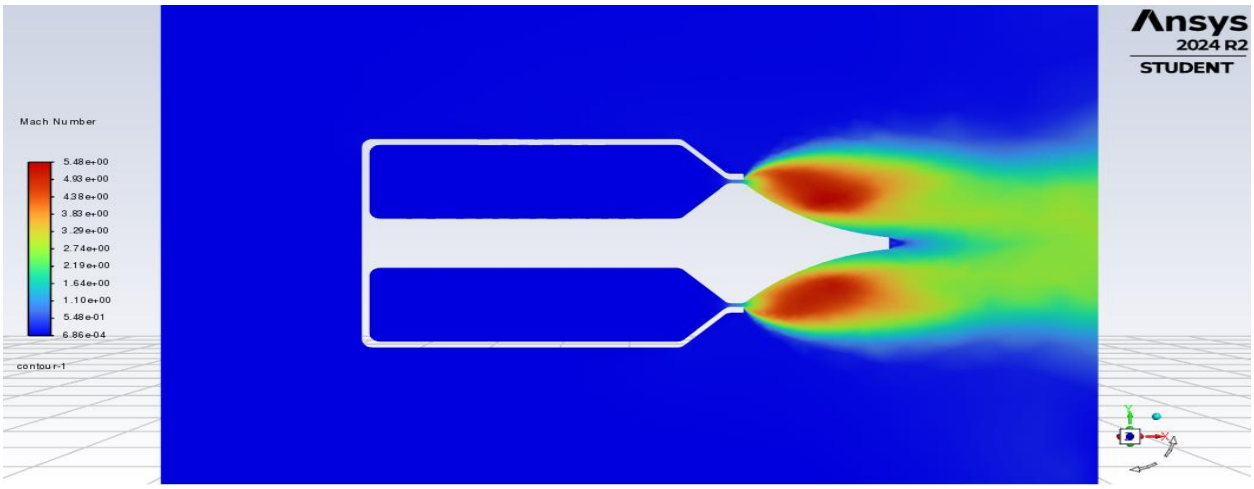

Figure 7.21 Mach distribution for config. 1

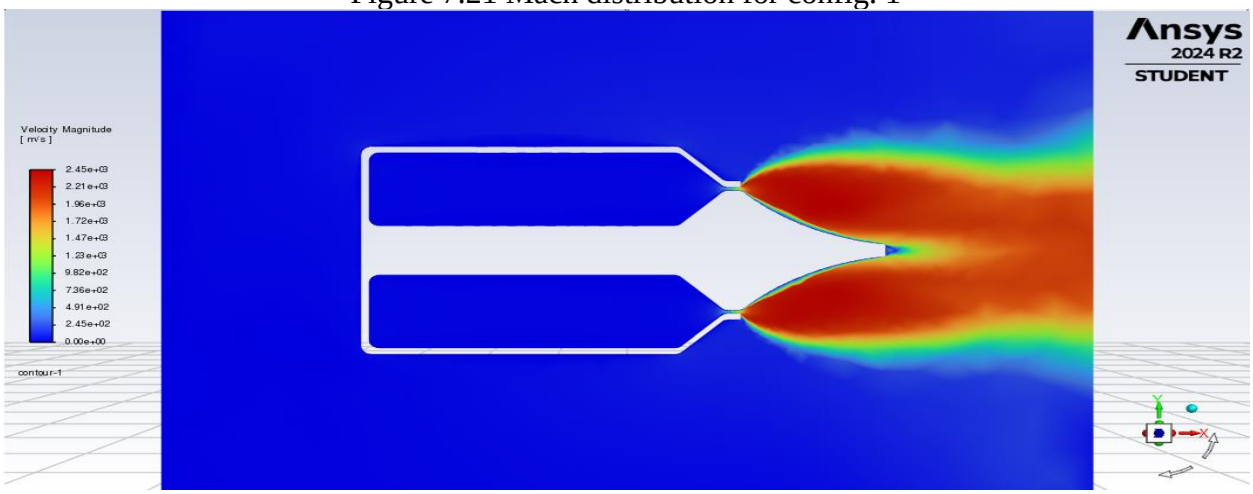

Figure 7.22 Velocity distribution for config. 1

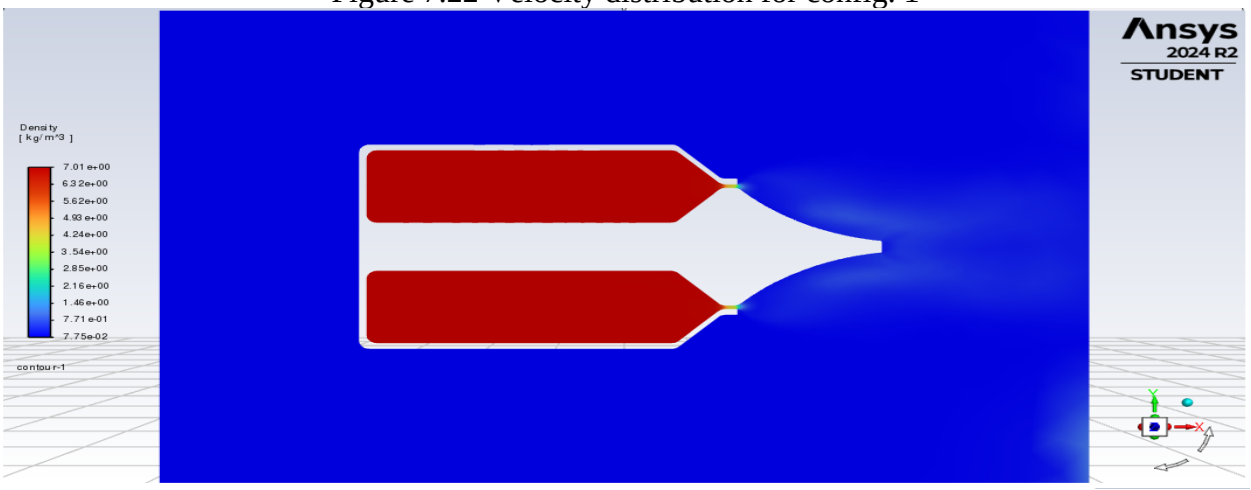

Figure 7.23 Density distribution for config. 1

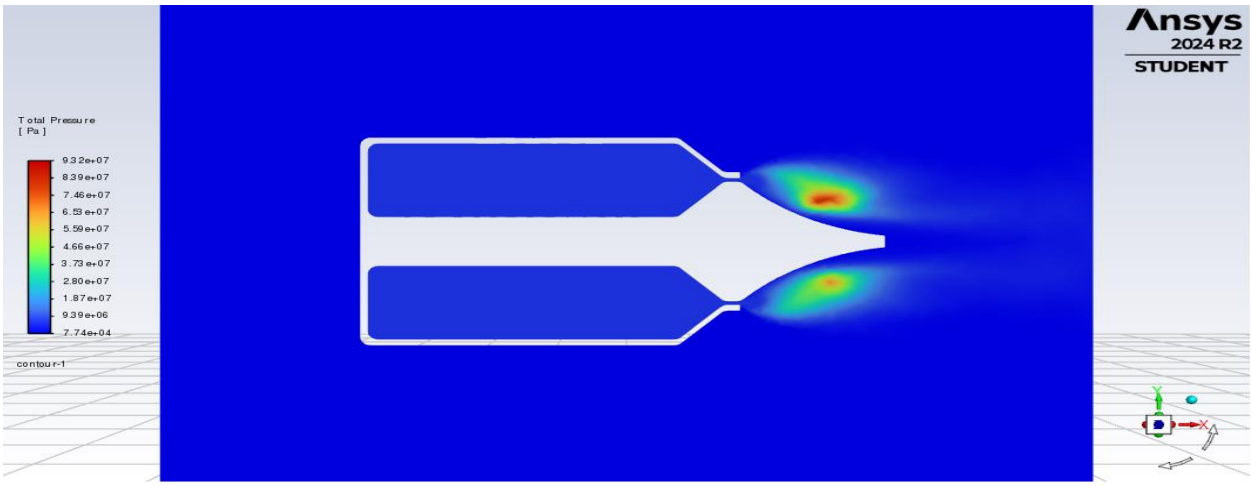

Figure 7.24 Total pressure distribution for config. 1

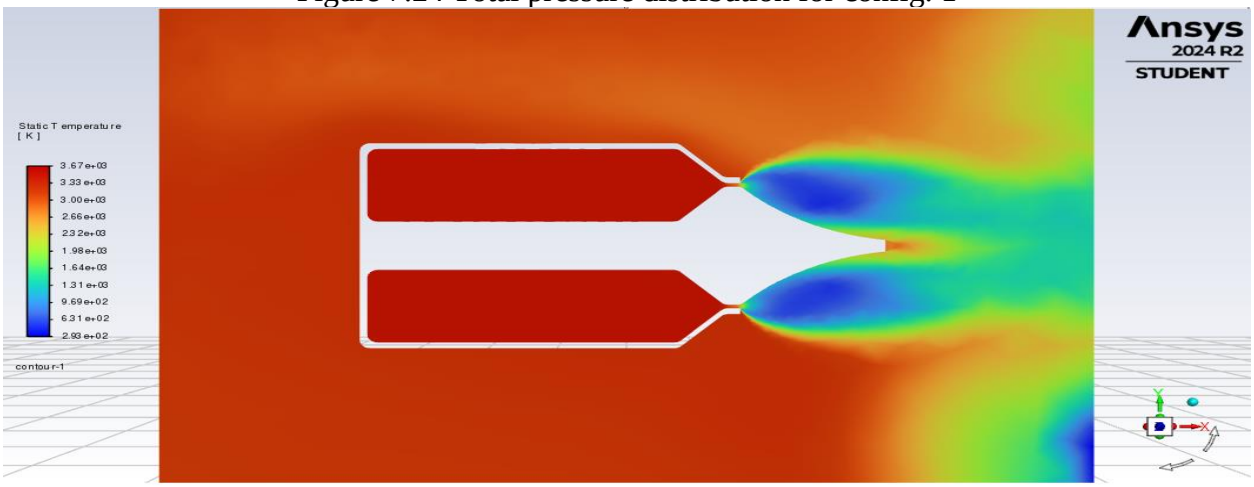

Figure 7.25 Static temperature distribution for config. 1

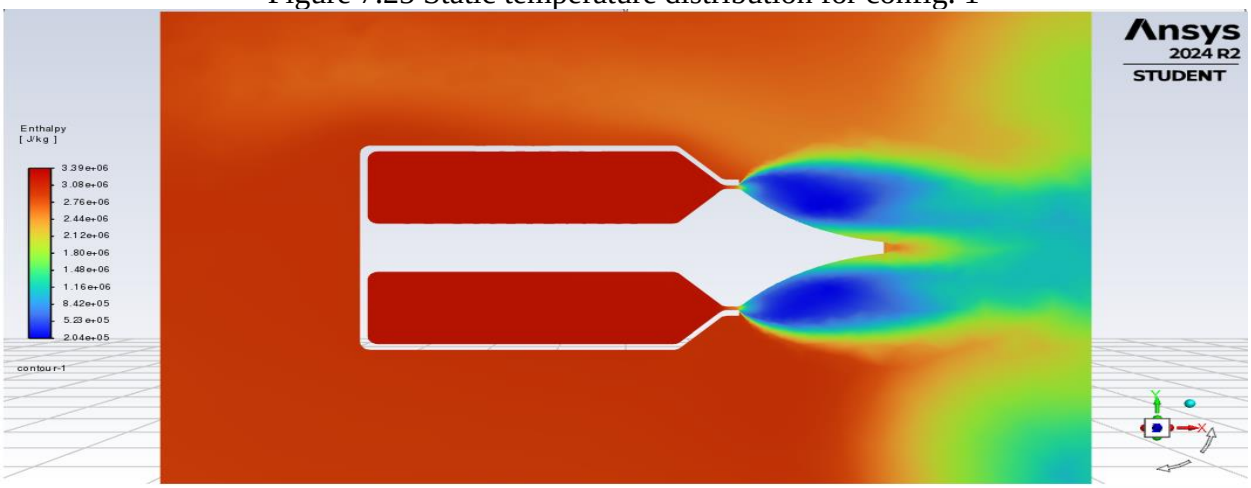

Figure 7.26 Enthalpy distribution for config. 1

7.4.4 Configuration 2 results at 51235 Pa

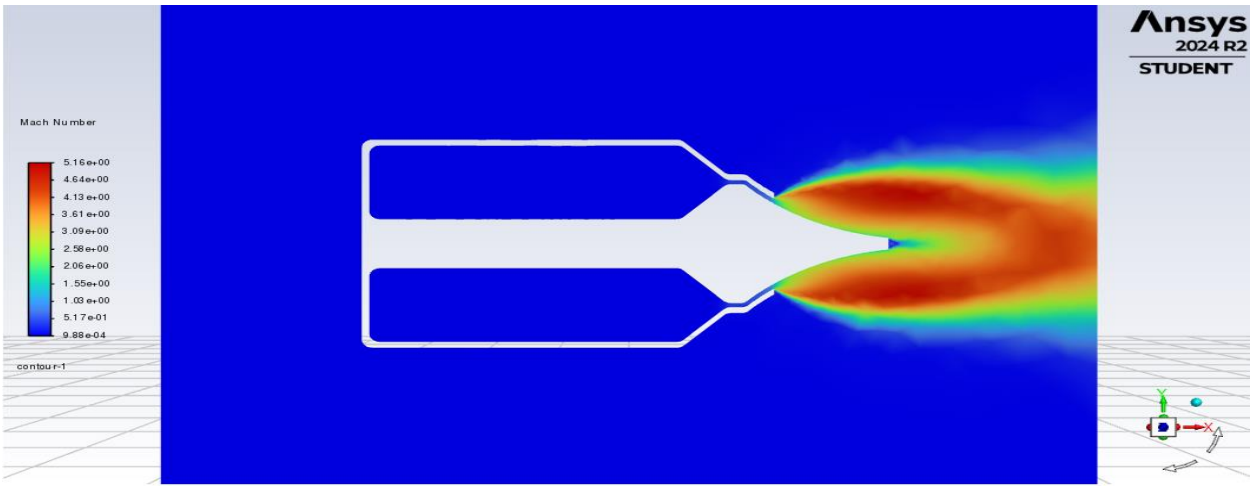

Figure 7.27 Mach distribution for config. 2

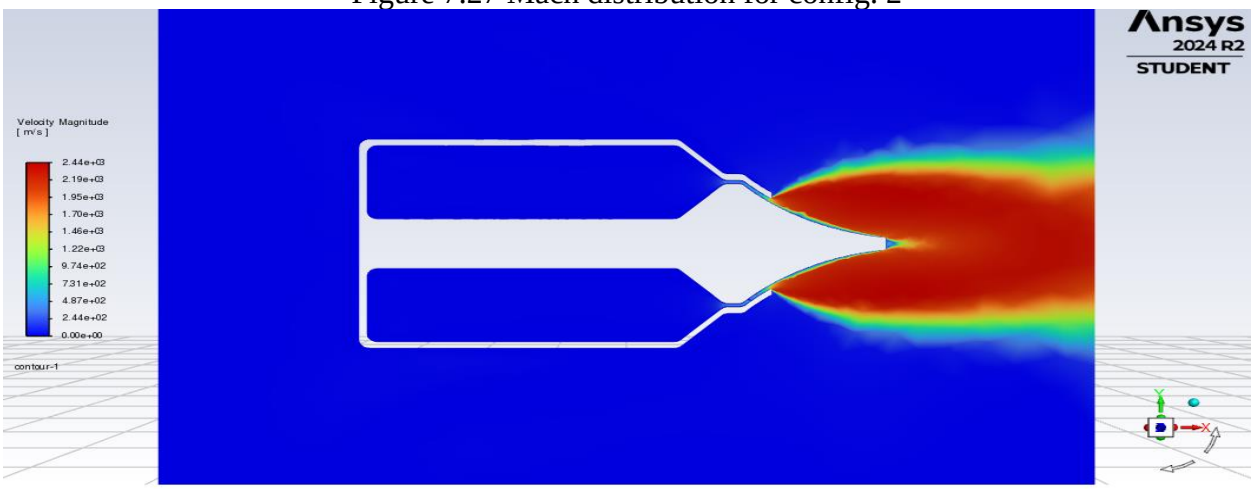

Figure 7.28 Velocity distribution for config. 2

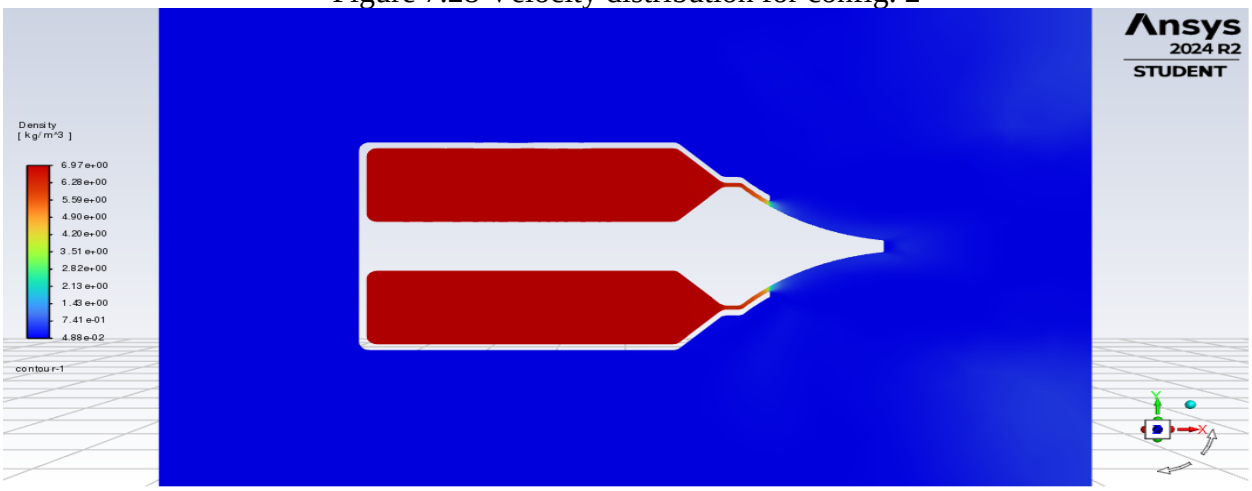

Figure 7.29 Density distribution for config. 2

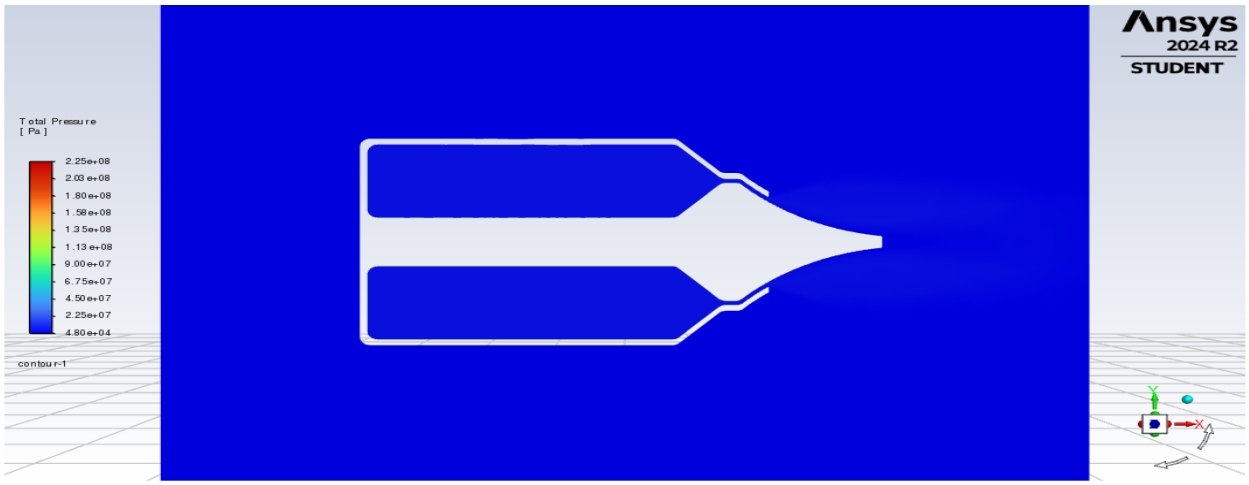

Figure 7.30 Total pressure distribution for config. 2

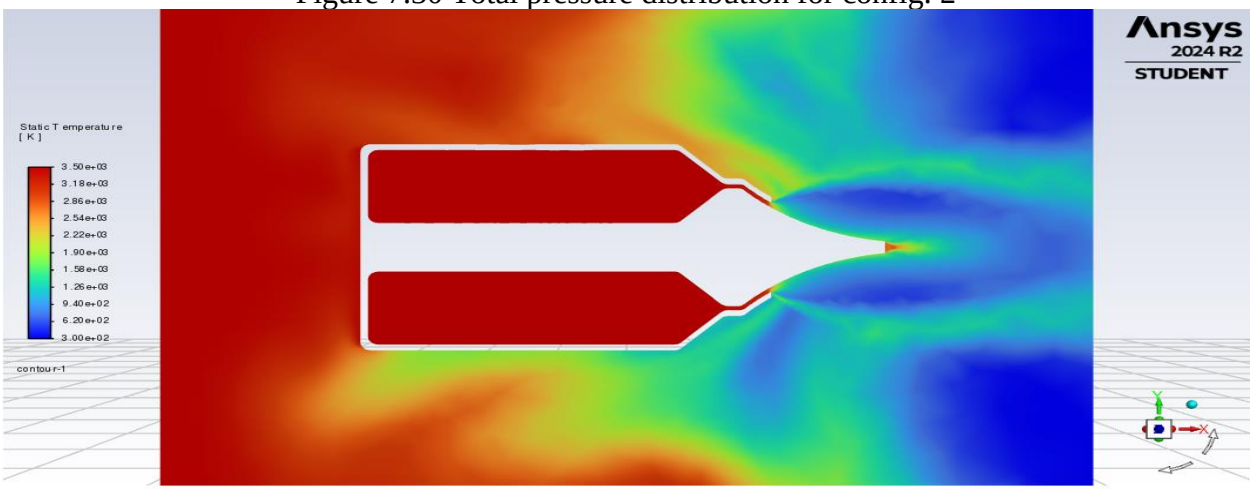

Figure 7.31 Static temperature distribution for config. 2

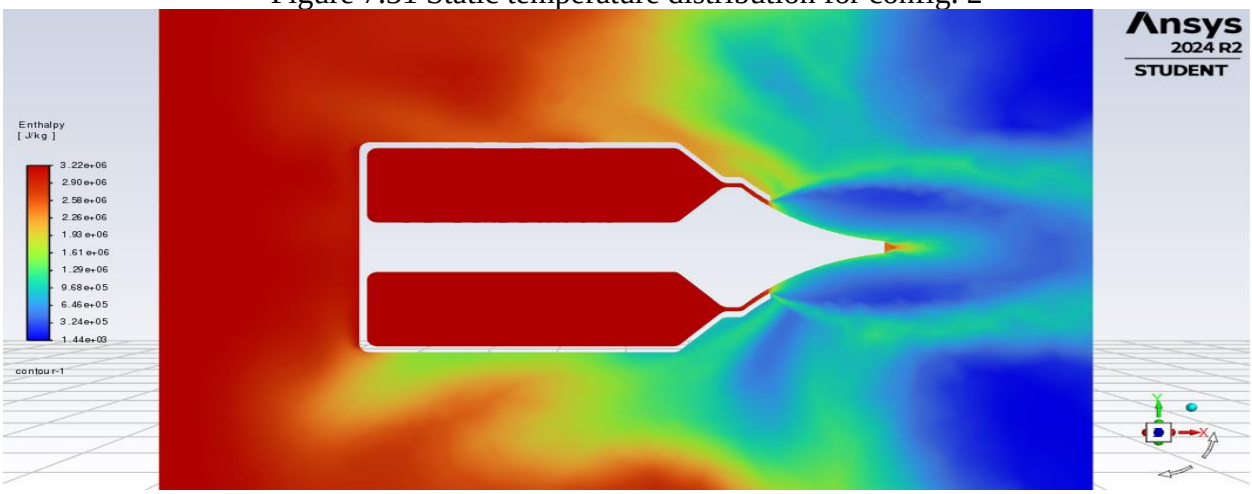

Figure 7.32 Enthalpy distribution for config. 2

7.4.5 Configuration 2 results at 81235 Pa

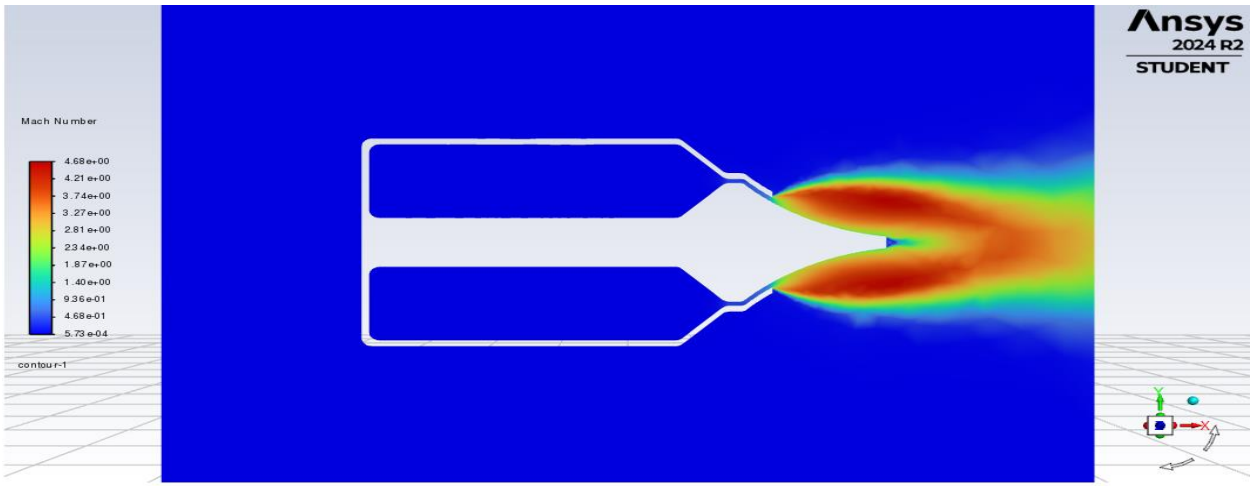

Figure 7.23 Mach distribution for config. 2

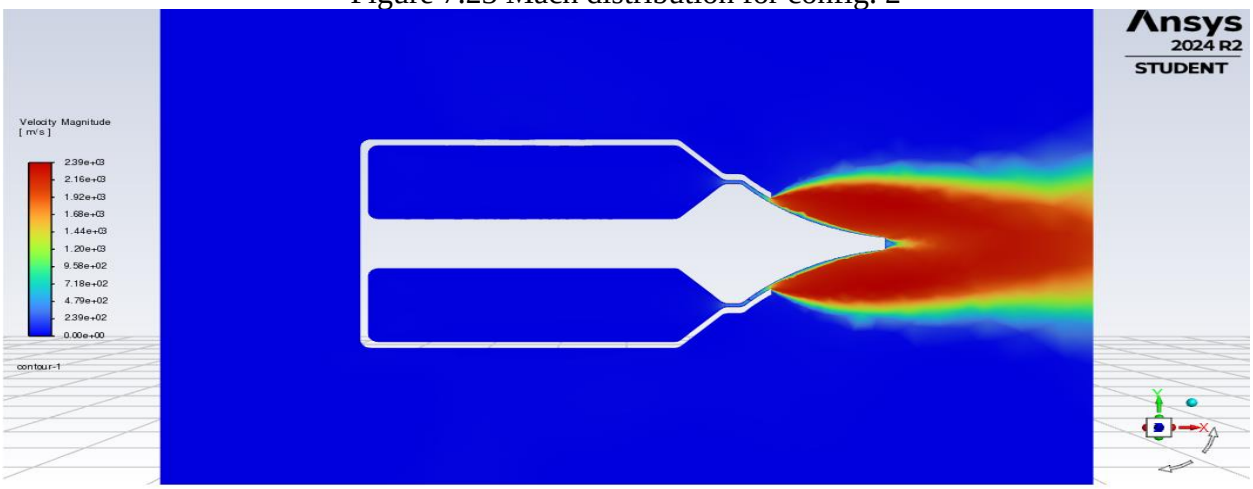

Figure 7.34 Velocity distribution for config. 2

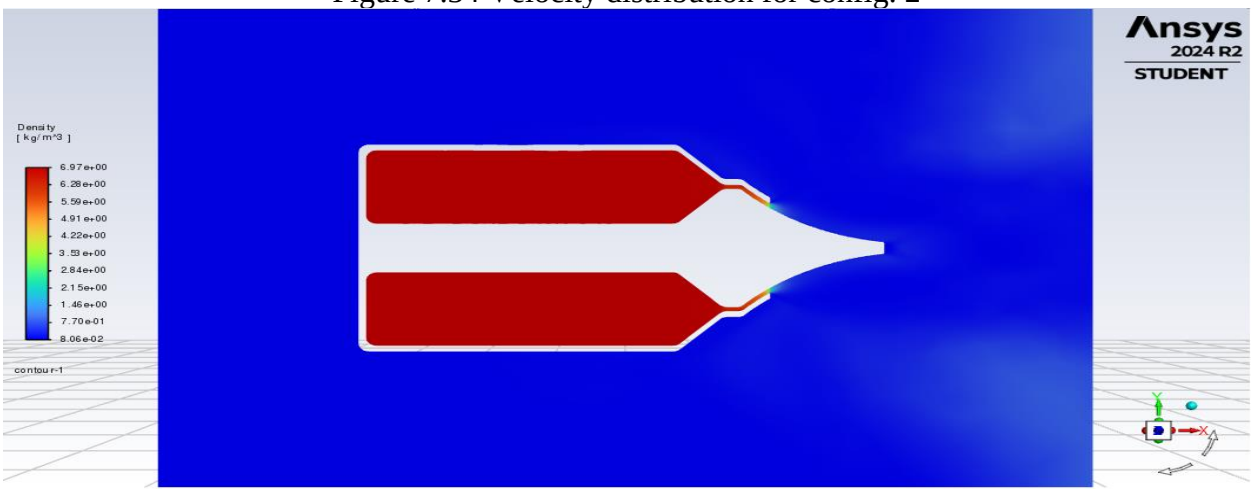

Figure 7.35 Density distribution for config. 2

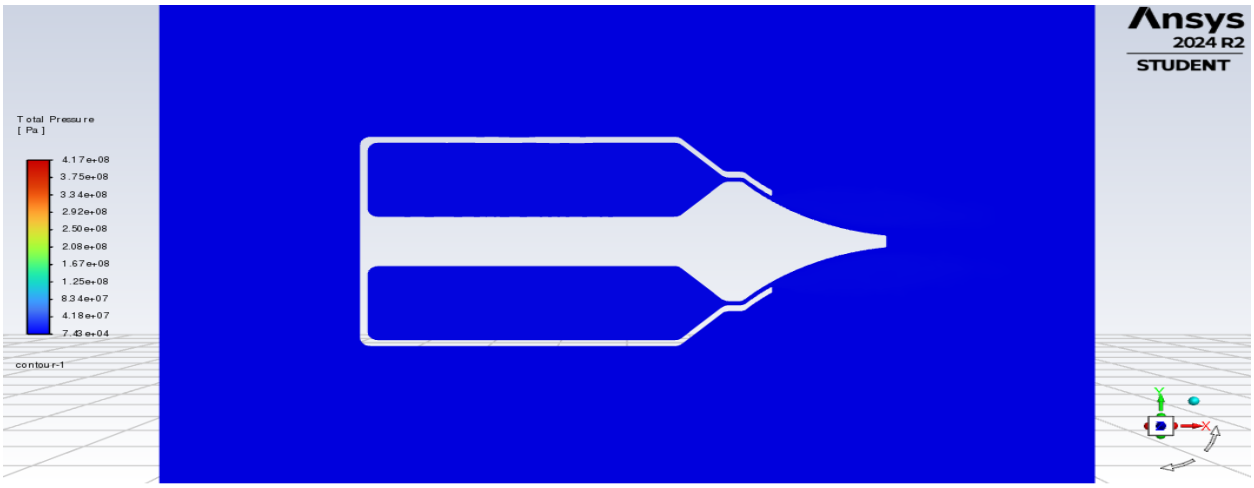

Figure 7.36 Total pressure distribution for config. 2

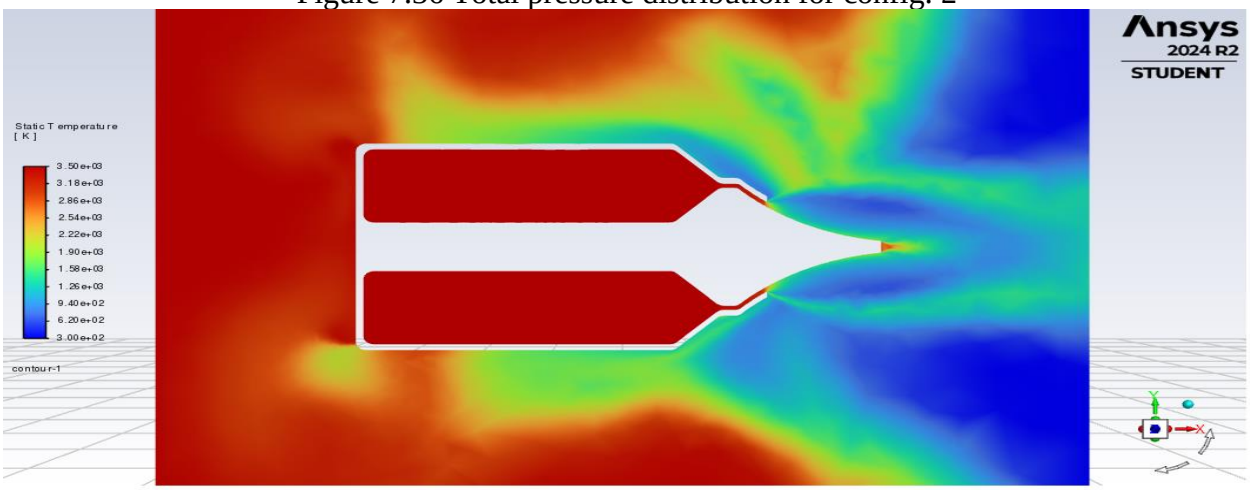

Figure 7.37 Static temperature distribution for config. 2

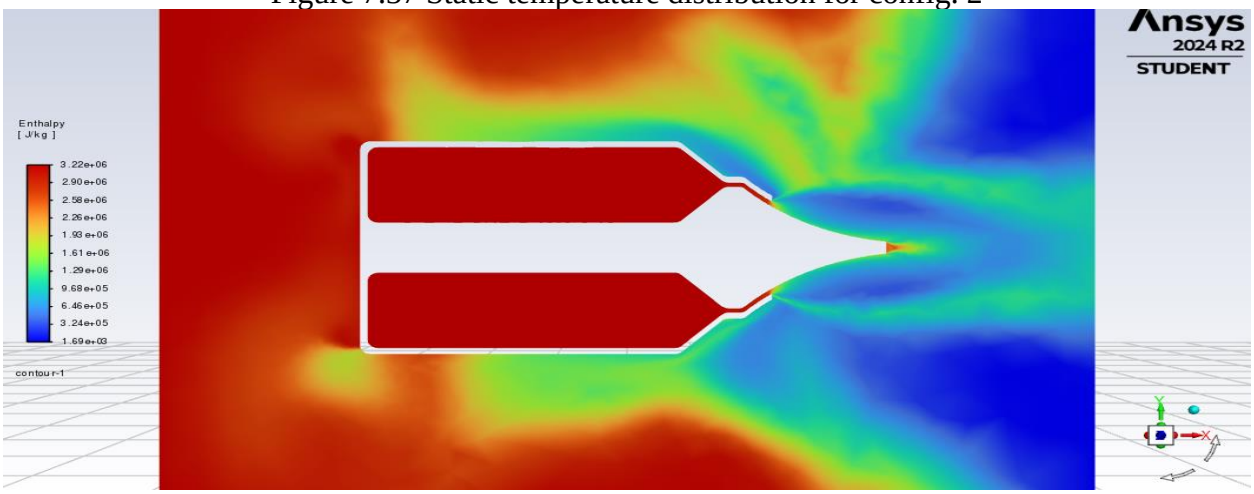

Figure 7.38 Enthalpy distribution for config. 2

7.4.6 Configuration 2 results at 101235 Pa

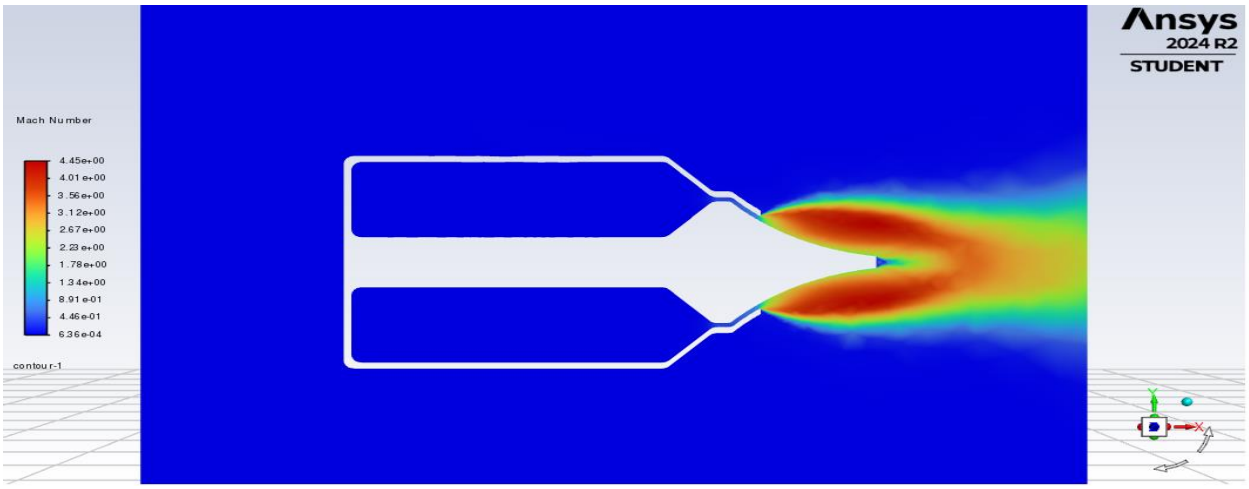

Figure 7.39 Mach distribution for config. 2

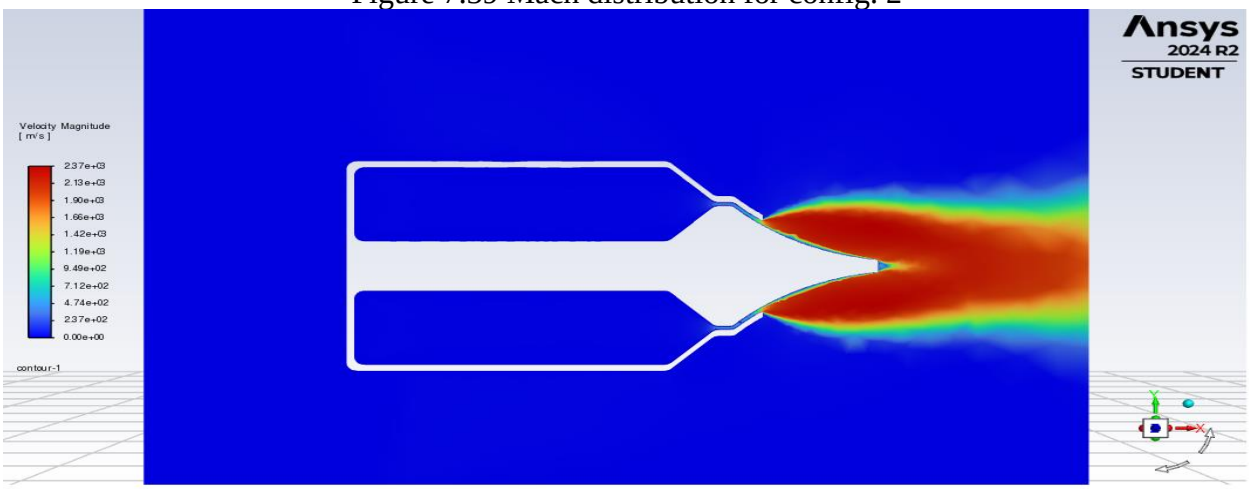

Figure 7.40 Velocity distribution for config. 2

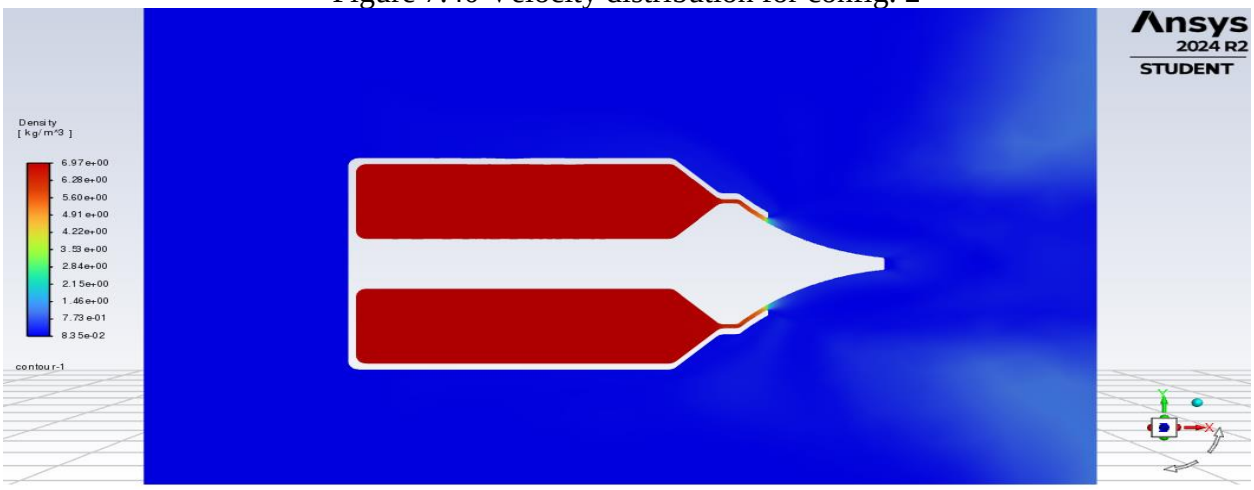

Figure 7.41 Density distribution for config. 2

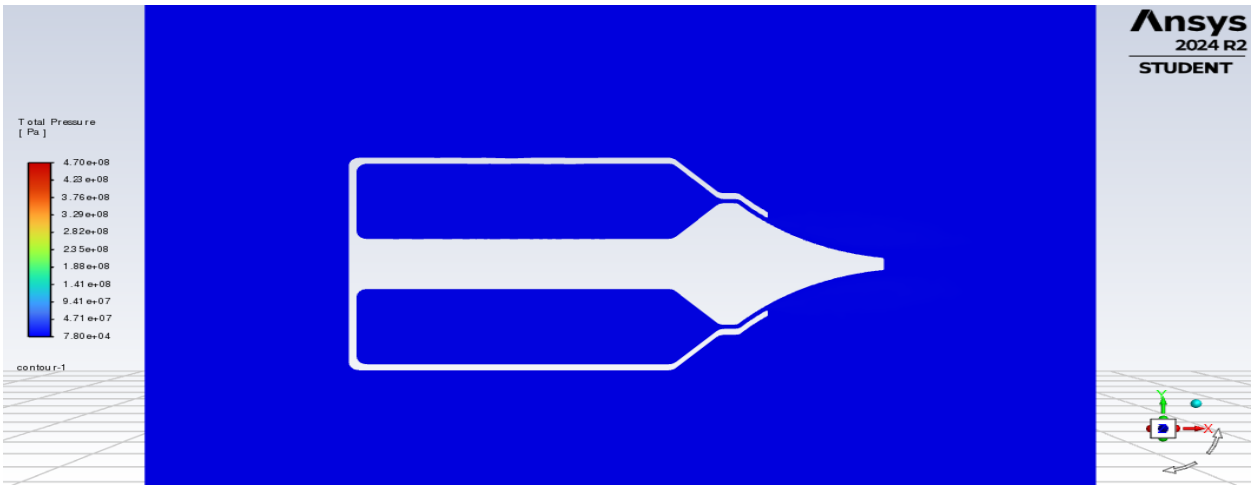

Figure 7.42 Total pressure distribution for config. 2

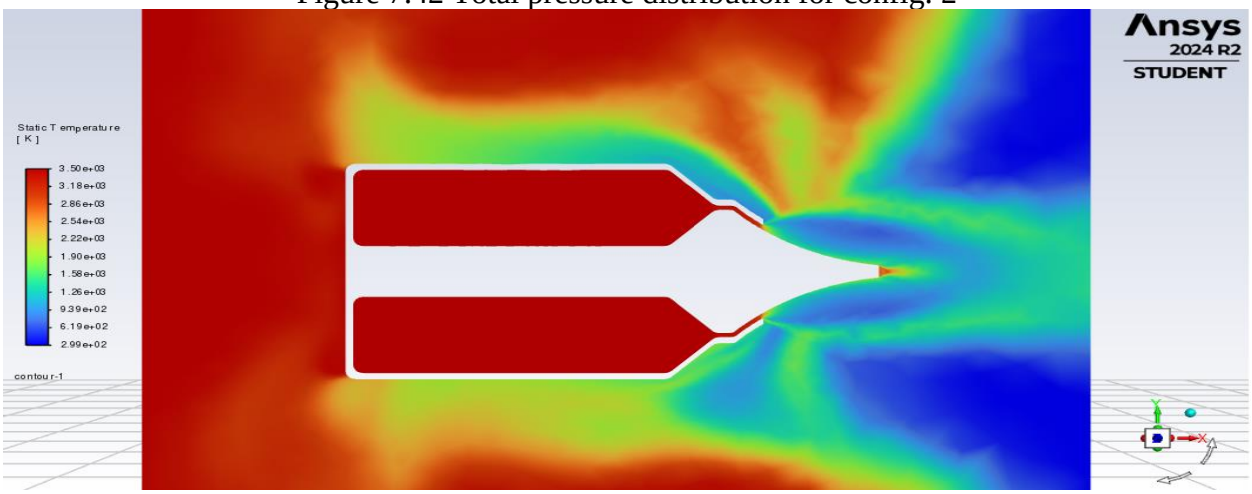

Figure 7.43 Static temperature distribution for config. 2

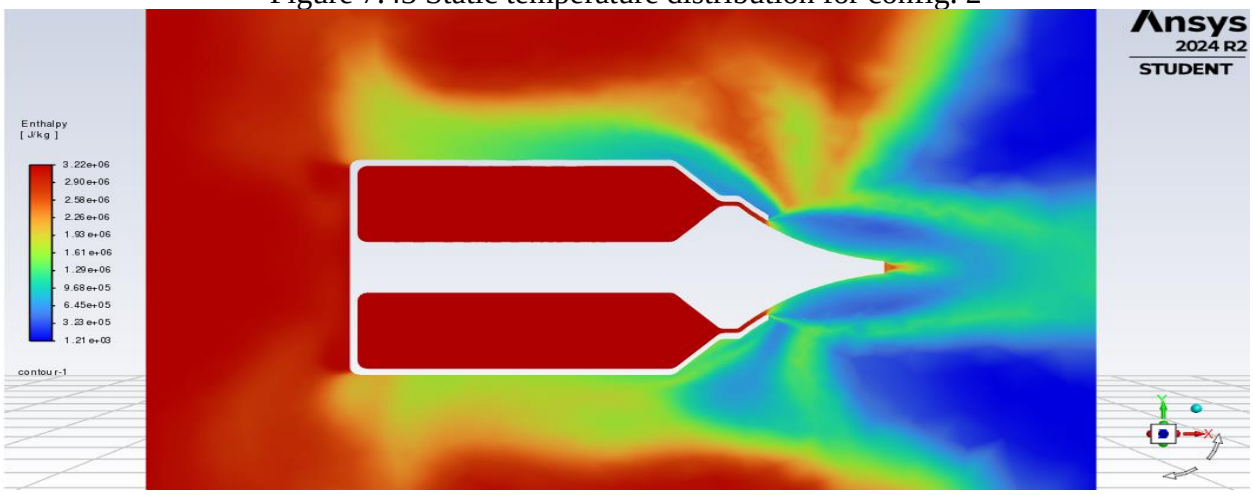

Figure 7.44 Enthalpy distribution for config. 2

7.4.7 Configuration 3 results at 51235 Pa

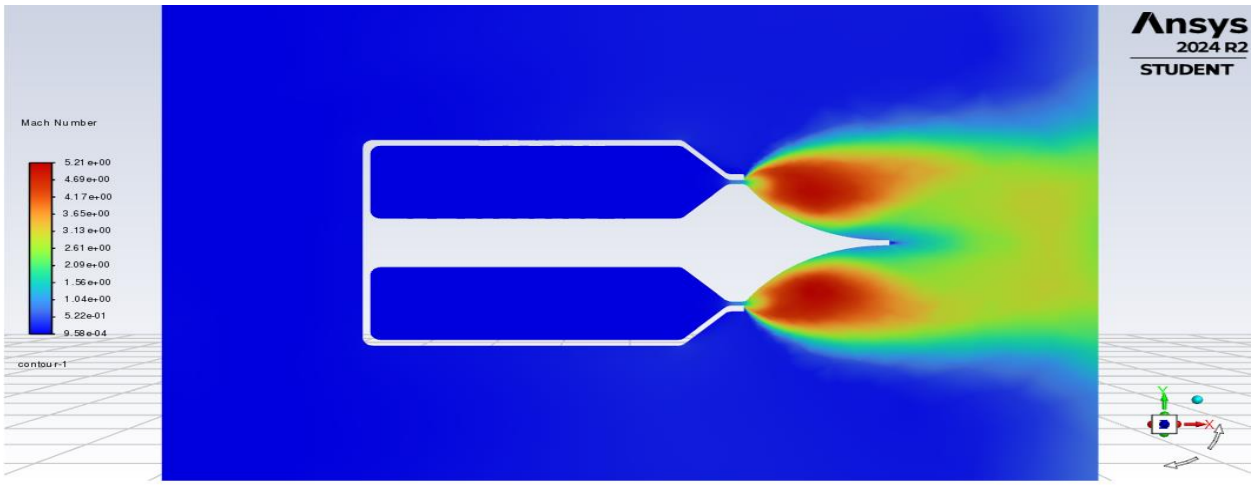

Figure 7.45 Mach distribution for config. 3

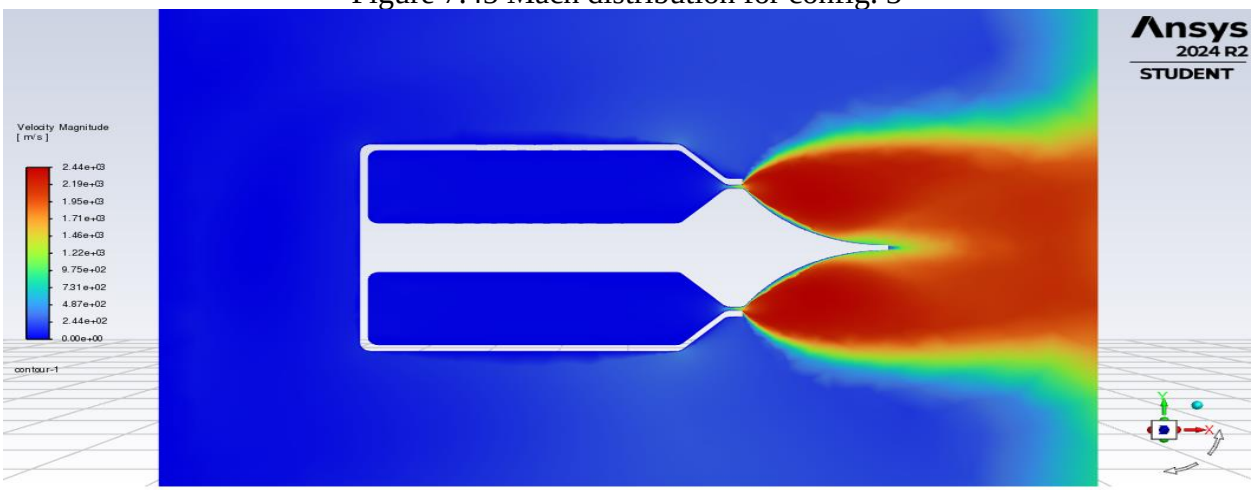

Figure 7.46 Velocity distribution for config. 3

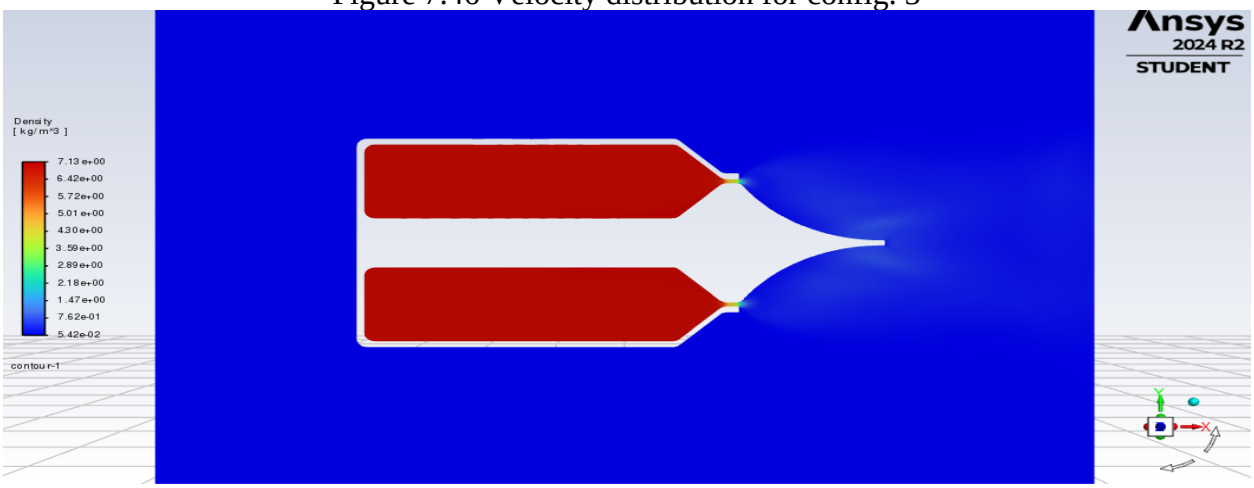

Figure 7.47 Density distribution for config. 3

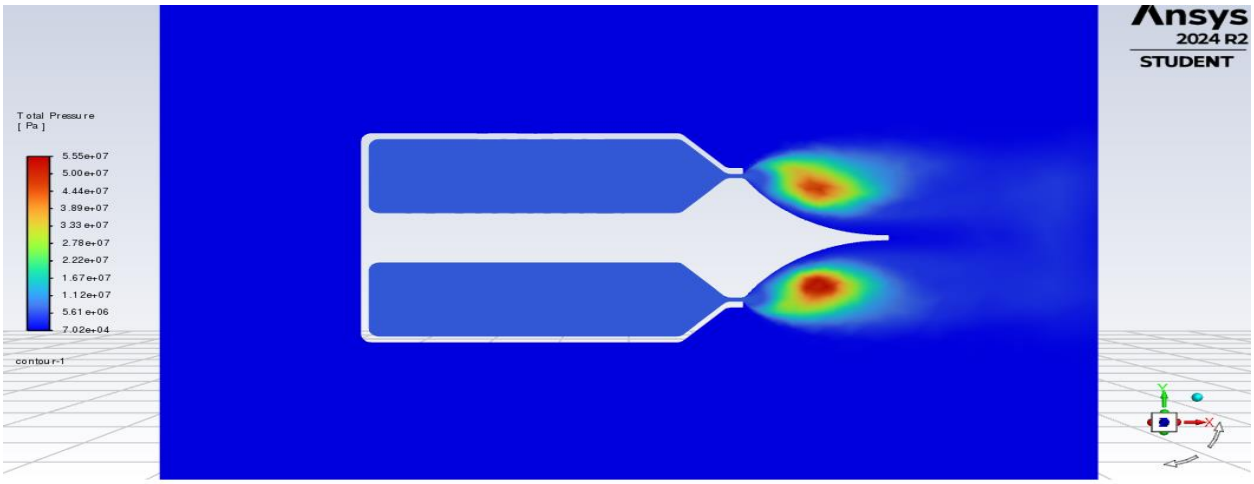

Figure 7.48 Total pressure distribution for config. 3

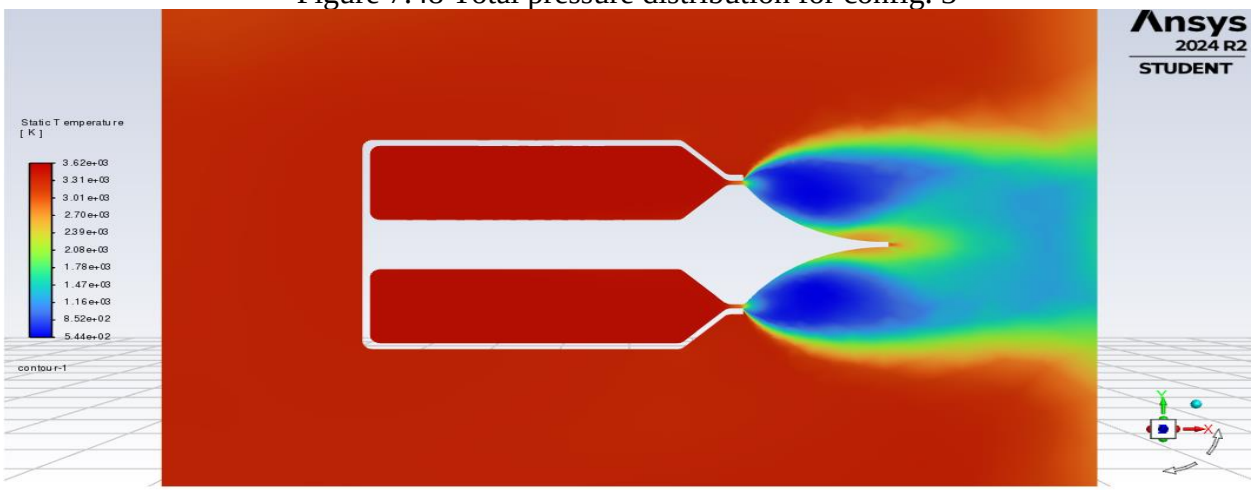

Figure 7.49 Static temperature distribution for config. 3

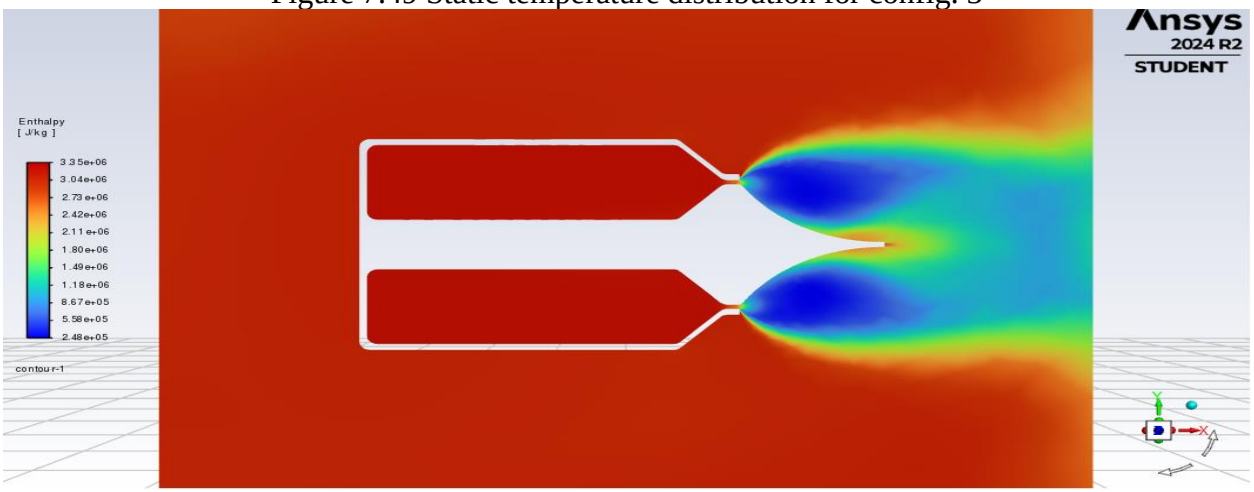

Figure 7.50 Enthalpy distribution for config. 3

7.4.8 Configuration 3 results at 81235 Pa

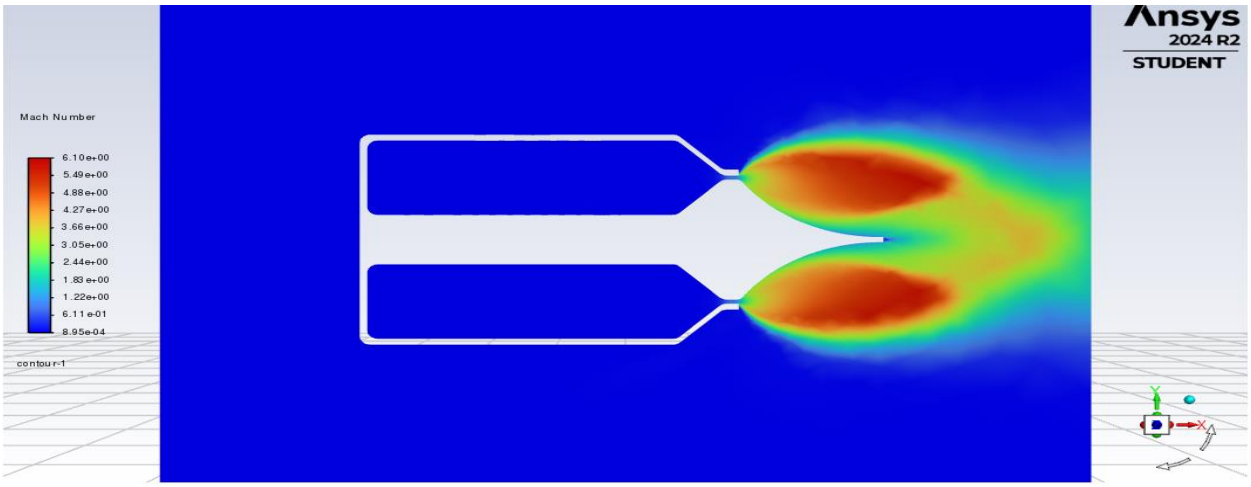

Figure 7.51 Mach distribution for config. 3

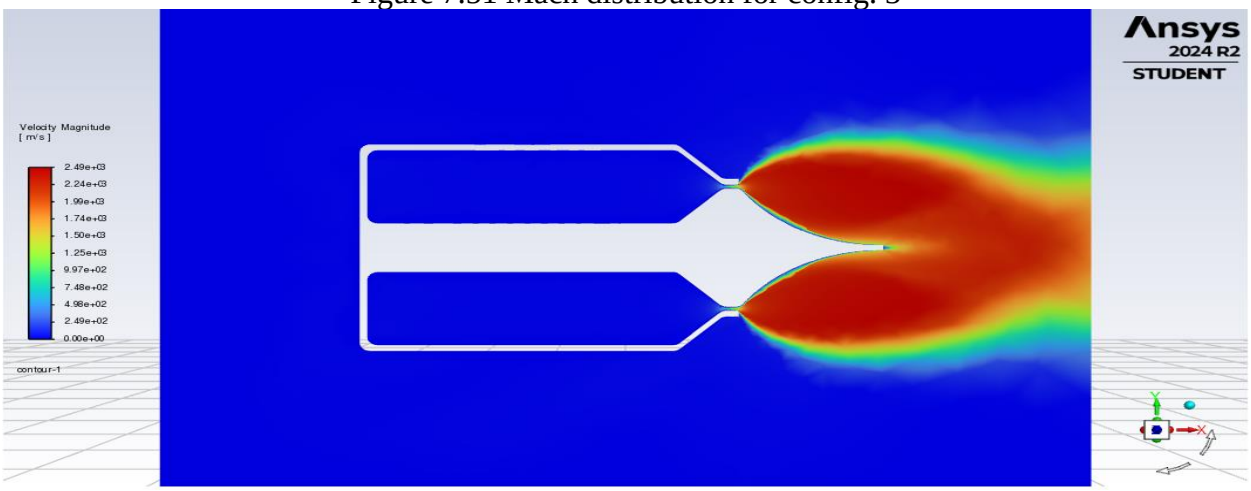

Figure 7.52 Velocity distribution for config. 3

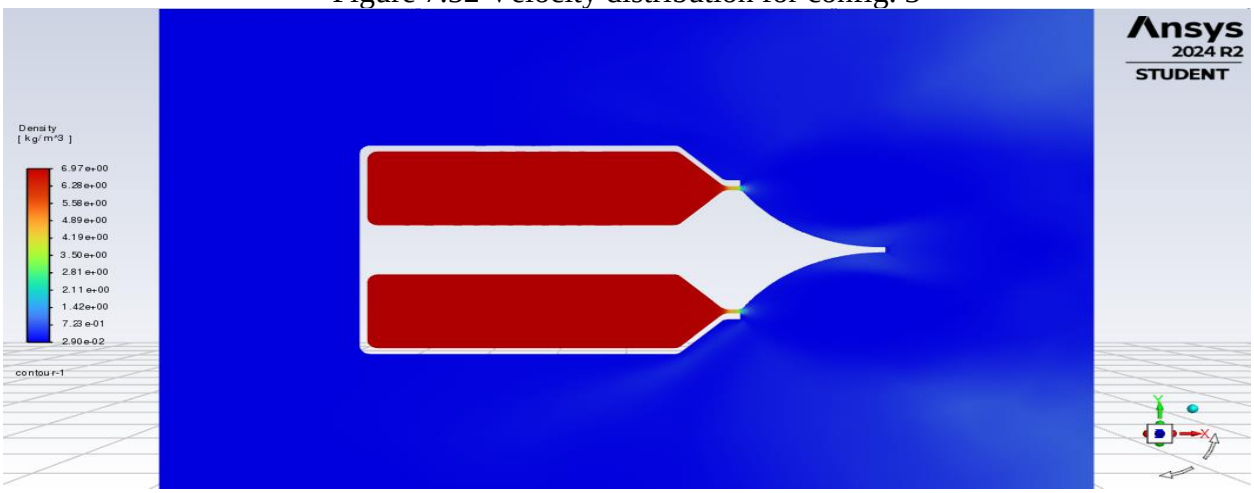

Figure 7.53 Density distribution for config. 3

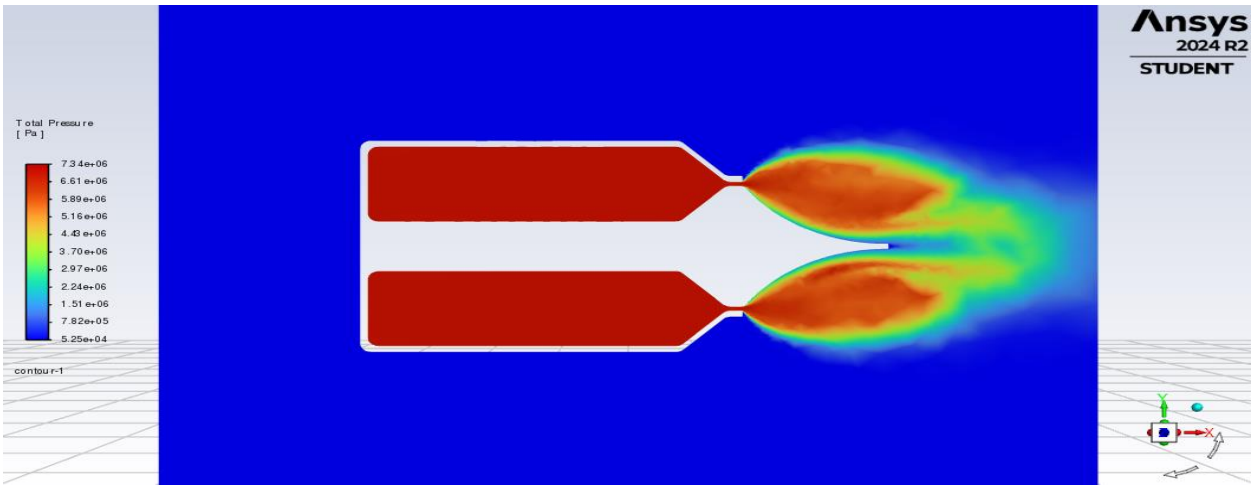

Figure 7.54 Total pressure distribution for config. 3

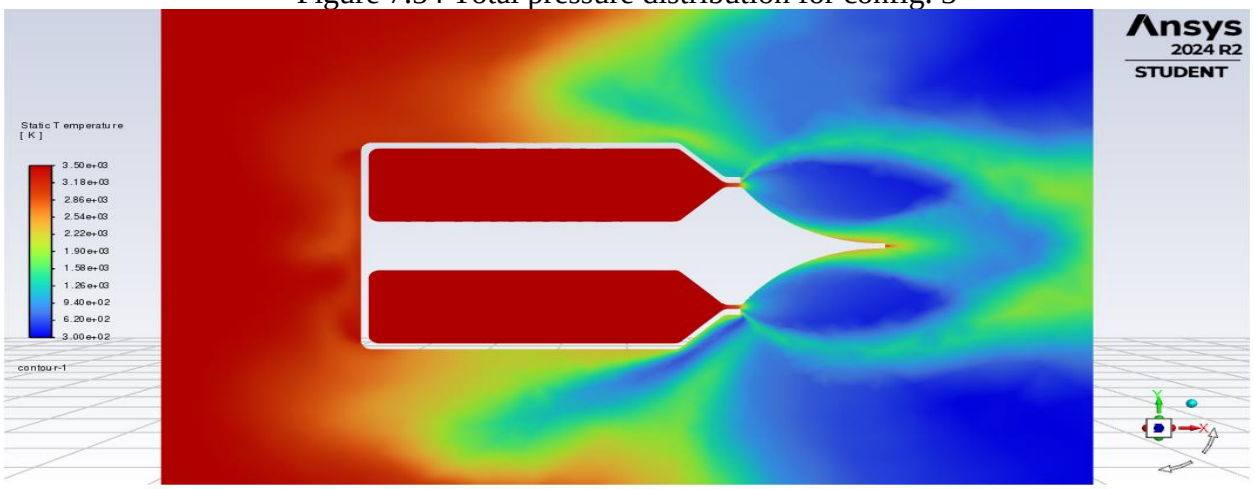

Figure 7.55 Static temperature distribution for config. 3

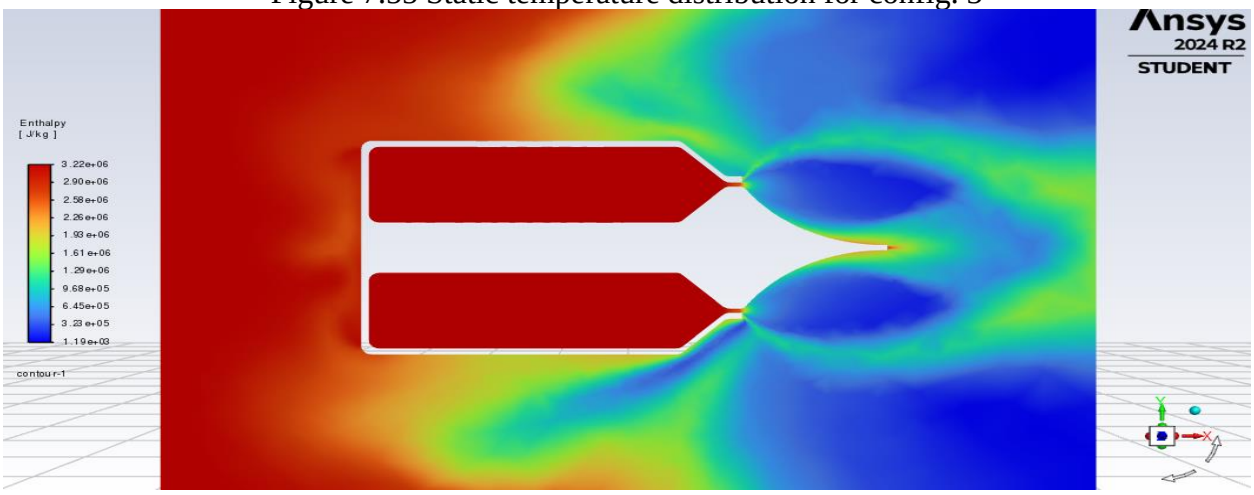

Figure 7.56 Enthalpy distribution for config. 3

7.4.9 Configuration 3 results at 101235 Pa

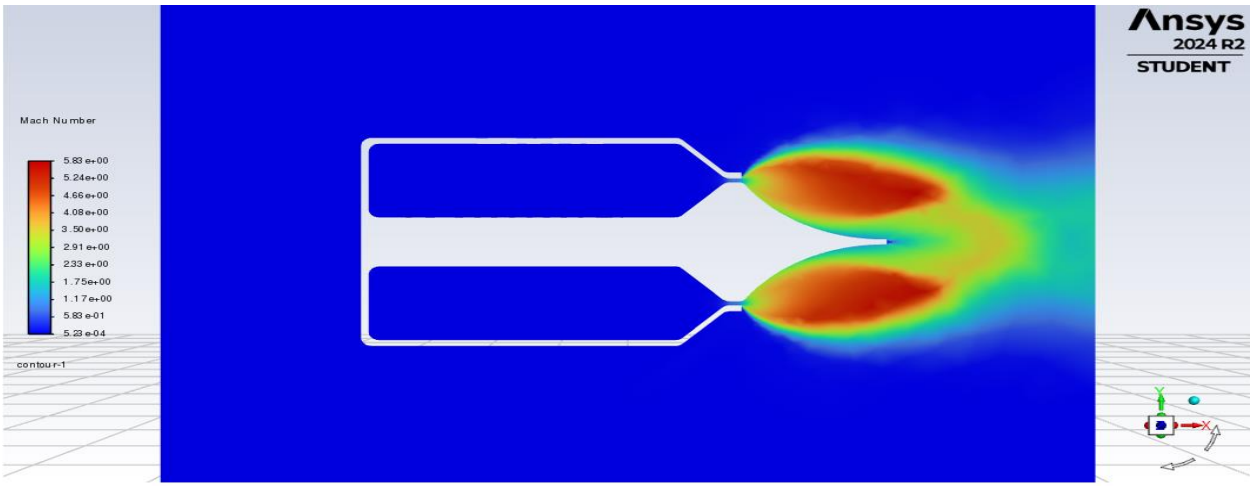

Figure 7.57 Mach distribution for config. 3

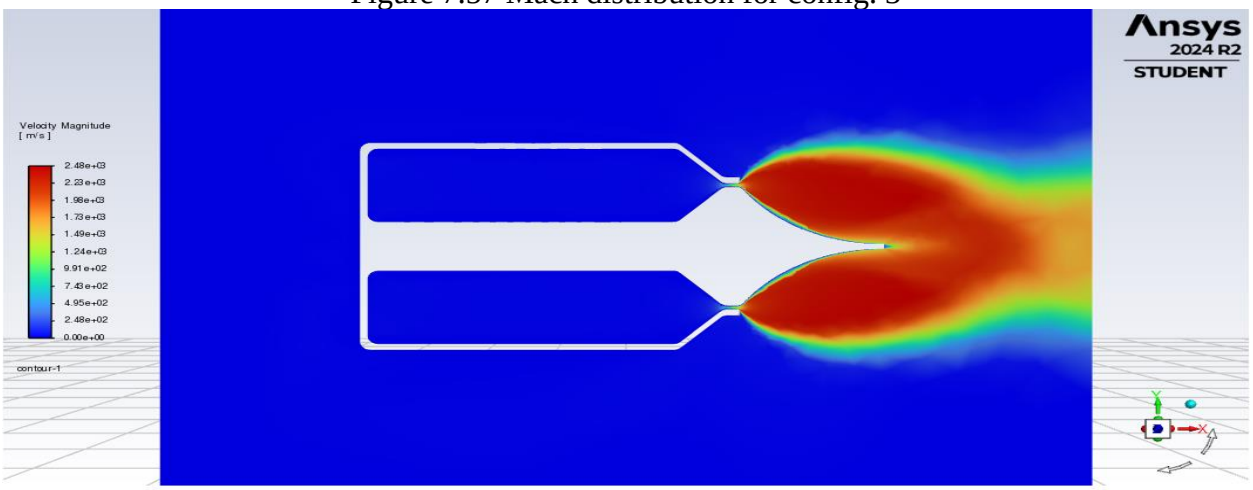

Figure 7.58 Velocity distribution for config. 3

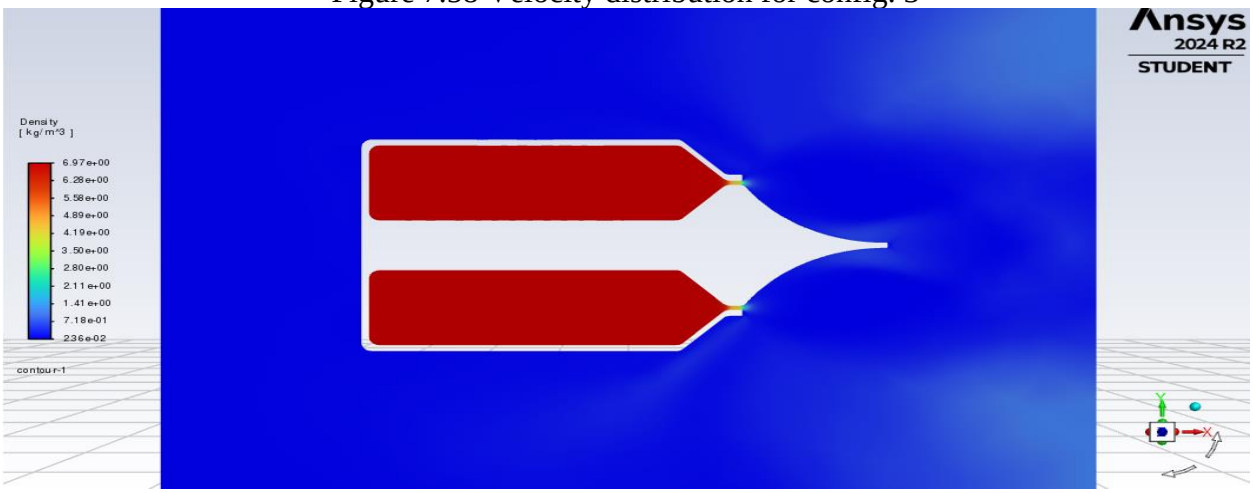

Figure 7.59 Density distribution for config. 3

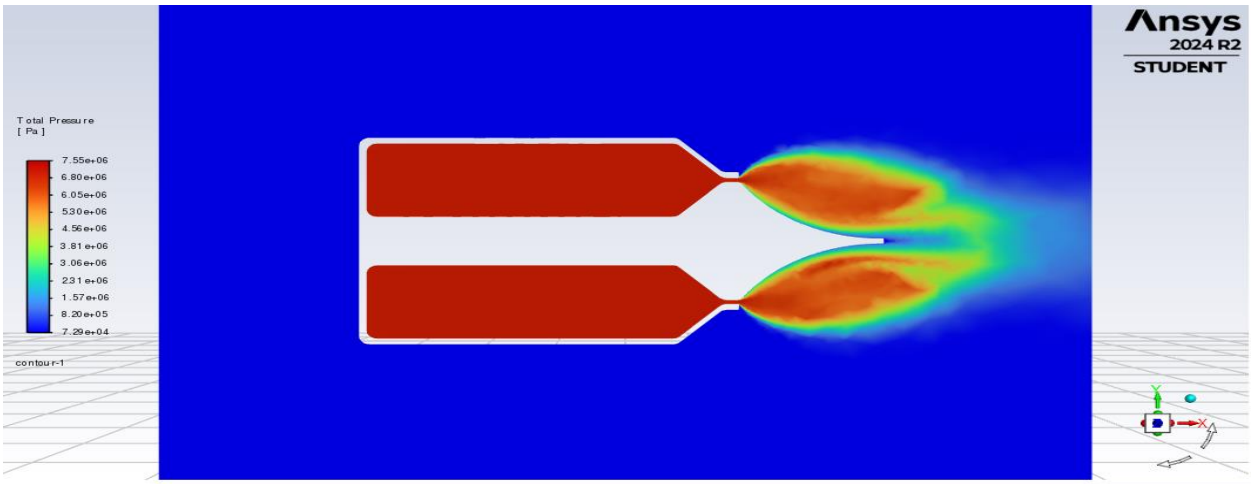

Figure 7.60 Total pressure distribution for config. 3

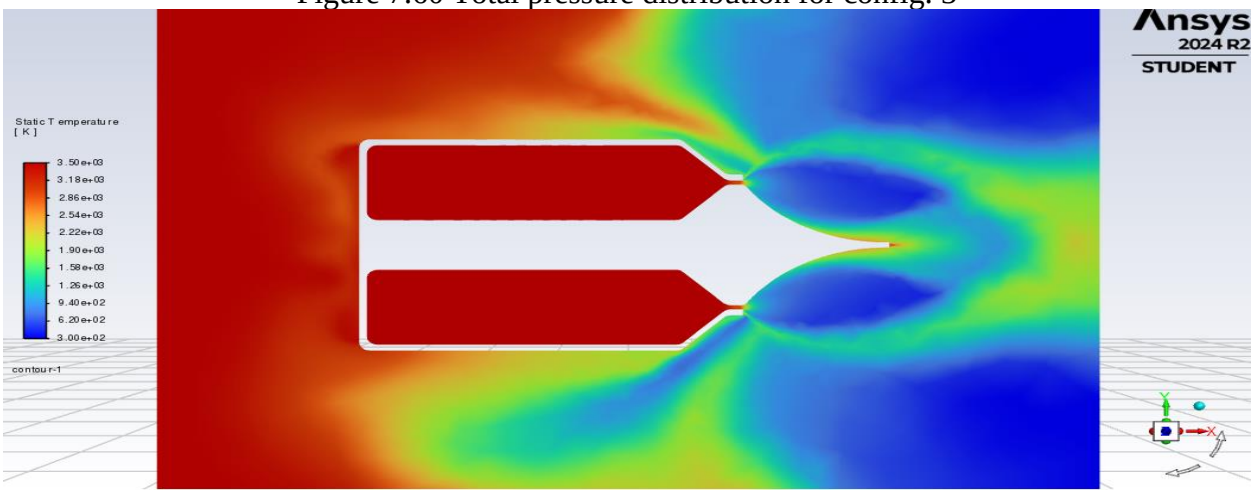

Figure 7.61 Static temperature distribution for config. 3

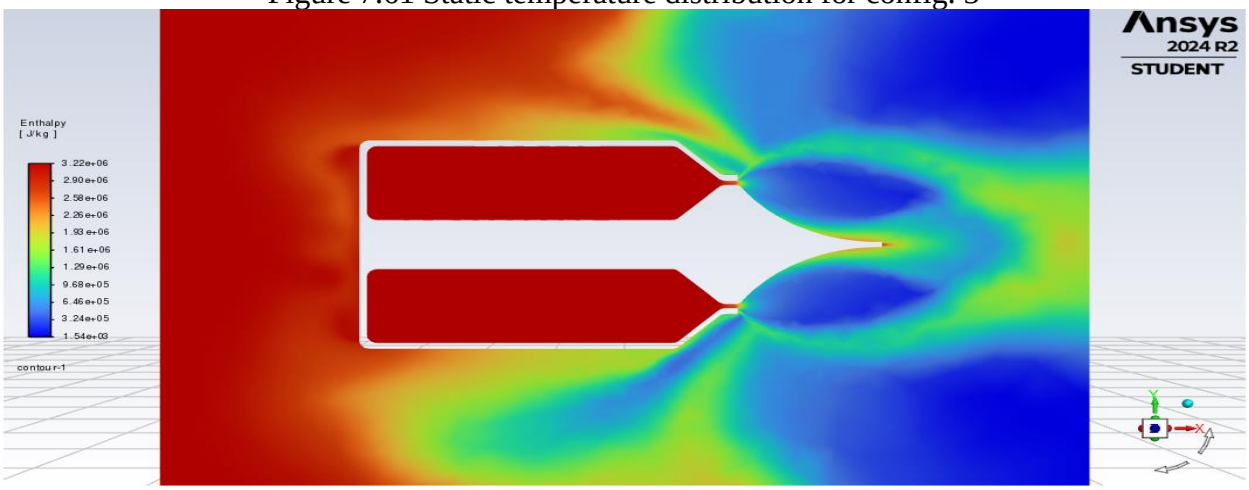

Figure 7.62 Enthalpy distribution for config. 3

7.4.10 Configuration 4 results at 51235 Pa

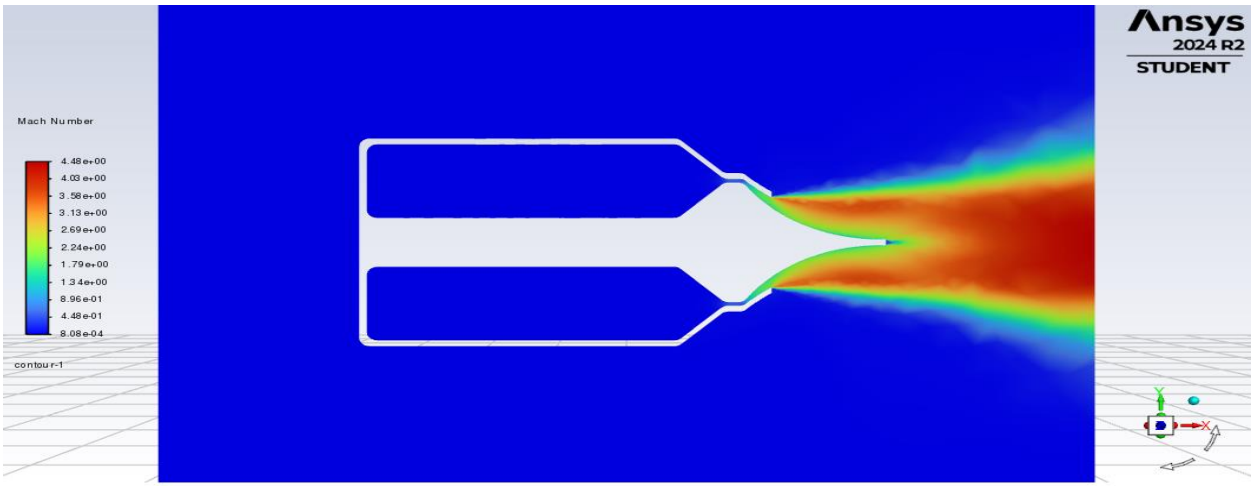

Figure 7.63 Mach distribution for config. 4

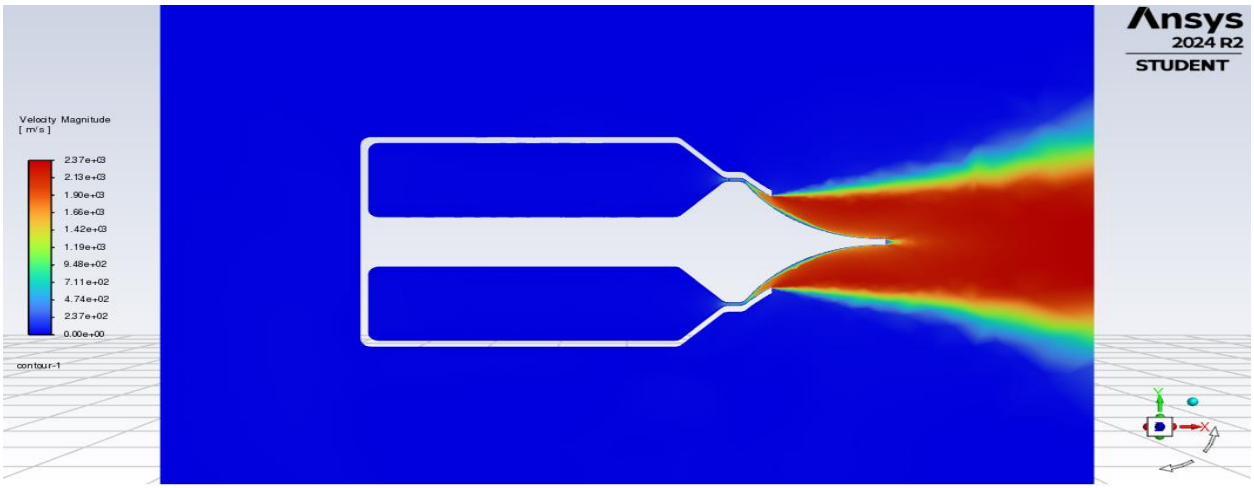

Figure 7.64 Velocity distribution for config. 4

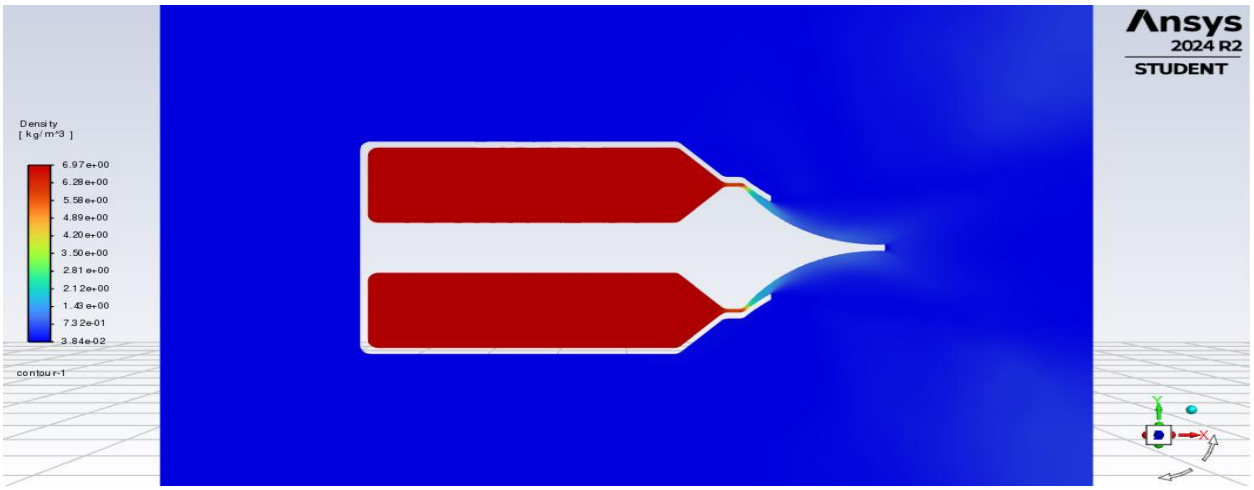

Figure 7.65 Density distribution for config. 4

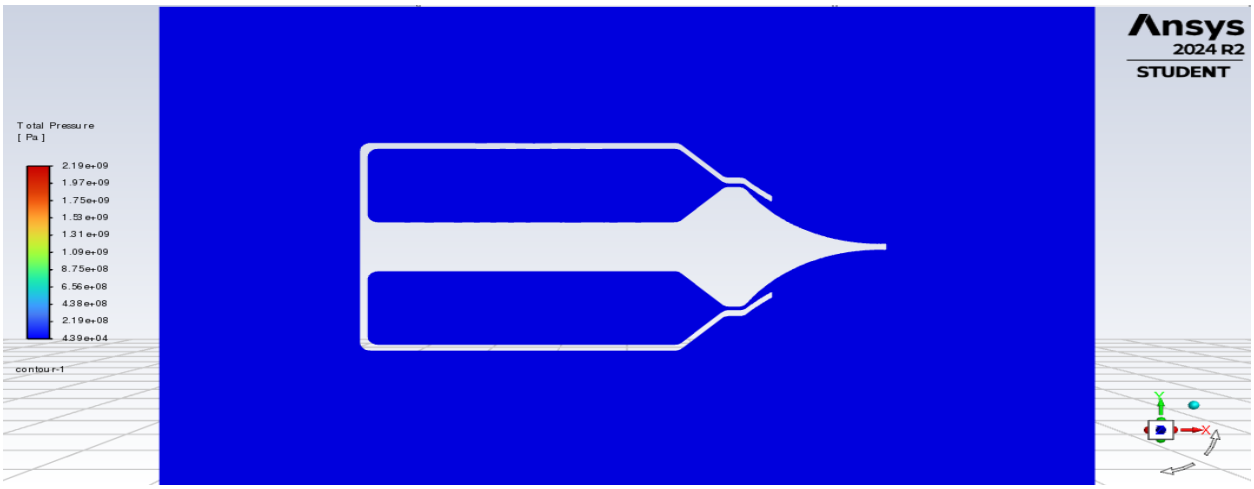

Figure 7.66 Total pressure distribution for config. 4

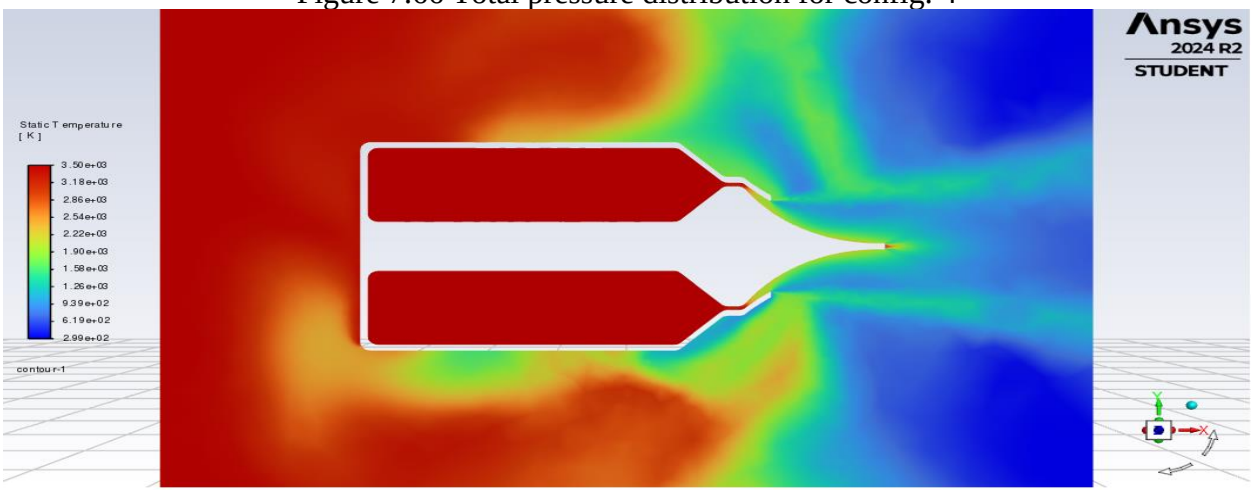

Figure 7.67 Static temperature distribution for config. 4

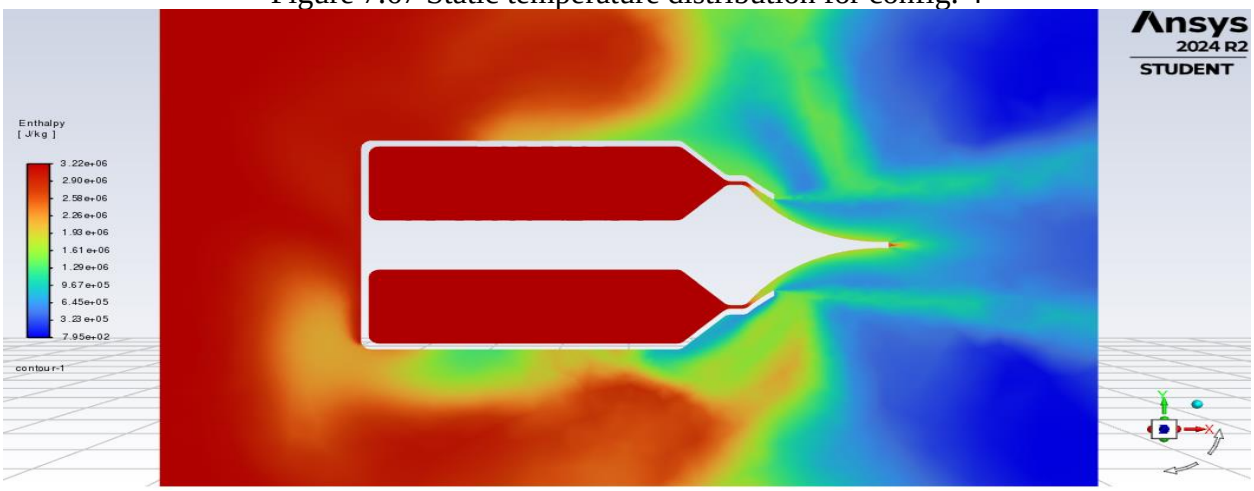

Figure 7.68 Enthalpy distribution for config. 4

7.4.11 Configuration 4 results at 81235 Pa

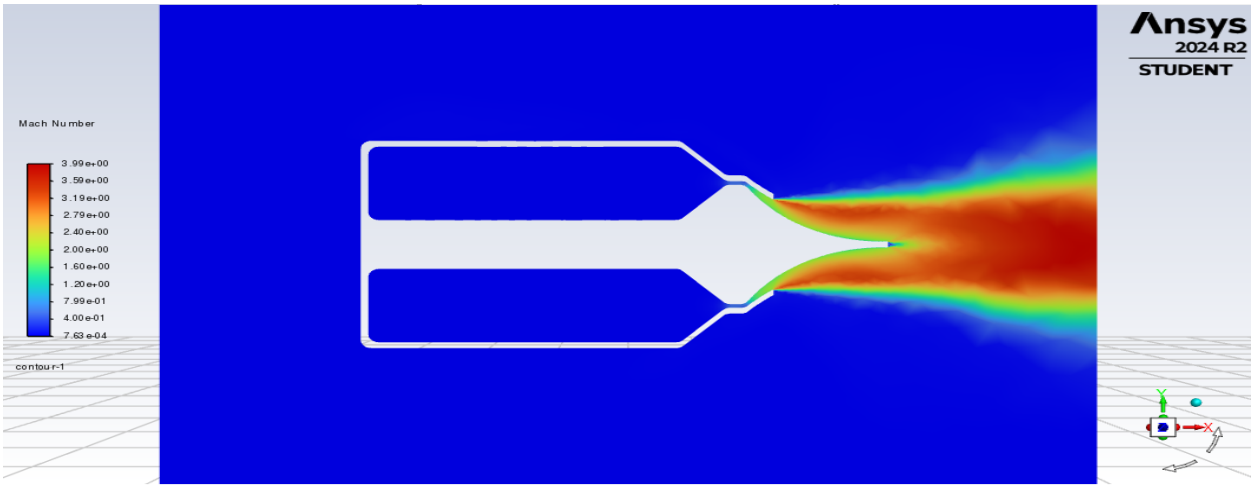

Figure 7.69 Mach distribution for config. 4

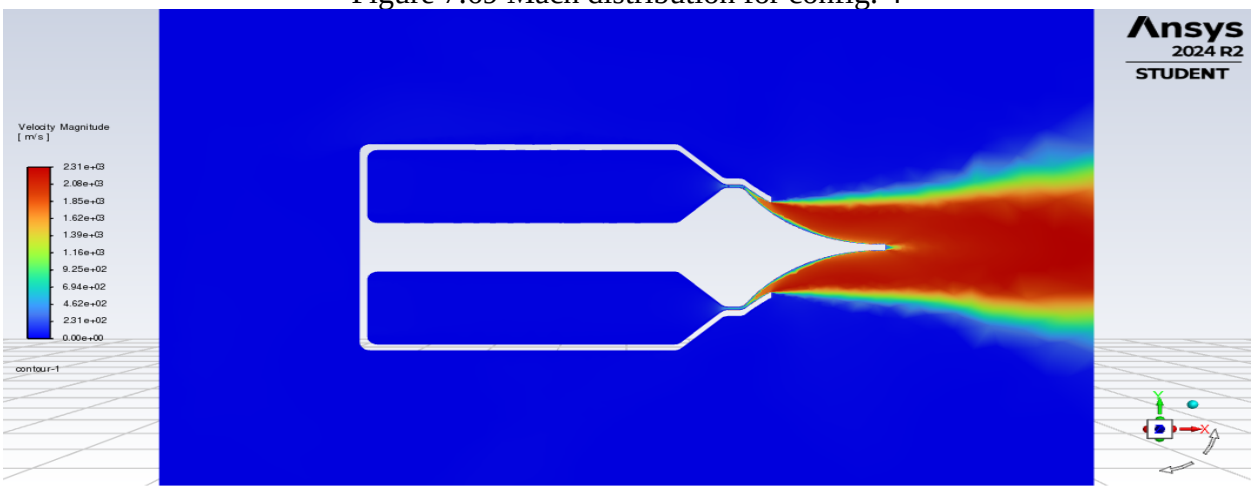

Figure 7.70 Velocity distribution for config. 4

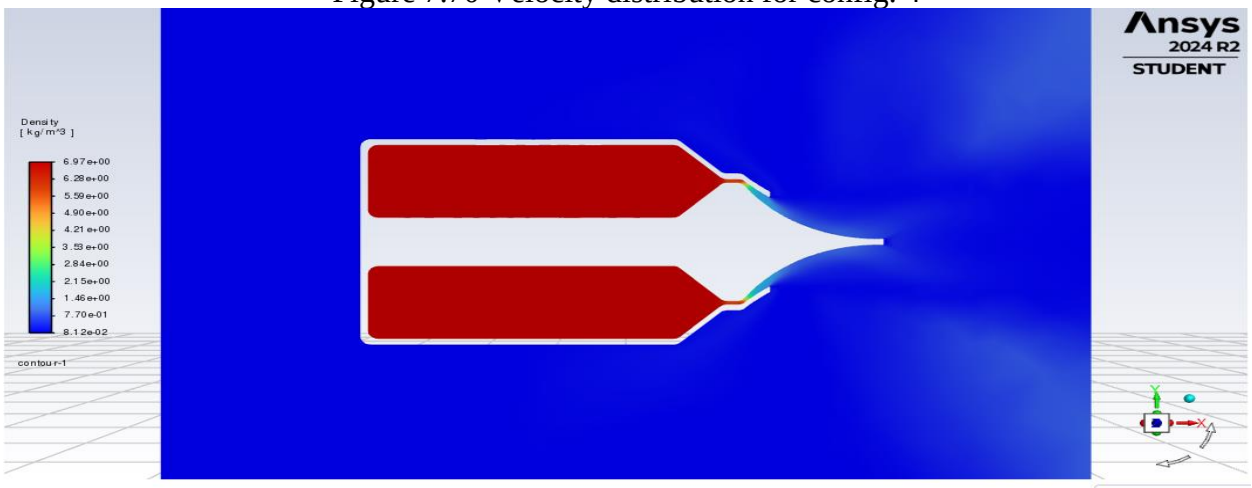

Figure 7.71 Density distribution for config. 4

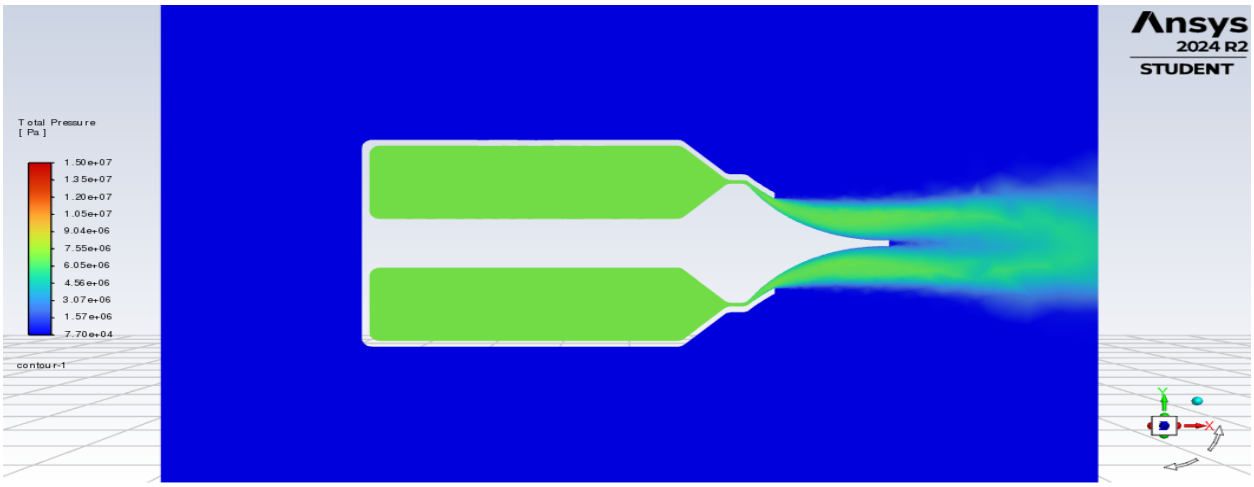

Figure 7.72 Total pressure distribution for config. 4

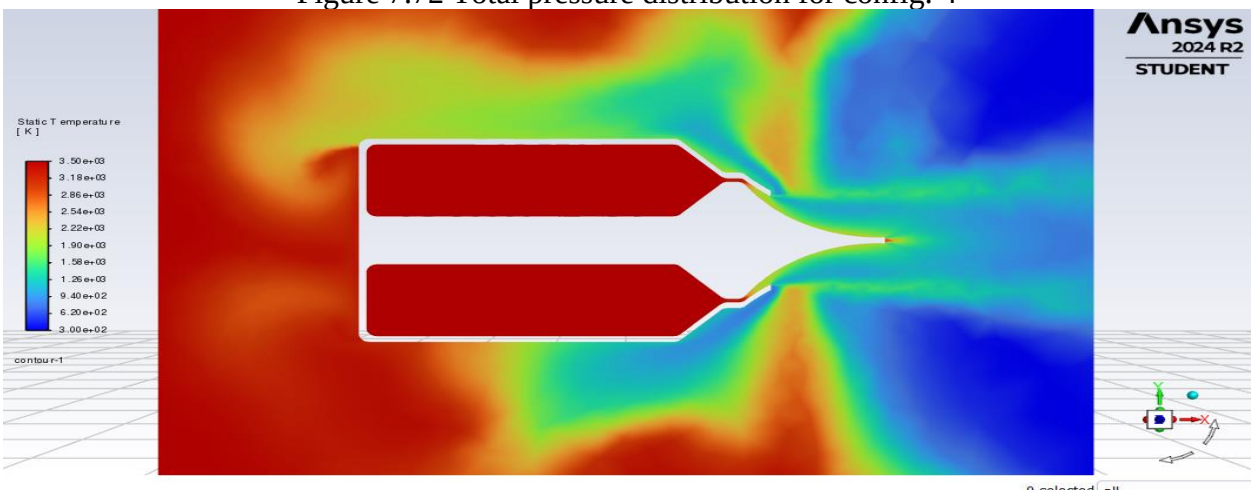

Figure 7.73 Static temperature distribution for config. 4

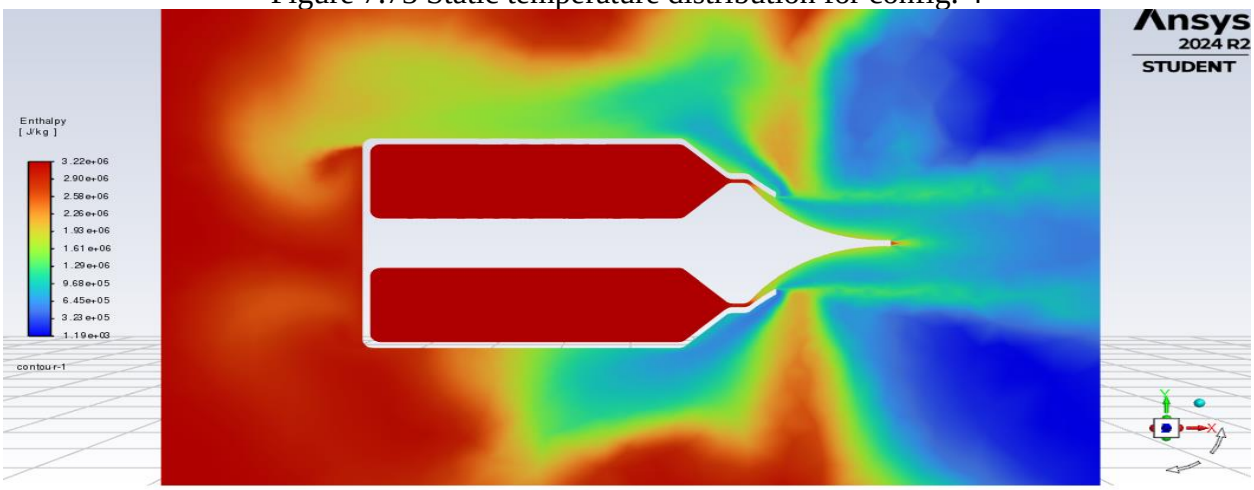

Figure 7.74 Enthalpy distribution for config. 4

7.4.12 Configuration 4 results at 101235 Pa

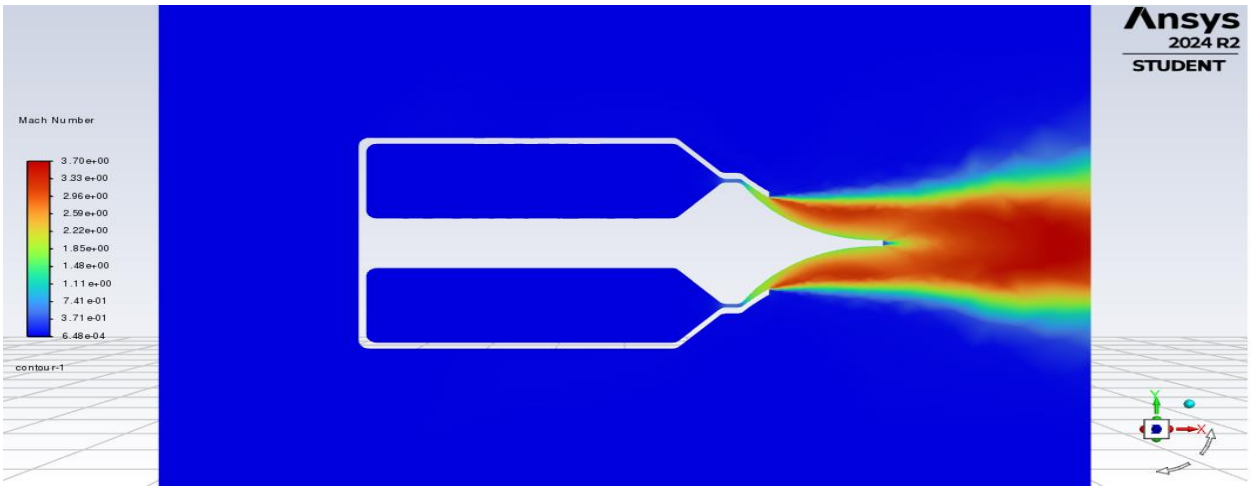

Figure 7.75 Mach distribution for config. 4

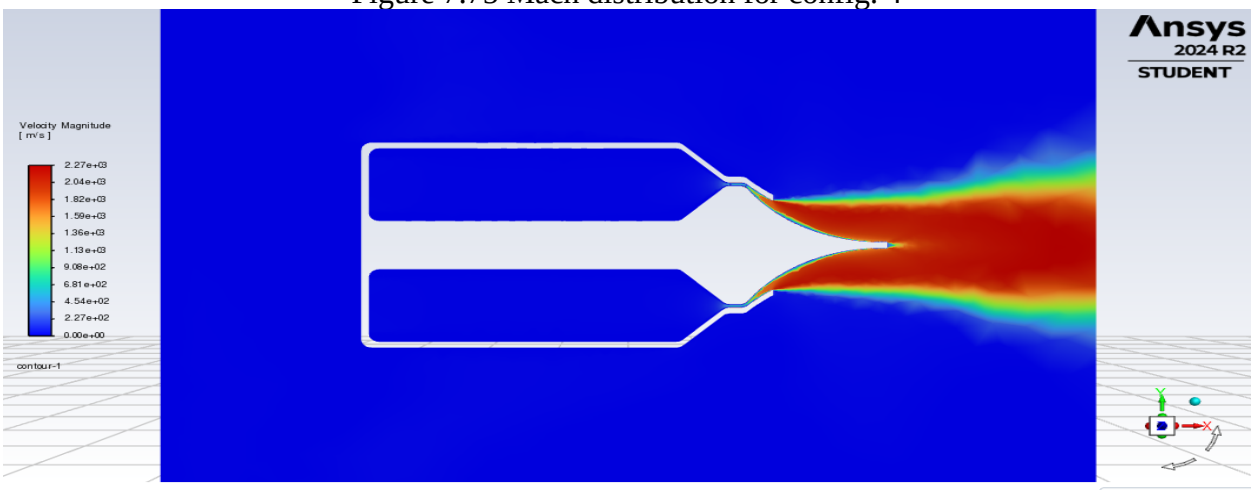

Figure 7.76 Velocity distribution for config. 4

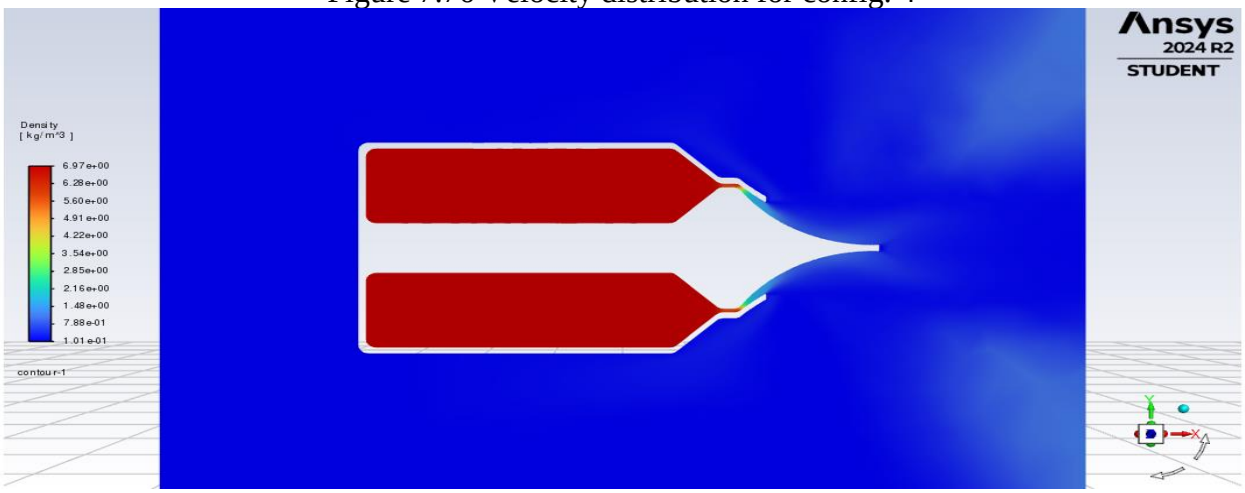

Figure 7.77 Density distribution for config. 4

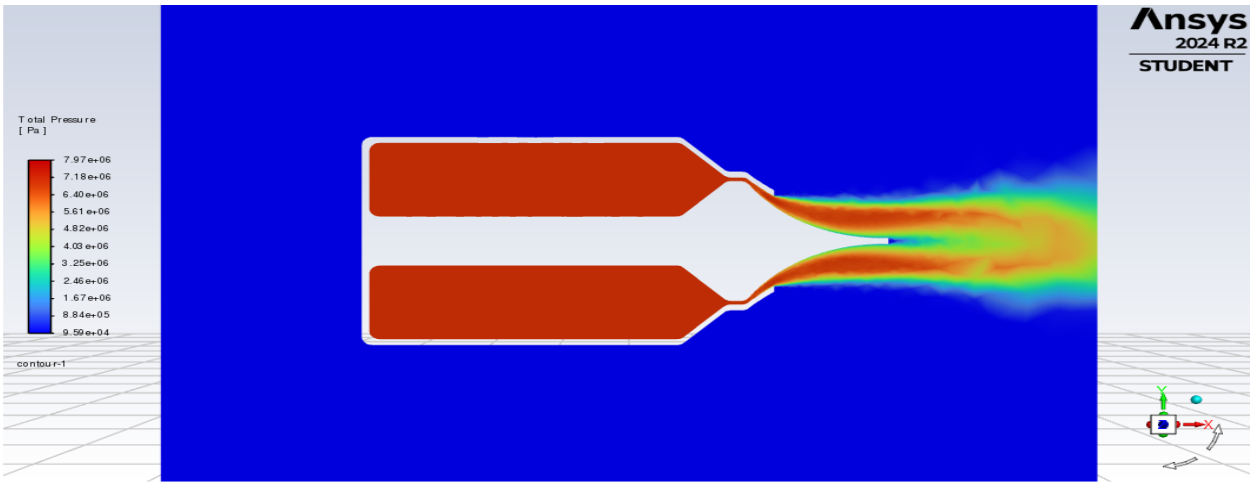

Figure 7.78 Total pressure distribution for config. 4

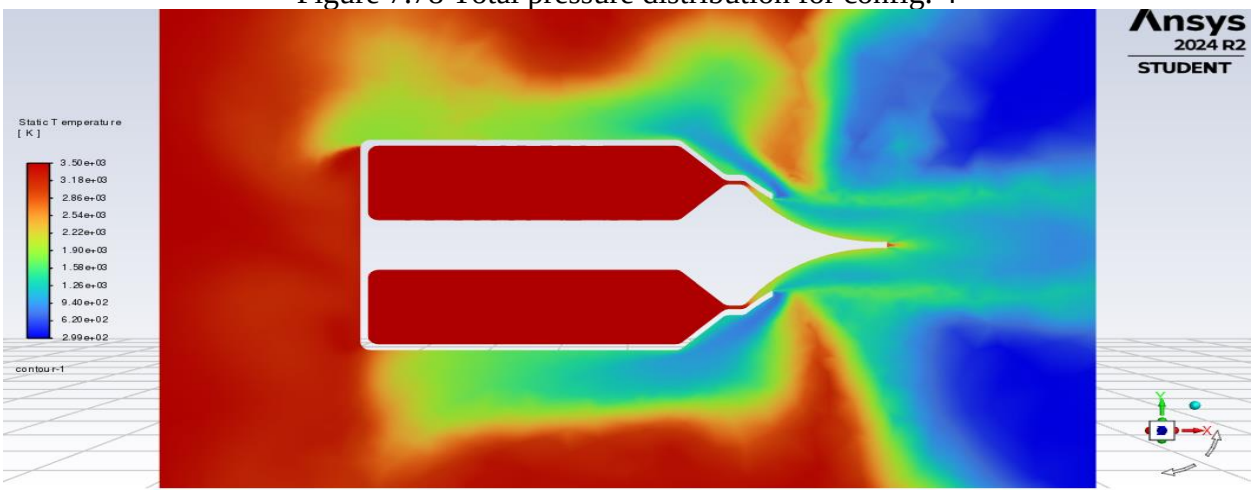

Figure 7.79 Static temperature distribution for config. 4

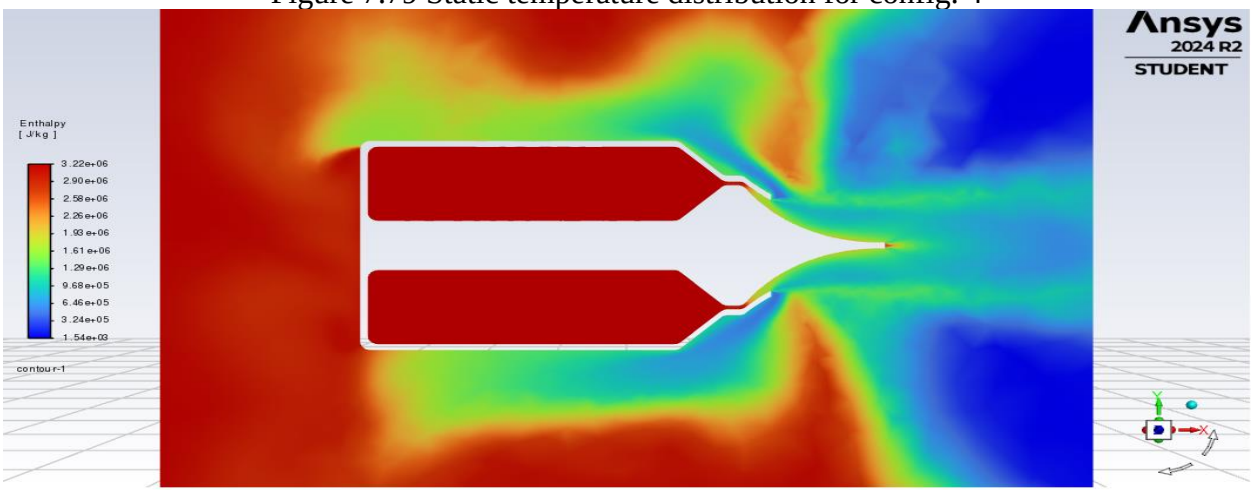

Figure 7.80 Enthalpy distribution for config. 4

7.4.12 Summary of tables

The following tables summarize the theoretical predictions, CFD results, and percent errors for each of the four aerospike nozzle configurations for the varying ambient pressures.

Table 7.2 Theoretical vs CFD exit mach number and velocity

Config #	Ambient Pressure	Exit Mach (Theory)	Exit Mach (CFD)	% Error	Exit Velocity (Theory) [m/s]	Exit Velocity (CFD) [m/s]	% Error
Configuration 1	51325	3.92	3.6	8.89%	2298.24	2240	2.60%
Configuration 1	81325	3.586	3.31	8.34%	2041.38	1980	3.10%
Configuration 1	101325	3.431	3.29	4.29%	2038.4	1960	4.00%
Configuration 2	51325	3.92	4.13	5.08%	2483.92	2440	1.80%
Configuration 2	81325	3.586	3.27	9.66%	2246.4	2160	4.00%
Configuration 2	101325	3.431	2.97	15.52%	2185.38	2130	2.60%
Configuration 3	51325	3.92	2.61	50.19%	2536.02	2190	15.80%
Configuration 3	81325	3.586	2.44	46.97%	2105.4	1740	21.00%
Configuration 3	101325	3.431	2.33	47.25%	1834.19	1490	23.10%
Configuration 4	51325	3.92	4.48	12.50%	2486.13	2370	4.90%
Configuration 4	81325	3.586	3.99	10.13%	2409.33	2310	4.30%
Configuration 4	101325	3.431	3.7	7.27%	2383.5	2270	5.00%

Table 7.3 Theoretical vs CFD thrust

Configuration	Ambient Pressure	Thrust (Theory) [N]	Thrust (CFD) [N]	% Error
Configuration 1	51325	89600	95961.6	6.63%
Configuration 1	81325	79200	84823.2	6.63%
Configuration 1	101325	78400	85377.6	8.17%
Configuration 2	51325	97600	98966.4	1.38%
Configuration 2	81325	86400	88819.2	2.72%
Configuration 2	101325	85200	88522.8	3.75%
Configuration 3	51325	87600	108186	19.03%
Configuration 3	81325	69600	86025.6	19.09%
Configuration 3	101325	59600	74142.4	19.61%
Configuration 4	51325	94800	100108.8	5.30%
Configuration 4	81325	92400	94432.8	2.15%
Configuration 4	101325	90800	92706.8	2.06%

7.5 Discussion

The parametric study revealed trends regarding how geometric and environmental changes impact aerospike nozzle performance. Among the four configurations tested, Configuration 4, which combined throat area reduction, chamber extension, and ramp curvature modification, consistently yielded the most optimal results across various ambient pressures.

Compared to the baseline and individual configurations, Configuration 4 exhibited:

- The highest exit Mach numbers and exit velocities, particularly at lower ambient pressures (51,325 Pa and 81,325 Pa).

- The best agreement between theoretical and CFD thrust values, with percent errors consistently below 5%, indicating a highly efficient expansion process.

- Improved thrust generation compared to other configurations, with CFD thrust reaching up to 100,109 N at low ambient pressures.

In contrast, Configuration 3 (ramp curvature only) showed the largest discrepancies between theoretical and CFD results, particularly in Mach number and velocity, suggesting that ramp steepening alone may induce flow separation or suboptimal expansion behavior. Configuration 1 (throat reduction only) and Configuration 2 (chamber extension only) improved performance relative to the baseline, but not as significantly as the combined approach used in Configuration 4.

Overall, the combined modifications in Configuration 4 synergistically enhanced flow acceleration, energy preservation, and thrust production, validating the effectiveness of a multi-parameter optimization strategy for aerospike nozzle design.

7.6 Conclusion

This chapter conducted a comprehensive parametric analysis of the aerospike nozzle, investigating the effects of throat area reduction, chamber area extension, ramp curvature adjustment, and ambient pressure variations on nozzle performance. Through a series of 3D CFD simulations and theoretical comparisons, it was determined that Configuration 4—which integrated all geometric modifications—provided the most optimal results, achieving the highest thrust, exit Mach number, and velocity across a range of environmental conditions.

Configuration 4 demonstrated superior expansion characteristics, minimal total pressure losses, and strong agreement between simulated and theoretical performance predictions, making it the best candidate for future integrated nozzle designs.

Having now identified the most effective aerospike nozzle configuration, the final chapter of this project will focus on integrating the optimal nose cone and nozzle designs developed throughout this research. Chapter 8 will synthesize the improvements realized from both aerodynamic and propulsion optimizations and assess the overall system performance, culminating with proposed future directions for continued enhancements and experimental validation.

Chapter 8. Conclusion and Future Work

8.1 Final Conclusion

This project conducted a comprehensive analysis and optimization study focused on improving the aerodynamic and propulsion efficiency of a rocket launch vehicle. Beginning with nose cone design optimization and progressing through advanced nozzle configuration studies, the project explored how geometric adjustments and environmental conditions influence overall vehicle performance.

Among the nose cone designs evaluated, the aerodisk configuration emerged as the most effective for minimizing aerodynamic drag, significantly reducing bow shock intensity and stagnation pressure compared to a traditional blunt nose cone.

For the nozzle study, after detailed 3D CFD simulations and theoretical validations, the aerospike nozzle with combined optimizations (Configuration 4) was identified as the most efficient configuration. This design achieved the highest thrust output, best expansion efficiency, and strongest adaptability to varying ambient pressure conditions, compared to traditional conic and bell nozzle designs previously evaluated.

By combining the aerodisk nose cone and the optimized aerospike nozzle, the overall launch vehicle system would benefit from enhanced aerodynamic shaping and thrust efficiency, offering a strong foundation for high-performance space launch or hypersonic applications.

8.2 Future Work

While the current study provided meaningful insights, several areas warrant further investigation. Future work could involve the development and simulation of a full-scale Falcon 9 geometry, incorporating detailed body contours, realistic material properties, and the effects of external aerodynamic forces. In addition, higher-fidelity CFD methods, such as Large Eddy Simulation (LES) or Detached Eddy Simulation (DES), could be employed to improve the accuracy of turbulence modeling and shock capturing. Simulations may also be expanded to include thermal protection analysis, evaluating surface heating rates and thermal stresses on both the nose cone and nozzle during ascent. To validate computational findings, wind tunnel testing of scaled models or subscale static firing tests of nozzle prototypes should be considered. Furthermore, exploring altitude-adaptive nozzles—flexible geometries that adjust during flight—could yield even greater efficiency gains than fixed designs. Through continued optimization and experimental validation, future designs may achieve enhanced performance and reliability, pushing the boundaries of next-generation space launch systems.

References

[1] Gunter, K., "Worldwide Launches in 2023," *Gunter's Space Page*, 30 April 2025. Retrieved 20 December 2024 from <https://space.skyrocket.de/doc_chr/lau2023.htm>

[2] NASA, "Brief History of Rockets," *NASA Glenn research Center*, 13 May 2021. Retrieved 20 December 2024 from<https://www.grc.nasa.gov/www/k-12/TRC/Rockets/history_of_rockets.html>

[3] Khare, V., and Saha, S., "Rocket Nozzles: 75 Years of Research and Development," *Journal of Aerospace Science and Technology*, Iranian Aerospace Society Paper, Vol. 46, No. 76, 2021. https://doi.org/10.1007/s12046-021-01584-6

[4] Davies, J., Grove, R., Bell, T., Rea, O., Furkert, M., Zhao, D., and Sellier, M. "Preliminary Design and Test of High Altitude Two-Stage Rockets in New Zealand," *Aerospace Science and Technology*, Department of Mechanical Engineering, College of Engineering, University of Canterbury, New Zealand, Vol. 128, No. 107741, Sep. 2022. https://doi.org/10.1016/j.ast.2022.107741

[5] Liu, X.-Y., Cheng, M., Zhang, Y.-Z., and Wang, J.-P. "Design and Optimization of Aerospike Nozzle for Rotating Detonation Engine," *Aerospace Science and Technology*, Dept. of Mechanics and Engineering Sciences, Peking Univ., Beijing, China, Vol. 120, No. 107300, Jan. 2022. https://doi.org/10.1016/j.ast.2021.107300

[6] Ajuwon, M., Caballes, M., Xue, J., Burris, A., Alamu, S. O., Qian, X., and Chen, G. "Optimization Design of Rocket Nose Cone for Achieving Desired Apogee by Empirical Research and Simulation-Based Comparison," *Proceedings of the 9th Annual World Conference of the Society for Industrial and Systems Engineering*, Department of Industrial & Systems Engineering, Maryland, Sept. 2020.

[7] Shah, V. K., Ateeb, K., Razzaq, M., Varun, C., and Avinash, B. "Determination of the Optimum Nose Cone Geometrical Shape for Supersonic Missile," *Materials Today: Proceedings*, Dept. of Aeronautical Engineering, MLR Inst. of Technology, Dundigal, India, Vol. 64, Part 1, 2022, pp. 749–754. https://doi.org/10.1016/j.matpr.2022.05.205

[8] Menezes, V., Saravanan, S., Jagadeesh, G., and Reddy, K. P. J., "Experimental Investigations of Hypersonic Flow Over Highly Blunted Cones with Aerospikes," *AIAA Journal*, Indian Inst. of Science, Bangalore, India, Vol. 41, No. 10, 2003, May 2012, pp. 1955-1966. https://doi.org/10.2514/2.1885

[9] Harikrishnan, R., and Lokavarapu, B. R. "Design and Analysis of Rocket Nozzle," *Materials Today: Proceedings*, Cognizant Technology Solutions, Trivendrum, India, Vol. 38, Part 5, 2021, pp. 3365–3371. https://doi.org/10.1016/j.matpr.2020.10.370

[10] Balusamy, K., Vinothraj, A., and Suresh, V. "Aero-Spike and Aero-Disk Effects on Wave Drag Reduction of Supersonic Flow Past Over Blunt Body," *Aircraft Engineering and Aerospace Technology*, Dept. of Aeronautical Engineering Rajalakshmi Engineering College,

Chennai, India, Vol. 96, No. 2, January 2024, pp. 233–247. https://doi.org/10.1108/AEAT-04-2023-0088

[11] Tahsini, A. M., "Heat Release Effects on Drag Reduction in High-Speed Flows," *International Journal of Heat and Mass Transfer*, Aerospace Research Inst., Tehran, Iran, Vol. 57, 2013, pp. 657-661. https://doi.org/10.1016/j.ijheatmasstransfer.2012.10.064

[12] Fernandes, T., Souza, A., and Afonso, F., "A Shape Design Optimization Methodology Based on the Method of Characteristics for Rocket Nozzles," *CEAS Space Journal*, Inst. Superior Técnico, Univ. of Lisboa, Lisbon, Portugal, Vol. 15, No. 3, 2023, pp. 867-879. https://doi-org.libaccess.sjlibrary.org/10.1007/s12567-023-00511-1

[13] Johnston, J. R., Signorelli, R. A., and Freche, J. C. "Performance of Rocket Nozzle Materials with Several Solid Propellants," NASA TN D-3428, NASA Lewis Research Center, Cleveland, OH, May 1966. Retrieved 12 May 2025 from <https://ntrs.nasa.gov/api/citations/19660015713/downloads/19660015713.pdf>.

[14] Sun, D., Luo, T., and Feng, Q. "New Contour Design Method for Rocket Nozzle of Large Area Ratio," *International Journal of Aerospace Engineering*, School of Aeronautics and Astronautics, Dalian Univ. of Tech., Dalian, China, Vol. 2019, No. 4926413, 2019. https://doi.org/10.1155/2019/4926413

[15] Ekadj, F. F., Putro, I. E., Abrizal, H., Mariani, L., Hakim, A. N., Yudanto, M., and Moranova, S. S., "Thermal Stress Analysis on Solid Rocket Nozzles with Fluid-Structure Interaction Simulations," *AIP Conference Proceedings*, The 9th international seminar on Aerospace Science and Technology, Bogor, Indonesia, Vol. 2941, No. 020038, 2023. https://doi.org/10.1063/5.0181496

[16] Raza, M. S., Prasad, A. K., Prasad, L., and Narayan, A., "Heat Flux and Aerodynamics Drag Reduction of a Hypersonic Flow with the Different Tips of the Taper Spike Design Parabolic Nose Cone," *Numerical Heat Transfer, Part A: Applications*, Department of Mechanical Engineering, National Inst. of Tech., Jharkhand, India Vol. 85, No. 1, 2024. https://doi.org/10.1080/10407782.2024.2302080

[17] Lockheed Martin Corporation. *Atlas V User's Guide*, Lockheed Martin, 2010. Retrieved 12 May 2025 from <https://spacecraft.ssl.umd.edu/design_lib/Atlas5.pl.guide.pdf>.

[18] United Launch Alliance. *Delta IV User's Guide*, United Launch Alliance, Centennial, CO, June 2013. Retrieved 12 May 2025 from <https://www.ulalaunch.com/docs/default-source/rockets/delta-iv-user's-guide.pdf >.

[19] SpaceX. *Falcon 9 Launch Vehicle User's Guide*, Space Exploration Technologies Corp., Hawthorne, CA, Sept. 2021. Retrieved 12 May 2025 from <https://www.spacex.com/media/falcon-users-guide-2021-09.pdf>

[20] United Launch Alliance. *Atlas V Launch Services User's Guide*, Revision 11, Centennial, CO, March 2010. Retrieved 12 May 2025 from <https://www.ulalaunch.com/docs/default-source/rockets/atlasvusersguide2010.pdf>

APPENDICES

Appendix A - Matlab Script : Aerospike Nozzle Theoretical Calculations

```
% Aerospike Nozzle Theoretical Calculations

% Based on Liu et al. [5]

% Define constants

gamma = 1.4;          % Ratio of specific heats (ideal air)

R = 287;              % Specific gas constant for air [J/(kg*K)]

Pc = 7e6;             % Combustion chamber pressure [Pa]

Pa = [51325 81325 101325];          % Ambient pressure [Pa]

T_exit = 1600;        % Estimated exit temperature [K] (adjust based on simulation results)

%Base Config T = 1600

%Config 1:

%Config 2:

%Config 3:

%Config 4:

m_dot = 123.05;           % Assumed mass flow rate [kg/s] (adjustable)

A_exit = pi*(.162)^2;        % Assumed exit area [m^2] (adjustable)

At =2*( pi*(.162)^2 - pi*(.152)^2);

At_10=2*( pi*(.162)^2 - pi*(.153)^2);

% Nozzle Pressure Ratio

NPR = Pc ./ Pa;

% Calculate Exit Mach Number

Me = sqrt((2 / (gamma - 1)) * ((NPR)^((gamma - 1) / gamma) - 1));

% Calculate Area Ratio A/A_t

Area_ratio = (1 / Me) * ((2 / (gamma + 1)) * (1 + ((gamma - 1) / 2) * Me^2))^((gamma + 1) / (2 *
(gamma - 1)));

% Calculate Prandtl-Meyer function omega (in degrees)

omega = sqrt((gamma + 1) / (gamma - 1)) * atand(sqrt(((gamma - 1) / (gamma + 1)) * (Me^2 - 1)))
...

       - atand(sqrt(Me^2 - 1));

% Calculate speed of sound at exit

a_exit = sqrt(gamma * R * T_exit);

% Calculate exit velocity
```

```
W_exit = Me * a_exit;

% Assume exit pressure is ambient for ideally expanded nozzle

P_exit = Pa;%9.06*10^6;

% Calculate exit thrust

F_exit = m_dot * W_exit + (P_exit - Pa) * A_exit; % second term drops out if P_exit = Pa

% Display results

fprintf('Exit Mach Number (Me): %.3f\n', Me);

fprintf('Area Ratio (A/A_t): %.3f\n', Area_ratio);

fprintf('Prandtl-Meyer Expansion Angle (omega): %.3f degrees\n', omega);

fprintf('Exit Velocity (W_exit): %.2f m/s\n', W_exit);

fprintf('Exit Thrust (F_exit): %.2f N\n', F_exit);

Ago = At*Area_ratio
```